Design and Control of a Gravity-Assisted Underactuated Snake Robot with Application to Aircraft Wing Assembly

by

Binayak Roy

B. Tech., Manufacturing Science and Engineering
IIT Kharagpur, 2001

S.M., Mechanical Engineering
MIT, 2003

Submitted to the Department of Mechanical Engineering
in partial fulfillment of the requirements for the degree of

Doctor of Philosophy

at the

MASSACHUSETTS INSTITUTE OF TECHNOLOGY

February 2008

Author ....
Department of Mechanical Engineering
September 30, 2007

Certified by ....
H. Harry Asada
Ford Professor of Mechanical Engineering
Thesis Supervisor

Accepted by ....
Lallit Anand
Chairman, Department Committee on Graduate Students

Design and Control of a Gravity-Assisted Underactuated Snake Robot with Application to Aircraft Wing Assembly

by

Binayak Roy

Submitted to the Department of Mechanical Engineering
on September 30, 2007, in partial fulfillment of the
requirements for the degree of
Doctor of Philosophy

Abstract

We present the design and control of a hyper-articulated robot arm comprising just a few active joints driving a multitude of passive joints. This underactuated arm design was motivated by the need for a compact snake-like robot for assembly operations inside an aircraft wing. The interior of the wing is accessible only through small access portholes distributed along the length. Currently, such assembly operations are performed by human operators who crawl into the wing through its access portholes. The working conditions are ergonomically challenging and result in frequent injuries. The conflicting requirements of small form factor and high payload carrying capacity have been the primary bottlenecks in the development of assembly robots.

We propose a nested-channel serial linkage structure for the hyper-articulated arm. When fully contracted, the arm is extremely compact and can access the interior of the wing through its access porthole. Once inside the wing, the arm may be expanded to access distal assembly locations. However, it is impossible to package current actuator technology to meet the payload requirements within the limited size of the robot arm. The joints of the hyper-articulated arm have no dedicated actuators. Instead, they are deployed by modulating gravitational torques. By tilting the base link appropriately, the gravitational torque drives each unactuated link to a desired angular position. With simple, compact locking mechanisms, the arm can change its configuration using the actuated base placed outside the wing.

We analyze the system dynamics to gain physical insight into the interaction between the actuated and unactuated degrees of freedom. We make important approximations to capture the dominant effects in the system dynamics so as to facilitate control design. The dynamics (actual, as well as approximate) of the unactuated links are essentially 2^{nd} order non-holonomic constraints, for which there are no general control techniques. We present several motion planning algorithms for sequential positioning of the free joints of the robot arm. The motion planning algorithms are formulated as parameterized non-linear two point boundary value problems. These algorithms demonstrate reasonable performance in the absence of disturbances. However, the end-effecter requires accurate positioning to perform assembly operations.

To address this issue, we present a sequential closed-loop control algorithm for accurate positioning of the free joints. We synthesize a Lyapunov function to prove the convergence of this control scheme and to generate estimates of the domain of convergence. For faster deployment of the robot arm, multiple free links must move concurrently. We also present several motion planning algorithms to address this problem.

We built two prototypes to illustrate the design and actuation concepts. The first prototype has 3 links and has a fixed axis of tilt in the horizontal plane. The second prototype has 4 links and may be tilted about an arbitrary axis in the horizontal plane. The motion planning and closed-loop control algorithms were implemented on both prototypes. The experimental results indicate the efficacy of such control schemes.

Thesis Supervisor: H. Harry Asada
Title: Ford Professor of Mechanical Engineering

Acknowledgments

I am grateful to Prof. Asada for his guidance at all stages of work during the preparation of this thesis. His phenomenal vision and deep insight will always be a source of inspiration for me. I would also like to thank my committee members Prof. Haller and Prof. Youcef-Toumi for their feedback and interest in my work.

It has been wonderful being a part of the d'Arbeloff Lab both academically and socially. My thanks to Tao Cheng, Kyu-Jin Cho, Jin-Oh Hahn, Devin McCombie, Manas Menon, Lael Odhner, Philip Shaltis, Eric Wade and Levi Wood for all the help and support that they have extended to me. My special thanks also to Dr. Jun Ueda for many helpful discussions on theoretical as well as engineering aspects of the problem.

I would also like to thank all my friends who provided me with encouragement as well as much needed distractions during this work.

Last, but not the least, my sincere thanks to my parents for their love and support.

Contents

List of Figures

Chapter 1

Introduction

Most assembly operations in aircraft manufacturing are currently done manually. Although aircraft are small in lot size, numerous repetitive assembly operations have to be performed on a single aircraft. The conditions are often ergonomically challenging and these result in low productivity as well as frequent injuries. Thus, there is a need to shift from manual assembly to automated robotic assembly. The following wing-box assembly illustrates this.

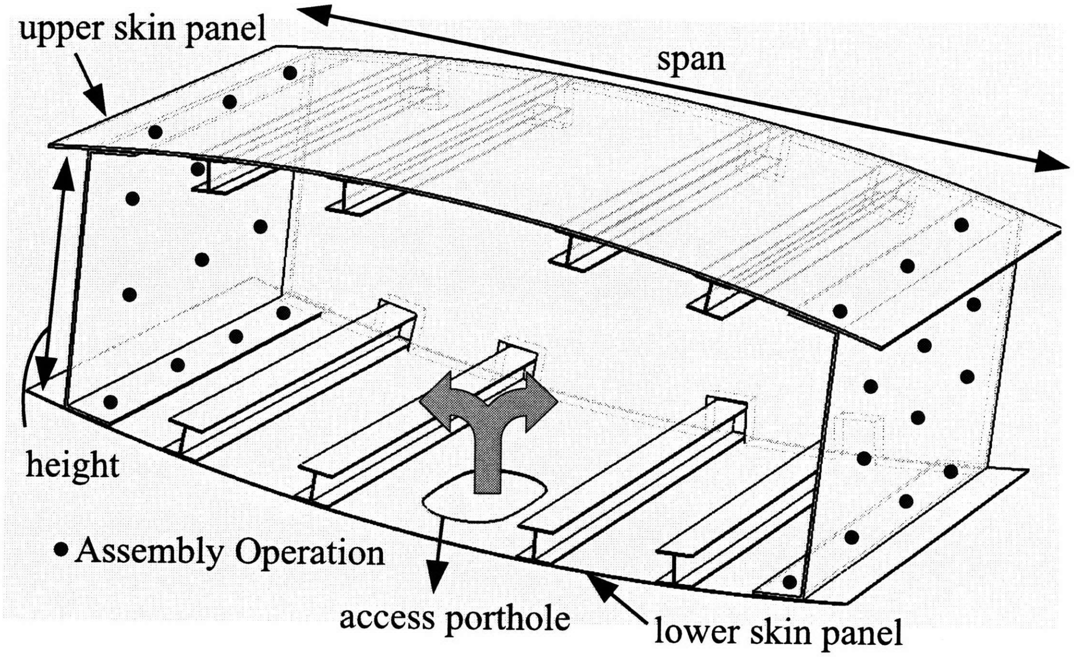

Figure 1-1: Cross-section of an aircraft wing

Fig. 1-1 shows a cross-section of an aircraft wing. Several assembly operations, such as burr-less drilling and fastener installations, have to be carried out inside the wing after the *upper* and *lower skin panels* are in place. The interior of the wing is accessible **only** through small portholes along its length. These *access portholes* are roughly elliptical with dimensions of 0.46 m (18 in) by 0.25 m (10 in). The wing also has a substantial *span*, which varies from 0.9 m (36 in) to 3 m (120 in) depending upon the size of the aircraft. The *height* of the section varies from about 0.2 m (8 in) to 0.9 m (36 in), depending upon the size of the aircraft, as well as the location of the wing-section along the length of the wing. Presently, the assembly operations are carried out manually. A worker enters the wing-box through the small portholes and lies flat on the base, while carrying out the assembly operations. Evidently, the working conditions are ergonomically challenging.

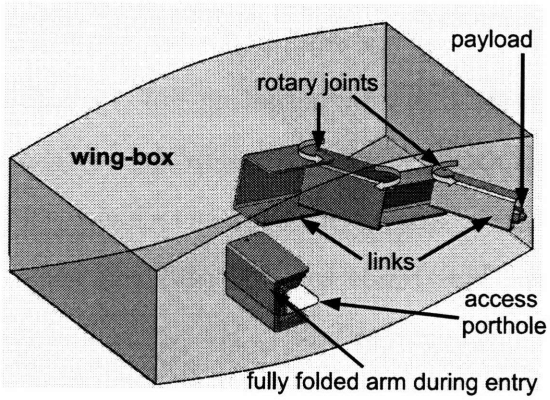

Figure 1-2: Structure of robot arm

We propose a "nested-channel" hyper-articulated mechanism capable of operating inside the aircraft wing. The links are essentially C-channels with successively smaller base and leg lengths, as shown in Fig. 1-2. They are connected by one degree-of-freedom rotary joints, the axes of which are parallel. The use of channel structures is advantageous for a number of reasons. The channels can fold into each other resulting in an extremely compact structure during entry through the porthole, as shown in Fig. 1-2. Once inside the wing, the links may be deployed to access distal points in the assembly space. The open channel structure also facilitates the attachment of a payload to the last link without increasing the overall dimensions of the arm.

The lack of a compact, powerful and high stroke actuation mechanism is the primary bottleneck in the development of the hyper-articulated arm. Other hyper-articulated mechanism, such as snake robots, are well known in robotics literature [3, 27]. They are primarily used for reconnaissance purposes and the issue of payload has not been addressed. We propose an underactuated design concept which obviates the use of dedicated actuators for each joint. Instead, we utilize gravity for driving individual joints. This drastically reduces the size and weight of the manipulator arm. The methodology requires a single actuator for tilting the arm at the base. This single actuator can be placed *outside* the wing and can be used in conjunction with simple locking mechanisms to reconfigure the hyper-articulated structure.

The reconfiguration scheme is illustrated in Fig. 2-5, which shows a schematic of an n-link robot arm. The base link (link 1) is the only servoed link. It may be rotated about a fixed axis $\mathbf{Z}$, which is orthogonal to the direction of gravity. All other joint axes are orthogonal to $\mathbf{Z}$. They are equipped with simple *on-off* locking mechanisms only. The goal is to rotate link i by actuating link 1 appropriately. All unactuated links except link i are locked. Link 1 starts in the vertical upright position. Then it is rotated, first clockwise and then counter-clockwise, before being brought back to its vertical position. This tends to accelerate and then decelerate link i due to gravity and dynamic coupling with link 1. By controlling the tilting angle of link 1, link i can be brought to a desired position with zero velocity. Link i may be locked thereafter. This procedure can be repeated sequentially for the other unactuated links. Contraction of the arm can be performed by reversing the above deployment procedure.

The dynamics of the unactuated links represent non-holonomic constraints, i.e., the constraints cannot be integrated. A considerable amount of work has been done in the area of non-holonomic systems. A good survey of the area is presented in [7]. Most of the work in this area deals with 1^{st} order non-holonomic constraints, i.e., constraints on the velocities. Such constraints arise in motion planning for space robots [11, 13, 16, 17], as well as steering trailers [25, 26], to name a few.

Underactuated systems represent a special class of non-holonomic systems, viz., systems with 2^{nd} order non-holonomic constraints. This was first pointed out by Oriolo and Nakamura [15]. Since then, several researchers have considered the design and control of underactuated mechanisms for robotics applications [1,5,6,8–10,14,22–24]. The focus is mostly on the planar (vertical or horizontal) case where the actuated and unactuated joint axes are parallel. In our approach, the actuated and unactuated joints are orthogonal and we can modulate the effects of gravity by controlling the actuated joint. Other systems in a gravity field, like the Acrobot [2,19], have isolated equilibrium points. Since we can modulate gravity, there exists a continuum of equilibrium points in our system. The presence of gravity also renders our system locally controllable, as can be seen from local linearization. This ensures that we can go from any initial point to any final point in the configuration space of the unactuated coordinate. However, it is inefficient to patch together local linear control laws to traverse the entire configuration space. Moreover, any control design must ensure that the range of motion of the actuated coordinate is small, because the arm operates inside an aircraft wing-box. Earlier approaches [1,10] to the control of underactuated systems generate constructive global control laws applied to specific systems. Such constructive control laws cannot be directly applied to our system.

In Chapter 2, we describe the design of the robot arm based on the functional requirements of the tasks associated with aircraft wing assembly. We first describe some of the assembly operations that are performed in aircraft wing manufacturing. Secondly, we outline the functional requirements and design challenges associated with the automation of such assembly operations. Next, we describe the design of the structure and actuation scheme of the manipulator arm.

In Chapter 3, we analyze the system dynamics of our proposed underactuated system. We gain some physical insight into the interaction between the actuated and unactuated degrees of freedom. We also make important approximations to capture the dominant effects in the system dynamics so as to facilitate control design. The dynamic model is also used to establish the controllability of the system.

In Chapter 4 we propose several motion planning algorithms suitable for the gravity-assisted underactuated robot arm. We first consider the case of sequential link deployment with a fixed axis of tilt. We propose feed-forward optimal control, as well as parameterized trajectory planning schemes for the actuated joint. These approaches essentially result in two-point boundary value problems involving non-linear Ordinary Differential Equations. We present comparisons from numerical simulations of the generated trajectories using these techniques. Secondly, we consider the case of sequential link deployment with an arbitrary axis of tilt. We demonstrate that the motion planning problem has an analytical solution in this case. Next, we consider the case of concurrent multi-link deployment. We present an extension of the parameterized control scheme for sequential link deployment. Numerical simulations indicate the efficacy of this algorithm.

In Chapter 5, we first propose a closed loop control strategy for sequential point-to-point control of the free joints. We synthesize a Lyapunov function to prove the convergence of the control law. The Lyapunov function is used to generate estimates of the domain of convergence of the control law for various control gains. Next, we propose an intermittent feedback control scheme for concurrent multi-link deployment. This is accomplished by smoothly updating the motion plan based on intermittent measurements of the state of the system.

In Chapter 6, we discuss the implementation of our design and control algorithms. We present two prototype systems which illustrate our ideas. The first prototype has 3 links and is actuated through a fixed tilt axis in the horizontal plane. The second prototype has 4 links and may be actuated by tilting about an arbitrary axis in the horizontal plane. We present experimental evidence to demonstrate the efficacy of the control algorithms.

Finally, in Chapter 7, we summarize the contributions of this thesis and propose some future directions.

Chapter 2

Robot Arm Design

In this chapter, we discuss the design of the robot arm based on the functional requirements of the task. We first describe some of the assembly operations that are performed in aircraft wing manufacturing. Secondly, we outline the functional requirements and design challenges associated with the automation of such assembly operations. Next, we describe the design of the structure and actuation scheme of the manipulator arm.

2.1 Task Description

Fig. 2-1 shows a schematic of a section of an aircraft wing. The italicized items in the following description are shown in Fig. 2-1. Several repetitive assembly operations, such as *burr-less drilling* and *fastener installations*, have to be performed inside the wing after the *upper* and *lower skin panels* are attached to the *spars*. The interior of the wing is separated by *ribs* into several compartments along the length. The spacing between successive *ribs* varies from 0.9 m (36 in) to 1.2 m (48 in), depending on the size of the aircraft. Each compartment between such successive *ribs* is called a *wing-box*. Each *wing-box* is accessible only through a small *access porthole* located on the *lower skin panel*. These portholes are roughly elliptical with dimensions of 0.46 m (18 in) by 0.25 m (10 in). The wing also has a substantial *span*, which varies from 0.9 m (36 in) to 3 m (120 in) depending upon the size of the aircraft. The *height* of the *wing-box* varies from about 0.2 m (8 in) to 0.9 m (36 in), depending upon the size of the aircraft, as well as the location of the *wing-box* along the length of the wing.

Fig. 2-1 also shows the various types of joints for the fastener installations. There are essentially three types:

1. *rib flange* to *spar web* joint
2. *rib flange* to *skin* joint
3. *spar cap* to *skin* joint

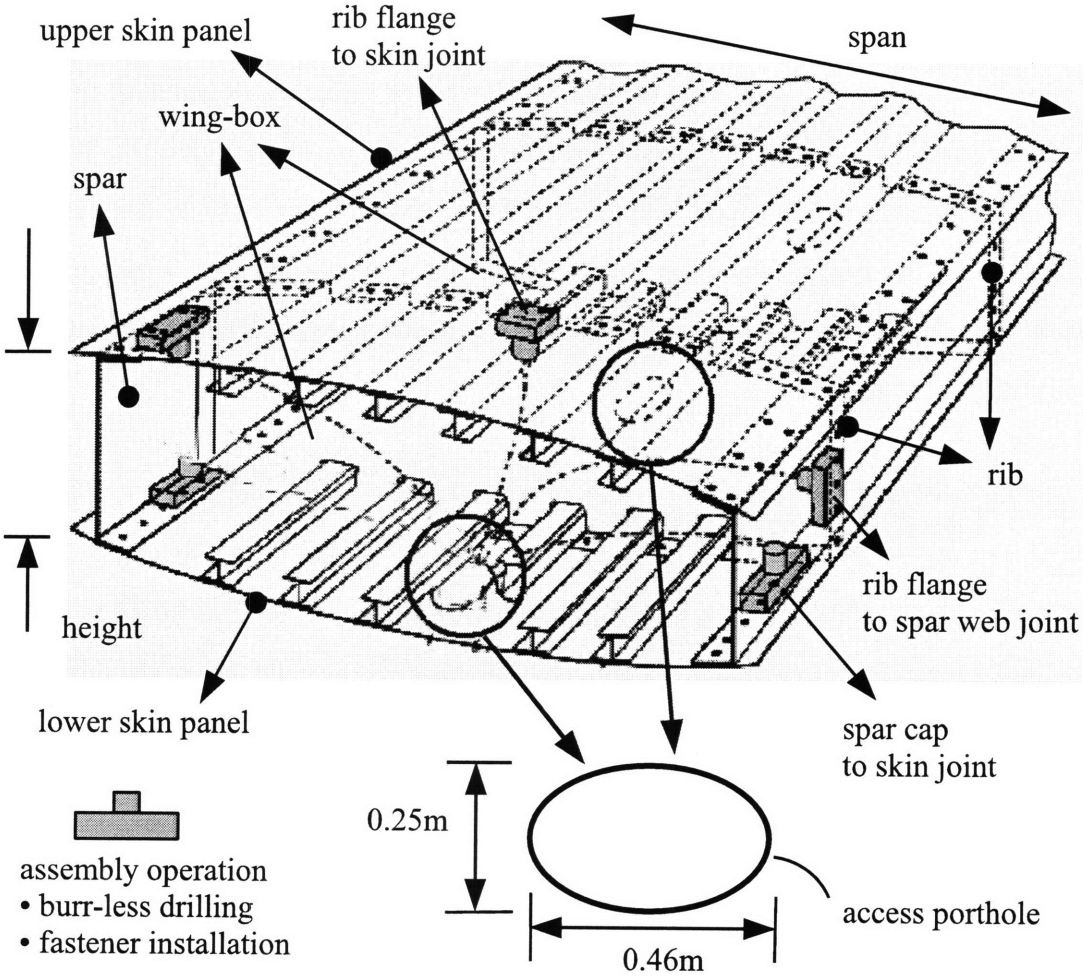

Figure 2-1: Aircraft wing section

The assembly operations are currently performed manually using hand-held pneumatic tools. Fig. 2-2 shows several such tools used for fastener installations. A worker enters each *wing-box* through its *access porthole.* He then lies flat inside the wing and performs the assembly operations. See Fig. 2-3. There could be up to a million fastener installations depending on the size and type of aircraft. Evidently, such repetitive assembly operations inside the *wing-box* are ergonomically challenging.

Figure 2-2: Pneumatic tools for fastener installations

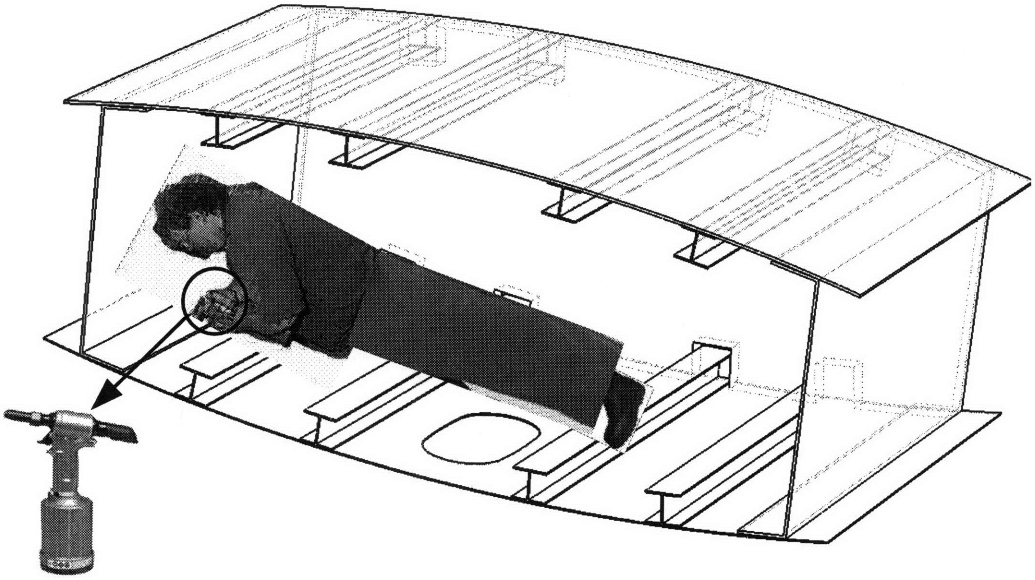

Figure 2-3: Worker performing assembly operations manually

2.2 Functional Requirements

Our goal is to design a robotic device which can automate the assembly operations inside an aircraft wing. This device should be compact enough to enter a *wing-box* through it's *access porthole.* Once inside the *wing-box*, it should be able to access distal points in the assembly space. Additionally, the device has to be designed to carry a payload of approximately 18 kg (40 lb) at the end-effecter.

2.3 Structure of Manipulator Arm

We propose a reconfigurable serial linkage structure for the manipulator arm. The links are essentially C-channels with successively smaller base and leg lengths, as shown in Fig. 2-4. They are connected by 1 d.o.f rotary joints, the axes of which are parallel. The use of channel structures is advantageous for a number of reasons. The channels can fold into each other resulting in an extremely compact structure during entry through the porthole. Once inside the wing-box, the links may be deployed to access distal points in the assembly space. The open channel structure also facilitates the attachment of a payload to the last link without increasing the overall dimensions of the arm.

2.4 Actuation Scheme

The lack of a compact, powerful and high stroke actuation mechanism is the primary bottleneck in the development of the manipulator arm. We propose a novel idea for the actuation of the serial linkage structure, which obviates the use of separate actuators or complex mechanical transmissions for each joint. Our methodology requires a single actuator, which can be placed outside the wing-box and can be used in conjunction with simple locking mechanisms to reconfigure the robot arm. The actuation scheme exploits gravitational and inertial coupling in the system dynamics to rapidly deploy the manipulator arm inside the wing-box.

Fig. 2-5 illustrates the basic deployment process of an n-link arm. There is no

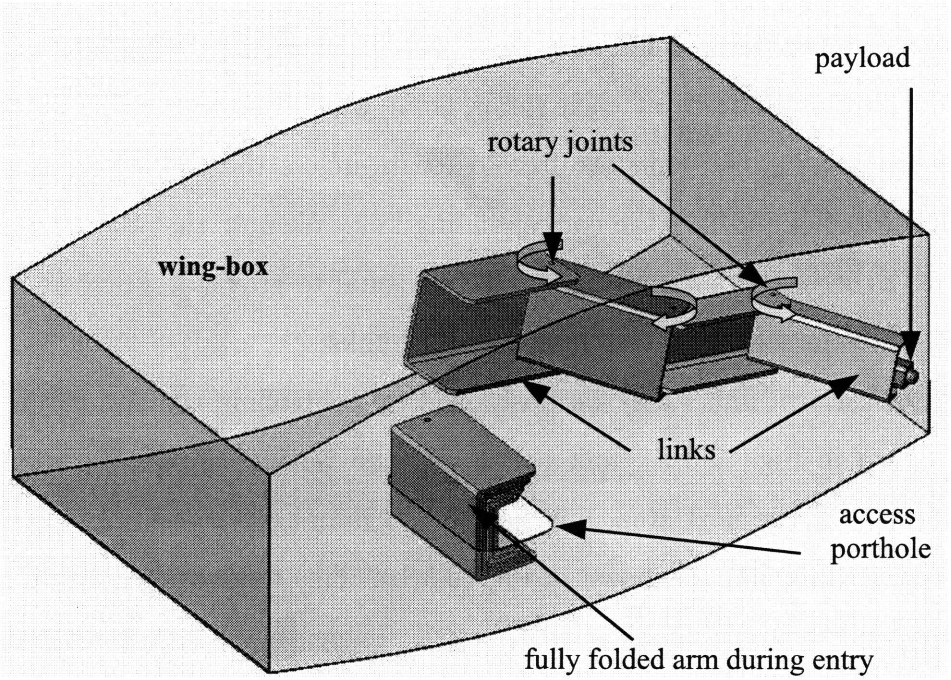

Figure 2-4: Structure of robot arm

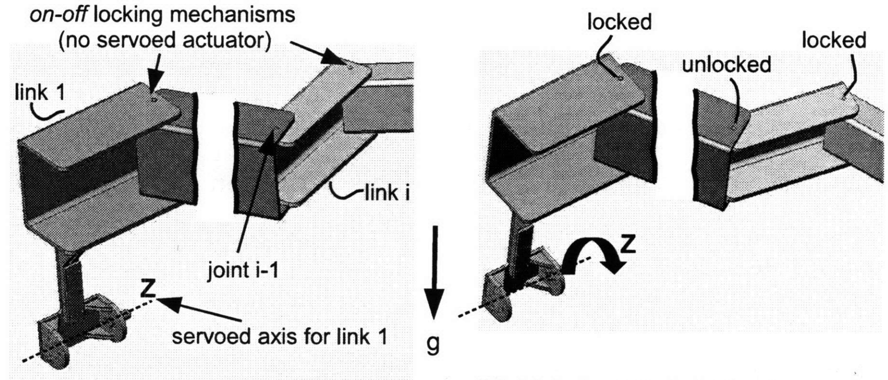

(a) Link 1 vertical

(b) Link 1 rotated clock-wise

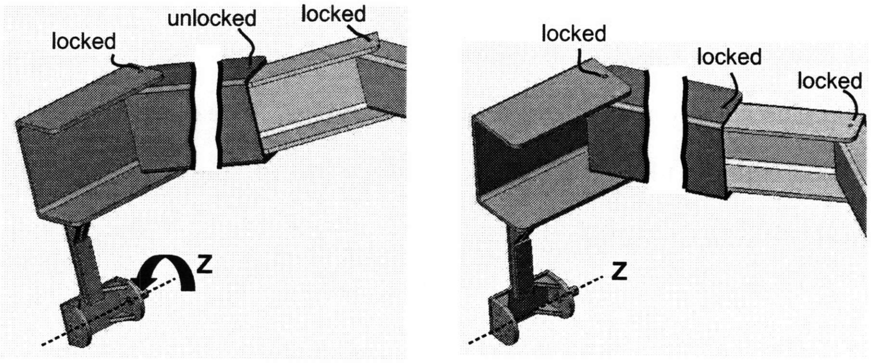

(c) Link 1 rotated counter clock-wise

(d) Link 1 vertical, all joints locked

Figure 2-5: Deployment scheme

dedicated actuator at the individual joints along the arm linkage. The only servoed actuator is at the base of link 1 and is placed outside the wing-box. There is a simple locking mechanism at each rotary joint which operates either in the locked or unlocked mode. The links are free to rotate unless the locking mechanism at a particular rotary joint fixes the corresponding link. We note that the axis of rotation of link 1 (**Z**) is in the horizontal plane (orthogonal to gravity). Further, this axis is orthogonal to the axes of rotation of the other links.

Each distal arm link i may be positioned by controlling the tilting angle of link 1. As shown in Fig. 2-5(a), link 1 starts in the vertical upright position with all joints locked. In the next step, only joint $i-1$ is unlocked and link 1 is rotated in the clockwise direction, as shown in Fig. 2-5(b). This tends to accelerate link i due to gravity and dynamic coupling with link 1. Thereafter, link 1 is rotated counter-clockwise, as shown in Fig. 2-5(c). This tends to decelerate link i. In the final step link 1 is brought back to its vertical position and joint $i-1$ is locked, as shown in Fig. 2-5(d). By controlling the tilting angle of link 1, link i can be brought to a desired position with zero velocity. This procedure can be repeated for other links by unlocking the corresponding joints. Contraction of the arm can be performed by reversing the above deployment procedure. This actuation scheme is scalable in the sense that a single actuator may be used even if more links are added.

The trajectory of the actuated link must be designed such that the unactuated links arrive at a desired position with zero velocity. The motion of the actuated link must also be restricted to a small amplitude about its vertical upright position. This is of utmost importance as the arm operates inside an aircraft wing-box and must remain clear of the access porthole and other obstacles. The design of such trajectories for the actuated link requires a careful consideration of the system dynamics. These issues are addressed in Chapters 4 and 5

2.5 Fixed Axis of Tilt

The simplest underactuated design concept uses a single actuator at the base for deploying the unactuated links of an n-link robot arm. Fig. 2-6 shows a robot arm, where the base link (link 1) may be rotated about a **fixed axis** Z_0 that is orthogonal to the direction of gravity. All other joint axes that are orthogonal to Z_0 are free to rotate unless the brakes are turned on. The simplest deployment scheme is to rotate one joint at a time by unlocking the joint and tilting the base link. All the unactuated links except link i are locked. By controlling the tilting angle of link 1, link i can be brought to a desired position with zero velocity. Link i may be locked thereafter. This procedure can be repeated sequentially for the other unactuated links. Contraction of the arm can be performed by reversing the above deployment procedure.

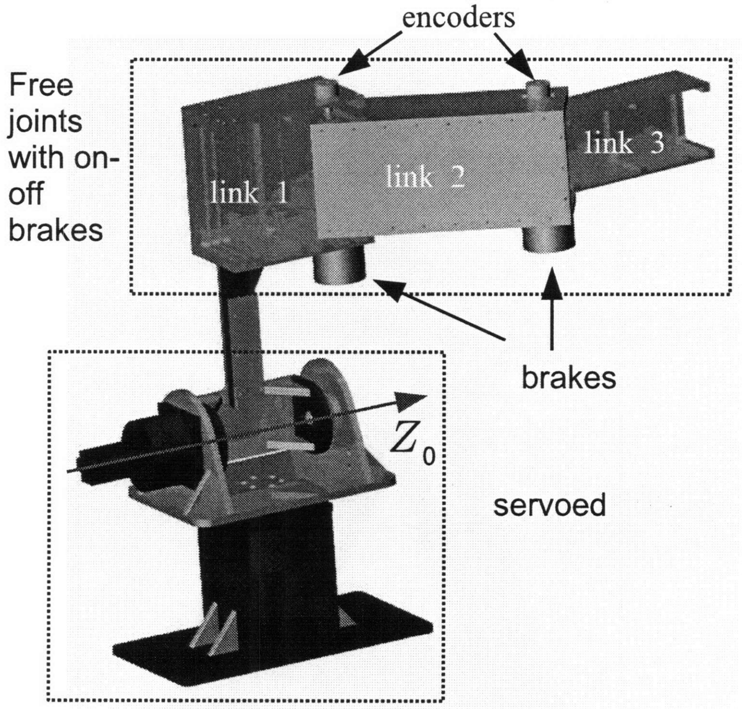

Figure 2-6: Fixed axis of tilt

2.6 Arbitrary Axis of Tilt

We consider another design where the orientation of the axis of tilt may be chosen arbitrarily in the horizontal plane. The gravitational torque on the unactuated joints may be weak in certain configurations if the axis of tilt has a fixed orientation. This additional "input" enables us to improve the speed of response of the unactuated links. Fig. 2-7 shows a schematic of the robot arm mounted on a Stewart Platform, also known as a hexapod. Z_0^* denotes a fixed reference direction in the horizontal plane. By coordinating the motion of the six legs of the hexapod, the table may be tilted about an arbitrary axis Z_0 in the horizontal plane.

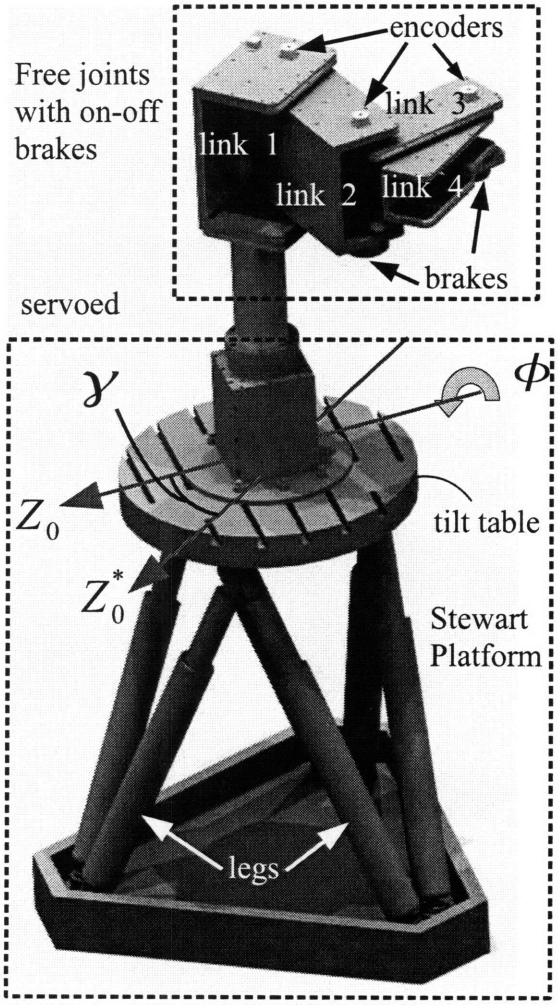

Figure 2-7: Arbitrary axis of tilt using hexapod

The hexapod mechanism may be used for rapid fastener installations. Fig. 2-8(a) shows the location of the end-effecter after the links have been deployed and locked. Fig. 2-8(b) shows the motion of the hexapod table so as to accomplish rapid motion of the end-effecter between successive fastener locations. It may be noted that the motion of the hexapod table is limited by the size of the access porthole. Thus, it is best to reconfigure the arm after a few successive translational motions of the hexapod table.

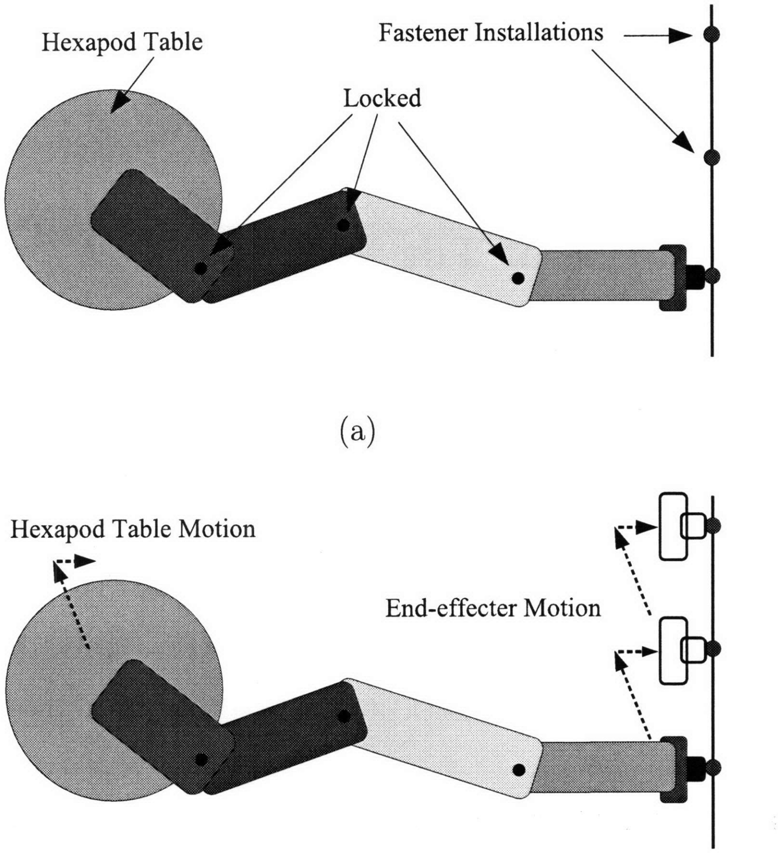

(a)

(b)

Figure 2-8: Rapid fastener installation using hexapod: (a) Initial position after link deployment; (b) Translational motion of hexapod table

Chapter 3

Dynamic Modeling

3.1 Fixed Axis of Tilt

Fig. 3-3 shows a schematic of an n-link robot arm with one actuated (link 1) and $n-1$ unactuated links. $X_0Y_0Z_0$ denotes the World Coordinate Frame. The coordinate frames are attached according to the Denavit-Hartenberg convention with the i^{th} coordinate frame fixed to the i^{th} link. We seek rotation of link i ($i \geq 2$) about the axis Z_{i-1} by rotating link 1 about the horizontal axis Z_0. The angle θ_i denotes the angular displacement of link i relative to link $i-1$. For clarity, the displacement of the first joint (the only servoed joint) tilting link 1 relative to the fixed vertical axis X_0 is denoted by ϕ.

The system dynamics may be written as:

$$\begin{bmatrix} H_{11} & H_{i1} \\ H_{i1} & H_{ii} \end{bmatrix} \begin{bmatrix} \ddot{\phi} \\ \ddot{\theta}_i \end{bmatrix} + \begin{bmatrix} F_1 \\ F_i \end{bmatrix} + \begin{bmatrix} G_1 \\ G_i \end{bmatrix} = \begin{bmatrix} \tau_1 \\ 0 \end{bmatrix} \tag{3.1}$$

$$\theta_j = \theta_{j0} \quad j \neq 1, i \tag{3.2}$$

Here $[H_{kl}(q)]$ is the $n \times n$ symmetric positive-definite inertia matrix, $q = [\theta_2, \ldots, \theta_n]^T$ is the $n-1$ dimensional vector of unactuated joint angles, $[F_1(q, \dot{q}, \dot{\phi}), F_i(q, \dot{q}, \dot{\phi})]^T$ represents the 2×1 vector of centrifugal and Coriolis effects and $[G_1(q, \phi), G_i(q, \phi)]^T$ represents the 2×1 vector of gravitational effects. The torque on the actuated joint

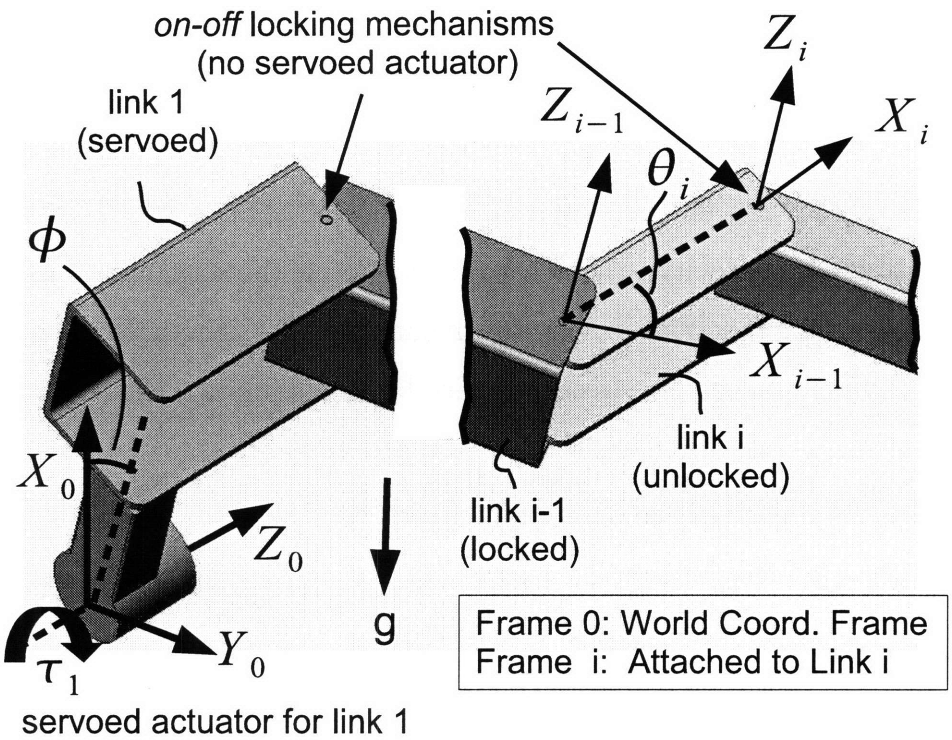

Figure 3-1: Schematic of n-link robot arm: fixed axis of tilt

axis Z_0 is represented by τ_1. We note that θ_{j0} is a constant because the j^{th} link $(j \neq 1, i)$ is locked. As shown in Appendix A, the centrifugal and gravity terms may be written as

$$F_i(q, \dot{q}, \dot{\phi}) = f_i(q)\dot{\phi}^2, \tag{3.3}$$

$$G_i(q, \phi) = g_i(q) g \sin\phi. \tag{3.4}$$

Using (3.3) and (3.4), the second row of (3.1) may be written as:

$$\ddot{\theta}_i = -\frac{H_{i1}(q)}{H_{ii}(q)}\ddot{\phi} - \frac{f_i(q)}{H_{ii}(q)}\dot{\phi}^2 - \frac{g_i(q)}{H_{ii}(q)} g \sin\phi. \tag{3.5}$$

As shown in [15], (3.5) is a 2^{nd} order non-holonomic constraint and thus cannot be integrated to express θ_i as a function of ϕ. Also, at any given time only one unactuated link (link i) is in motion. Thus, the n-link problem can be treated as a 2-link problem without loss of generality. For the 2-link case, we may write (3.5) as:

$$\ddot{\theta}_2 = -\frac{H_{21}(\theta_2)}{H_{22}(\theta_2)}\ddot{\phi} - \frac{f_2(\theta_2)}{H_{22}(\theta_2)}\dot{\phi}^2 - \frac{g_2(\theta_2)}{H_{22}(\theta_2)} g \sin\phi, \tag{3.6}$$

The expressions for H_{21} etc. are given in Appendix A.

The position (ϕ), velocity ($\dot{\phi}$) and acceleration ($\ddot{\phi}$) of the actuated coordinate may be viewed as forcing functions driving the dynamics of the unactuated coordinate θ_2. These forcing functions may be freely specified by an appropriate choice of the control input τ_1 in (3.1). In particular, let $\phi_d(t)$ be a desired trajectory for the actuated coordinate. The control torque τ_1 may be chosen as

$$\tau_1 = \frac{\ddot{\phi}_d}{N_{11}} + F_1 + G_1 + \frac{N_{12}}{N_{11}}(F_2 + G_2), \tag{3.7}$$

where $[N_{ij}] = [H_{ij}]^{-1}$. This gives rise to the dynamics $\ddot{\phi} = \ddot{\phi}_d$, as desired. In view of these arguments, we refer to ϕ and its derivatives ($\dot{\phi}, \ddot{\phi}$) in (3.6) as the *pseudo input.* The terms involving θ_2 in (3.6), i.e. H_{12}/H_{22}, f_2/H_{22} and g_2/H_{22}, are referred to as the *modulating coefficients.* These *modulating coefficients* scale the various components of the *pseudo input* ($\phi, \dot{\phi}, \ddot{\phi}$) depending on the position of the unactuated link 2.

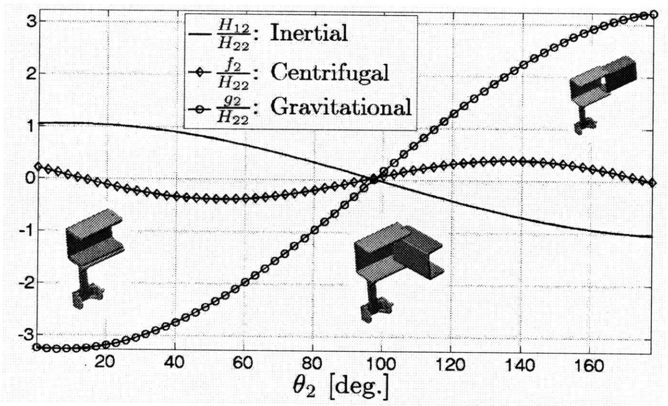

Figure 3-2: Comparison of modulating coefficients over configuration space

Fig. 3-2 shows the variation of the dimensionless *modulating coefficients* in the configuration space (0° to 180°) of the unactuated coordinate. The simulation is based on parameter values taken from a 2-link version of our prototype system shown in Fig.

6-1. The dominant term is the modulating coefficient due to gravity (g_2/H_{22}), followed by the contribution of the inertial coupling (H_{12}/H_{22}) and finally the contribution of the centrifugal coupling (f_2/H_{22}). In view of these observations, we make the following assumptions:

1. Inertial coupling is neglected.
2. Centrifugal coupling is neglected.

These assumptions are valid as long as the gravitational component of acceleration $|g \sin \phi|$ is of the same (or higher) order of magnitude as compared to $|\ddot{\phi}|$ and $|\dot{\phi}^2|$. We validate these approximations *a posteriori* in the section on experimental results. Under these assumptions, the dynamics (3.6) may be simplified as:

$$\ddot{\theta}_2 = -\frac{g_2(\theta_2)}{H_{22}} g \sin \phi \tag{3.8}$$

Using (A.3) and (A.7), we may write (3.8) as:

$$\ddot{\theta} = A \sin \theta \sin \phi, \tag{3.9}$$

where

$$\begin{aligned} \theta &= \theta_2 + \alpha, \\ A &= \frac{M_2 g \sqrt{y_{c2}^2 + (x_{c2} + a_2)^2}}{I_{zz2} + M_2(y_{c2}^2 + (x_{c2} + a_2)^2)}, && (3.10) \\ \alpha &= \operatorname{atan2}(y_{c2}, x_{c2} + a_2). && (3.11) \end{aligned}$$

Remark 3.1.1. *It is worthwhile to examine the physical significance of the dynamics (3.9). It represents a pendulum in a modulated "gravity" field. For a fixed value of ϕ, the quantity A may be identified with the square of the natural frequency. The strength of this field can be modulated as $A \sin \phi$ by controlling the angle ϕ. The pendulum behaves as a regular or inverted pendulum depending on the sign of $\sin \theta \sin \phi$. Also, the "gravity" field may be switched off by setting $\phi = 0$. This gives rise to a continuum* *of equilibria given by* $[\theta = \bar{\theta}, \dot{\theta} = 0, \phi = 0]$, *where* $\bar{\theta}$ *is arbitrary.*

Remark 3.1.2. *Although inertial and centrifugal terms have been neglected in (3.9), the dynamical system is still second-order non-holonomic. The gravity term is a function of the generalized coordinates* θ *and* ϕ. *Therefore it satisfies the conditions for* 2^{nd} *order non-holonomic systems stated in [15].*

Remark 3.1.3. *The inertial effects have the same significance relative to the centrifugal effects [4]. Thus, it is consistent to neglect both inertial and centrifugal effects in the system dynamics.*

3.2 Arbitrary Axis of Tilt

3.2.1 Sequential Link Deployment

Fig. 3-3 shows a schematic of an n-link robot arm with one actuated (link 1) and $n-1$ unactuated links. $X_0^* Y_0^* Z_0^*$ denotes the World Coordinate Frame, with the axis Z_0^* being normal to the direction of gravity. The coordinate frames are attached according to the Denavit-Hartenberg convention with the i^{th} coordinate frame fixed to the i^{th} link. We seek rotation of link i ($i \geq 2$) about the axis Z_{i-1} by rotating link 1 about the horizontal axis Z_0. The angle γ denotes the orientation of the axis Z_0 with respect to Z_0^*. The angle θ_i denotes the angular displacement of link i relative to link $i-1$. For clarity, the displacement of the first joint (the only servoed joint) tilting link 1 about the horizontal axis Z_0 is denoted by ϕ.

$$\begin{bmatrix} H_{11} & H_{i1} \\ H_{i1} & H_{ii} \end{bmatrix} \begin{bmatrix} \ddot{\phi} \\ \ddot{\theta}_i \end{bmatrix} + \begin{bmatrix} F_1 \\ F_i \end{bmatrix} + \begin{bmatrix} G_1 \\ G_i \end{bmatrix} = \begin{bmatrix} \tau_1 \\ 0 \end{bmatrix} \tag{3.12}$$

$$\theta_j = \theta_{j0} \quad j \neq 1, i \tag{3.13}$$

Here $[H_{kl}(q, \gamma)]$ is the $n \times n$ symmetric positive-definite inertia matrix, $q = [\theta_2, \ldots, \theta_n]^T$ is the $n-1$ vector of unactuated joint angles, $[F_1(q, \gamma, \dot{q}, \dot{\phi}), F_i(q, \gamma, \dot{q}, \dot{\phi})]^T$ represents

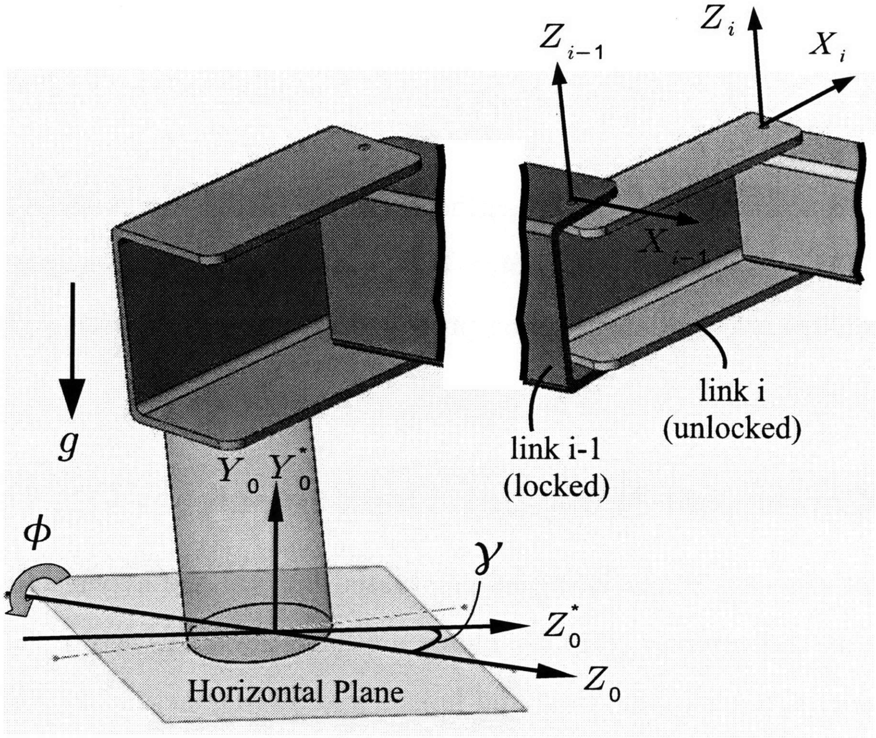

Figure 3-3: Schematic of n-link arm: arbitrary axis of tilt

the 2×1 vector of centrifugal and Coriolis effects and $[G_1(q, \gamma, \phi), G_i(q, \gamma, \phi)]^T$ represents the 2×1 vector of gravitational effects. The torque on the actuated joint axis Z_0 is represented by τ_1. We note that θ_{j0} is a constant because the j^{th} link $(j \neq 1, i)$ is locked. The second row of (3.12) may be written as:

$$\ddot{\theta}_i = -h_{i1}(q, \gamma)\ddot{\phi} - f_i(q, \gamma)\dot{\phi}^2 - g_i(q, \gamma)\sin\phi. \tag{3.14}$$

Here

$$h_{i1}(q, \gamma) = \frac{H_{i1}(q, \gamma, \dot{q}, \dot{\phi})}{H_{ii}(q)} \tag{3.15}$$

$$f_i(q, \gamma)\dot{\phi}^2 = \frac{F_i(q, \gamma, \dot{q}, \dot{\phi})}{H_{ii}(q)} \tag{3.16}$$

$$g_i(q, \gamma)\sin\phi = \frac{G_i(q, \gamma, \phi)}{H_{ii}(q)} \tag{3.17}$$

As with the fixed axis of tilt, the quantity $g_i(q, \gamma)$ may be written as

$$g_i(q, \gamma) = -A_i \sin(\theta_i - \gamma + \alpha_i) \tag{3.18}$$

The parameters A_i and α_i may be identified with the parameters A and α respectively in (3.10)-(3.11). As shown in Chapter 4, this structure in the gravitational effects greatly simplifies the motion planning problem when the orientation γ of the axis of tilt may be chosen freely.

3.2.2 Concurrent Multi-link Deployment

We consider the case where multiple unactuated links of the hyper-articulated arm are in motion concurrently. Fig. 3-4 shows a schematic of this setup. As usual, link 1 (not shown) is the actuated link, and links 2 and 3 are unactuated. The axis of tilt is located on the horizontal plane and is denoted by Z_0. It is oriented at an angle γ with respect to the link 1 frame X_1Y_1. The points C_2 and C_3 denote the locations of the center of mass of links 2 and 3 respectively. The masses of links 2 and 3 are denoted by m_2 and m_3 respectively. I_{zz2} and I_{zz3} denote the centroidal inertias of links 2 and 3 respectively.

Lagrange's equations of motion for the unactuated links may be written as

$$\frac{d}{dt}\left(\frac{\partial T_0}{\partial \dot{q}}\right) - \frac{\partial T_0}{\partial q} + \frac{\partial V}{\partial q} = 0. \tag{3.19}$$

Here $q = [\theta_2, \theta_3]^T$ denotes the 2 dimensional vector of unactuated coordinates, $T_0(\phi, q, \dot{\phi}, \dot{q})$ denotes the kinetic energy and $V(\phi, \gamma, q)$ the potential energy of the system.

As with the single link case, we make the following assumptions:

1. Centrifugal and Coriolis coupling with link 1 (actuated link) is negligible.
2. Inertial coupling with link 1 is negligible.

It may be noted that the inertial coupling between links 2 and 3, as well as the centrifugal and Coriolis effects within the plane of links 2 and 3 are retained. Effectively, we may approximate T_0 by $T(q, \dot{q})$, the kinetic energy of a double pendulum system in a fixed plane. The "fixed" plane instantaneously makes an angle ϕ with the horizontal plane. We retain the gravitational effects in $V(\phi, \gamma, q)$. We essentially end up with a double pendulum whose dynamics is modulated by gravity through a choice of the axis of tilt Z_0 (in the horizontal plane) and the tilt angle ϕ.

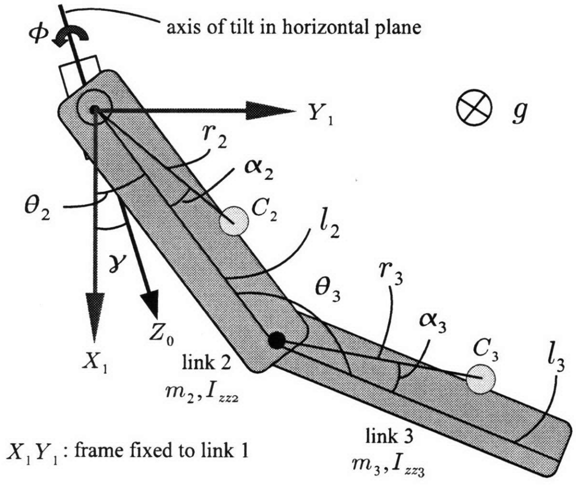

Figure 3-4: Double pendulum in modulated gravity field

The kinetic energy of the double pendulum system may be written as

$$\begin{aligned} T =& \sum_{i=2}^{3} \frac{1}{2} m_i v_{ci}^T v_{ci} + \frac{1}{2} I_{zzi} \omega_i^2 \\ =& \frac{1}{2}(m_2 r_2^2 \dot{\theta}_2^2 + m_3(l_2^2 \dot{\theta}_2^2 + r_3^2(\dot{\theta}_2 - \dot{\theta}_3)^2 - 2 l_2 r_3 \cos(\theta_3 - \alpha_3) \dot{\theta}_2 (\dot{\theta}_2 - \dot{\theta}_3)) \\ &+ \frac{1}{2}(I_{zz2} \dot{\theta}_2^2 + I_{zz3}(\dot{\theta}_2 - \dot{\theta}_3)^2). \end{aligned} \tag{3.20}$$

The potential energy may be written as

$$\begin{aligned} V =& m_2 g r_2 \sin(\theta_2 + \alpha_2 - \gamma) \sin\phi \\ &+ m_3 g (l_2 \sin(\theta_2 - \gamma) - r_3 \sin(\theta_2 - \theta_3 + \alpha_3 - \gamma)) \sin\phi. \end{aligned} \tag{3.21}$$

Using (3.20) and (3.21) in (3.19), the system dynamics for this approximate model may be written as:

$$H(q)\ddot{q} + C(q,\dot{q}) + G(\phi,\gamma,q) = 0. \tag{3.22}$$

Here

$$\begin{aligned}
H &= \begin{bmatrix} H_{22} & H_{23} \\ H_{23} & H_{33} \end{bmatrix}, \\
H_{22}(q) &= m_2 r_2^2 + m_3(l_2^2 + r_3^2 - 2 l_2 r_3 \cos(\theta_3 - \alpha_3)) + I_{zz2} + I_{zz3}, \\
H_{23}(q) &= m_3 r_3 (l_2 \cos(\theta_3 - \alpha_3) - r_3), \\
H_{33}(q) &= m_3 r_3^2 + I_{zz3}, \\
G_2(\phi,\gamma,q) &= (m_2 r_2 \cos(\theta_2 + \alpha_2 - \gamma) \\
&\quad - m_3(r_3 \cos(\theta_2 - \theta_3 + \alpha_3 - \gamma) - l_2 \cos(\theta_2 - \gamma))) g \sin\phi, \\
G_3(\phi,\gamma,q) &= m_3 r_3 \cos(\theta_2 - \theta_3 + \alpha_3 - \gamma) g \sin\phi, \\
C(q,\dot{q}) &= \dot{H}\dot{q} - \frac{\partial T}{\partial q}.
\end{aligned}$$

This dynamical model is used as the basis of our concurrent multi-link deployment algorithms presented in Section 4.2.1.

3.3 Controllability Analysis

In this section, we address the controllability of our proposed underactuated system with respect to the input torque τ_1. Our goal is to steer each unactuated link from an arbitrary initial position to an arbitrary desired final position with zero final velocity. In other words, we wish to ascertain the existence of an input torque for the steering process. We first analyze the case of sequential link deployment using a fixed axis of tilt. Next, we analyze concurrent multi-link deployment using an arbitrary axis of tilt.

3.3.1 Sequential Link Deployment

The state space model for sequential link deployment using a fixed axis of tilt is given by (3.1). After some rearrangement, (3.1) may be written as

$$\begin{bmatrix} \ddot{\phi} \\ \ddot{\theta}_i \end{bmatrix} = - \begin{bmatrix} N_{11} & N_{i1} \\ N_{i1} & N_{ii} \end{bmatrix} \begin{bmatrix} F_1 + G_1 \\ F_i + G_i \end{bmatrix} + \begin{bmatrix} N_{11} \\ N_{1i} \end{bmatrix} \tau_1, \tag{3.23}$$

where $[N_{ij}] = [H_{ij}]^{-1}$.

The system dynamics (3.23) is non-linear and its global controllability cannot be checked directly. We linearize (3.23) about an operating point in the state space and check the controllability of the linearized system. If the linearized system is controllable, then it is guaranteed that the non-linear system is *locally controllable* around that operating point. If the linearization is controllable at *every* point in the state space, then the non-linear system is *globally controllable.*

Let us define $x \triangleq [\dot{\phi}, \dot{\theta}_i, \phi, \theta_i]^T$. The operating point is chosen as $(x, \tau_1) = ([0, 0, 0, \bar{\theta}_i]^T, \bar{\tau}_1)$. Physically, this corresponds to the upright ($\phi = 0$) equilibrium position for link 1 and an arbitrary equilibrium position ($\theta_i = \bar{\theta}_i$) for link i. The nominal torque to keep the system in this equilibrium position is denoted by $\bar{\tau}_1$. The linearization of (3.23) about $(x, \tau_1) = ([0, 0, 0, \bar{\theta}_i]^T, \bar{\tau}_1)$ can be written as

$$\begin{bmatrix} \delta\ddot{\phi} \\ \delta\ddot{\theta}_i \\ \delta\dot{\phi} \\ \delta\dot{\theta}_i \end{bmatrix} = \begin{bmatrix} 0 & 0 & A_{13} & A_{14} \\ 0 & 0 & A_{23} & A_{24} \\ 1 & 0 & 0 & 0 \\ 0 & 1 & 0 & 0 \end{bmatrix} \begin{bmatrix} \delta\dot{\phi} \\ \delta\dot{\theta}_i \\ \delta\phi \\ \delta\theta_i \end{bmatrix} + \begin{bmatrix} N_{11} \\ N_{1i} \\ 0 \\ 0 \end{bmatrix} \delta\tau \tag{3.24}$$

Here

$$A_{13} = -N_{11}\frac{\partial G_1}{\partial \phi} - N_{1i}\frac{\partial G_i}{\partial \phi} \tag{3.25}$$

$$A_{14} = -N_{11}\frac{\partial G_1}{\partial \theta_i} \tag{3.26}$$

$$A_{23} = -N_{1i}\frac{\partial G_1}{\partial \phi} - N_{ii}\frac{\partial G_i}{\partial \phi} \tag{3.27}$$

$$A_{24} = -N_{1i}\frac{\partial G_1}{\partial \theta_i} \tag{3.28}$$

The controllability matrix is given by:

$$\begin{aligned} \Lambda &= \begin{bmatrix} B & AB & A^2B & A^3B \end{bmatrix} \\ &= \begin{bmatrix} N_{11} & 0 & A_{13}N_{11} + A_{14}N_{1i} & 0 \\ N_{1i} & 0 & A_{23}N_{11} + A_{24}N_{1i} & 0 \\ 0 & N_{11} & 0 & A_{13}N_{11} + A_{14}N_{1i} \\ 0 & N_{1i} & 0 & A_{23}N_{11} + A_{24}N_{1i} \end{bmatrix} \end{aligned}$$

The controllability matrix Λ is singular *iff*

$$\det(\Lambda) = 0$$

$$\Rightarrow N_{11}(N_{11}A_{23} - N_{1i}A_{13}) - N_{1i}(N_{1i}A_{14} - N_{11}A_{24}) = 0. \tag{3.29}$$

Using (3.25) - (3.28) and (3.4), (3.29) reduces to

$$\begin{aligned} \frac{\partial G_i}{\partial \phi} &= 0 \\ \Rightarrow g_i &= 0. \end{aligned}$$

The linearized analysis indicates that the system (3.1) is locally controllable at all points in the state space of the form $x = [0, 0, 0, \theta_i]^T$ except when $\theta_i = \theta_i^*$, such that $g_i(\theta_i^*) = 0$. The physical interpretation of this condition is that the gravitational torque is identically zero, i.e., the axis of tilt is orthogonal to the plane containing the center of mass of the free link and the corresponding free joint axis. The linearized analysis is inconclusive at this point.

A non-linear analysis is required to check the controllability of (3.1) at $x = [0,0,0,\theta_i^*]^T$. We wish to check the *Small Time Local Controllability (STLC)* of (3.1) at $x^* = [0,0,0,\theta_i^*]^T$. We note that the nominal torque required to keep the system at equilibrium at x^* is given by $\tau^* = G_1(x^*)$. Let $\tau = \tau_1 - \tau^*$. Then, we can rewrite (3.1) as:

$$\dot{x} = f(x) + g(x)u \tag{3.30}$$

Equation (3.30) is in the standard form $\dot{x} = f(x) + g(x)u$ such that $f(x^*) = 0$. Let us consider repeated Lie brackets containing f and g, e.g. $[f,[g,[f,g]]]$. Following Sussmann [20], for a Lie bracket B, we define $\delta_0(B)$ and $\delta_1(B)$ to be the number of times f and g appear in B respectively. The degree of B is defined as $\delta(B) = \delta_0(B) + \delta_1(B)$. If $\delta_0(B)$ is odd and $\delta_1(B)$ is even, then B is called a *bad* bracket. A bracket is *good* if it is not *bad.* Thus $[f,[g,[f,g]]]$ has degree 4 and is a good bracket.

Sussmann's sufficient conditions for *STLC* of (3.30) are:

1. The system satisfies the **Lie Algebra Rank Condition (LARC)**.
2. Every bad bracket is a linear combination of good brackets of lower degree.

Condition 1 also implies that the system (3.30) is *locally accessible.* A system is said to be *locally accessible* at x^*, if it can reach an open set starting at x^*. The *local controllability* condition is stronger and requires the open set to contain a neighborhood of x^*. We consider the following set of Lie brackets to check this:

$$L = \{g, [f,g], [g,[f,g]], [f,[g,[f,g]]]\} \tag{3.31}$$

Appendix B shows that the brackets in L satisfy the *LARC.* Thus the system is locally accessible. Also, we note that L has brackets up to degree 4. Thus, the only *bad* brackets we are concerned about are f and $[g,[f,g]]$. The *good* brackets of lower degree are g and $[f, g]$. Once again, from Appendix B, it may be verified that the good brackets do not span the bad brackets.

We further check that the **Hermes necessary condition (HNC)** [20] for local controllability is satisfied at x^*, i.e.,

$$[g, [f, g]] \in \operatorname{span}\{f, g, [f, [f, g]]\}. \tag{3.32}$$

Appendix B shows that this necessary condition is satisfied. The conclusion of the non-linear analysis is that the system is *locally accessible.* Intuitively, this ensures that we can "get out" of the singular configuration. However, the non-linear analysis is also inconclusive in ascertaining the *local controllability* of the system.

Remark 3.3.1. *The linearized controllability analysis is conclusive if the orientation* γ *of the axis of tilt may be chosen arbitrarily. From (3.18), it may be noted that it is always possible to choose* γ *such that* $g_i(\gamma, \theta_i) \neq 0$. *In a sense, the control problem involving an arbitrary axis of tilt is more straightforward than the case of a fixed axis of tilt. This is expected, as the orientation* γ *serves as an additional input.*

3.3.2 Concurrent Multi-link Deployment

In this section, we wish to ascertain the feasibility of concurrent multi-link deployment. We first perform a linearized controllability analysis on the approximate dynamical model (3.22) and then provide a physical interpretation of the result. The key observation is that the effective direction of gravity is orthogonal to the orientation of the axis of tilt. Indeed, the effective direction of gravity can be chosen arbitrarily by choosing an appropriate orientation of the axis of tilt.

Linearized Analysis

We check the sufficient condition for local controllability by linearizing the system dynamics (3.22) about an equilibrium point in the state space. Let us define the state as $x = [\dot{\theta}_2, \dot{\theta}_3, \theta_2, \theta_3]^T$. It is convenient to redefine the inputs ϕ and γ as

$$u \triangleq [\phi_x, \phi_y]^T \triangleq [\phi \cos\gamma, \phi \sin\gamma]^T \tag{3.33}$$

We linearize the system dynamics (3.22) about $(\dot{\theta}_2, \dot{\theta}_3, \theta_2, \theta_3, \phi_x, \phi_y) = (0, 0, \bar{\theta}_2, \bar{\theta}_3, 0, 0)$, where $\bar{\theta}_2$, and $\bar{\theta}_3$ are arbitrary. The linearization is given by:

$$\delta\ddot{x} = A\delta x - B\delta u, \tag{3.34}$$

where

$$A \triangleq \begin{bmatrix} \multicolumn{2}{c}{0_{2\times 4}} \\ I_{2\times 2} & 0_{2\times 2} \end{bmatrix}, \quad B \triangleq \begin{bmatrix} N_{22}g_{23x} + N_{23}g_{3x} & N_{22}g_{23y} + N_{23}g_{3y} \\ N_{23}g_{23x} + N_{33}g_{3x} & N_{23}g_{23y} + N_{33}g_{3y} \\ \multicolumn{2}{c}{0_{2\times 2}} \end{bmatrix}.$$

Here

$$[N] = [H]^{-1} \tag{3.35}$$

$$g_{23x} = m_2 g r_2 \cos(\theta_2 + \alpha_2) - m_3 g (r_3 \cos(\theta_2 - \theta_3 + \alpha_3) - l_2 \cos\theta_2) \tag{3.36}$$

$$g_{23y} = m_2 g r_2 \sin(\theta_2 + \alpha_2) - m_3 g (r_3 \sin(\theta_2 - \theta_3 + \alpha_3) - l_2 \sin\theta_2) \tag{3.37}$$

$$g_{3x} = m_3 g r_3 \cos(\theta_2 - \theta_3 + \alpha_3) \tag{3.38}$$

$$g_{3y} = m_3 g r_3 \sin(\theta_2 - \theta_3 + \alpha_3) \tag{3.39}$$

The controllability matrix in this case is given by

$$\begin{aligned} P &= \begin{bmatrix} B & AB & A^2B & A^3B \end{bmatrix} \\ &= \left[\begin{array}{cccc|c} B_{11} & B_{12} & 0 & 0 & \\ B_{21} & B_{22} & 0 & 0 & \\ 0 & 0 & B_{11} & B_{12} & 0_{4\times 4} \\ 0 & 0 & B_{21} & B_{22} & \end{array}\right]. \end{aligned} \tag{3.40}$$

Using the **Kalman rank condition**, the system is not controllable *iff*

$$\begin{aligned} B_{11}B_{22} - B_{12}B_{21} &= 0 \\ \Rightarrow (N_{22}N_{33} - N_{23}^2)(g_{23x}g_{3y} - g_{3x}g_{23y}) \\ \Rightarrow \frac{g_{23y}}{g_{23x}} &= \frac{g_{3y}}{g_{3x}}. \end{aligned} \tag{3.41}$$

Thus, the dynamical system (3.22) satisfies the sufficient condition for local controllability, except in certain special configurations in the state space. A non-linear analysis using Sussmann's sufficient conditions [20] may be conclusive in such configurations.

Physical Interpretation

In this section, we present an intuitive understanding of the controllability analysis from the previous section. See Fig. 3-5. The point C_{23} denotes the combined center-of-mass of links 2 and 3. The point C_3 denotes the location of the center-of-mass of link 3. The goal is to achieve *in-phase* and *out-of-phase* steering for the free links. We define *in-phase* steering as the case where links 2 and 3 move in the same direction, viz. clockwise or counter-clockwise. Similarly, we define *out-of-phase* steering as the case where links 2 and 3 move in opposite directions.

Fig. 3-5(a) shows the choice of the orientation γ of the tilt axis O_2Z_0, such that *in-phase* steering may be achieved. The effective direction of gravity in the instantaneous plane of motion is given by OG. It may be noted that OG is orthogonal to O_2Z_0. The direction O_2G_2 (respectively, O_3G_3) is parallel to OG and denotes the direction of gravity as viewed from joint 2 (respectively, 3). It is evident from the figure that the gravitational torques on the free joints enable *in-phase* steering. Similarly, Fig. 3-5(b) shows the choice of the orientation γ of the tilt axis O_2Z_0, such that *out-of-phase* steering may be achieved.

The condition (3.41) corresponds to the case where O_2C_{23} and O_3C_3 are *parallel* or *anti-parallel.* When O_2C_{23} and O_3C_3 are *parallel*, the effective direction of gravity is the same relative to links 2 and 3. Thus, *out-of-phase* steering cannot be achieved. Similarly, *in-phase* steering cannot be achieved when O_2C_{23} and O_3C_3 are *anti-parallel.* Indeed, the quantities g_{23x} and g_{23y} in (3.41) may be identified with the x and y coordinates of the combined center-of-mass of links 2 and 3, i.e., the point C_{23}. Similarly, the quantities g_{3x} and g_{3y} may be identified with the x and y coordinates of the center-of-mass of link 3, i.e., the point C_3.

Remark 3.3.2. *Out-of-phase steering may be achieved even when the lines* O_2C_{23} *and* O_3C_3 *are parallel. The intuitive explanation is that the links start moving in phase, but at different rates. Thus, the lines* O_2C_{23} *and* O_3C_3 *are no longer parallel after the onset of motion. At this point, the axis of tilt may be switched to enable out-of-phase steering. A non-linear analysis based on Sussmann's sufficient conditions may be fruitful.*

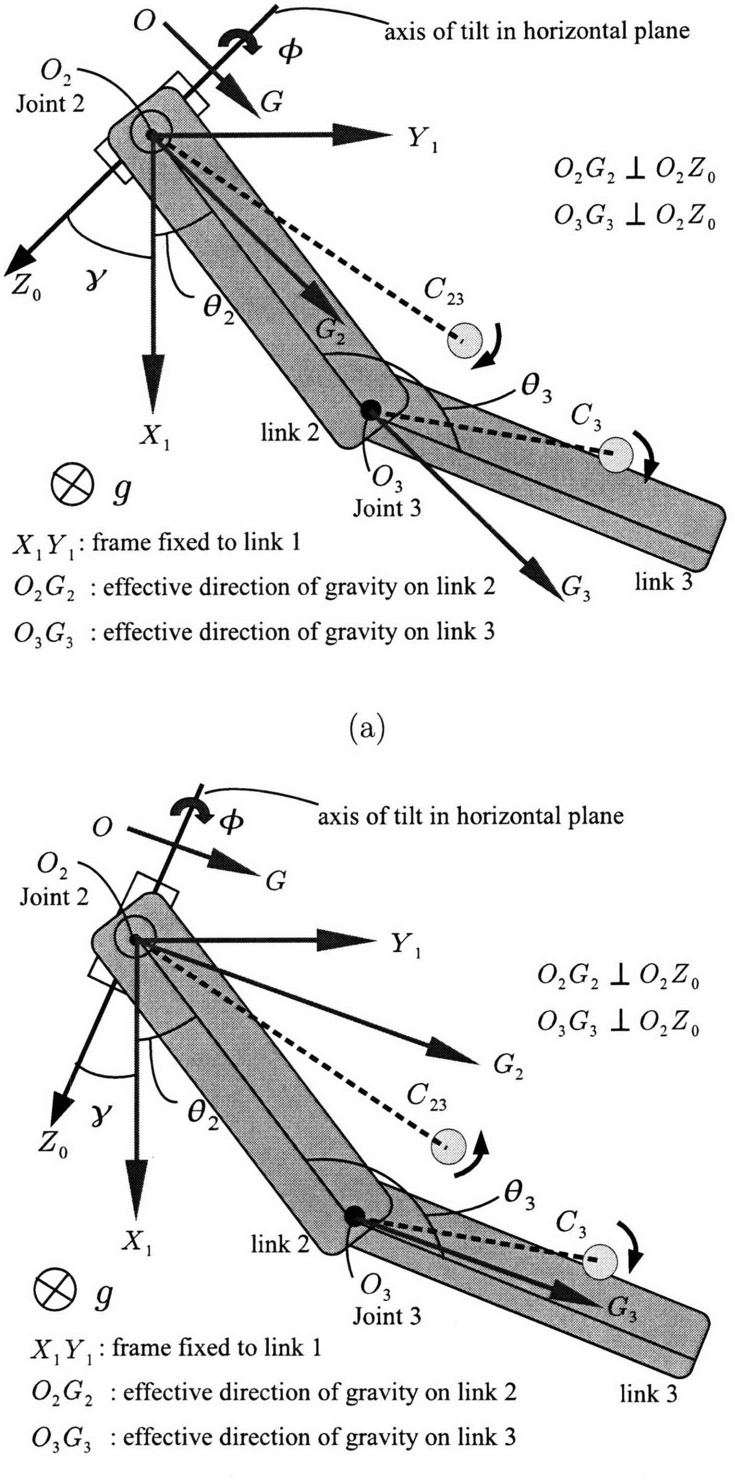

(a)

(b)

Figure 3-5: Multi-link steering: (a) In-phase steering; (b) Out-of-phase steering

Chapter 4

Feed-forward Control

The goal of this chapter is to develop motion-planning algorithms for positioning the links of the robot arm. Since the arm lacks dedicated actuators at the joints, there is no direct means of positioning the links arbitrarily. Instead, the tilt trajectory of the base joint has to be carefully designed so as to move each link (starting at rest) to a desired final position with zero final velocity. Further, the arm operates inside an aircraft wing, and it must be ensured that the amplitude of the tilt trajectory is within reasonable bounds. We develop algorithms for the generation of such tilt trajectories. We first present algorithms for sequential link deployment and extend these results for concurrent multi-link deployment.

4.1 Sequential Link Deployment

In this section we develop motion planning algorithms for the sequential deployment of the unactuated links. At any given time, only one unactuated link is free; all other unactuated links are locked. We first consider an optimal control formulation of the problem with an appropriate cost function. Next, we gather insights from the optimal control solution and propose a parameterized control scheme. The latter scheme generates trajectories which are similar to the optimal control setup, but is computationally superior.

4.1.1 Optimal Control Scheme

We have ascertained the controllability of the system and now we investigate a fixed horizon optimal control approach to generate a control law for the system (3.30). Optimal control approaches have been used for the generation of trajectories of systems involving 1st order non-holonomic constraints [12]. Often, analytical solutions are available for the optimal control problem. It is straightforward to extended the optimal control framework to systems with 2^{nd} order non-holonomic constraints. However, analytical solutions are in general not available and we must use numerical techniques to solve the associated boundary value problem.

The choice of an appropriate cost function is very important in an optimal control framework. The qualitative nature of the solution changes depending on the choice of the cost function. It is common practice to use a measure of control effort, for example, $\int u^2 dt$, as the cost function. However, our application does not necessarily benefit from this choice of cost function. Instead, it is more important for us to restrict the amplitude of the actuated coordinate because the arm operates inside an aircraft wing-box. We would also like to avoid excitation of structural modes of the system through large accelerations of the actuated coordinate. Under these considerations, we choose to minimize the cost function:

$$J_0 = \int_0^{t_f} L(x,u)dt = \int_0^{t_f} \ddot{\phi}^2 dt. \tag{4.1}$$

As before, $x \triangleq [\dot{\phi}, \dot{\theta}_2, \phi, \theta_2]^T$, $u \triangleq \tau_1$ and the state x evolves as

$$\begin{aligned} \dot{x} &= -\begin{bmatrix} -N_{11}(F_1+G_1) - N_{12}(F_2+G_2) \\ -N_{12}(F_1+G_1) - N_{22}(F_2+G_2) \\ \dot{\phi} \\ \dot{\theta}_2 \end{bmatrix} + \begin{bmatrix} N_{11} \\ N_{12} \\ 0 \\ 0 \end{bmatrix} \tau_1 \\ &\triangleq f(x) + g(x)u \end{aligned} \tag{4.2}$$

The expressions for the quantities N_{11}, N_{12} etc. are given in Appendix A.

Introducing Lagrange Multipliers $\lambda = [\lambda_1, \lambda_2, \lambda_3, \lambda_4]^T$, the augmented cost function may be written as:

$$J = \int_0^{t_f} \left(L(x,u) + \lambda^T (f(x) + g(x)u - \dot{x}) \right) dt. \tag{4.3}$$

Using the calculus of variations, the necessary conditions for optimality may be written as:

$$\begin{aligned} \dot{x} &= f(x) + g(x)u && (4.4) \\ \dot{\lambda} &= -\left(\frac{\partial f}{\partial x} + \frac{\partial g}{\partial x} u \right)^T \lambda - \left(\frac{\partial L}{\partial x} \right)^T && (4.5) \\ \frac{\partial L}{\partial u} &= -\lambda^T g(x) && (4.6) \end{aligned}$$

The system of equations (4.4)-(4.6) can be solved as a two point boundary value problem with the following boundary conditions:

$$x(0) = [0,0,0,\theta_{20}]^T, \; x(t_f) = [0,0,0,\theta_{2f}]^T \tag{4.7}$$

We note that the range of motion of θ_2 is 0° (fully folded) to 180° (fully extended). Fig. 4-1 shows the simulation results for $\theta_{20} = 20°$ and $\theta_{2f} = 50°$. It is instructive to compare the results for the cost functions $J_0 = \int_0^{t_f} \ddot{\phi}^2 dt$ and $J_0' = \int_0^{t_f} \tau_1^2 dt$. From Fig. 4-1(a), it is evident that the latter choice of cost function results in a higher amplitude and frequency components in the actuated joint trajectory. Fig. 4-1(b) shows that the unactuated coordinate also displays a large overshoot and oscillatory behavior when the cost function is J_0'. Fig. 4-1(c) shows the corresponding torque profiles. The peak torque is higher for the cost function J_0', but the average torque is lower. As mentioned before, we are interested in a small amplitude of tilt and low frequency of oscillations of the actuated coordinate. Thus, the trajectory obtained using the cost function $J_0 = \int_0^{t_f} \ddot{\phi}^2 dt$ is preferred.

The system of equations (4.4) to (4.7) represents an 8^{th} order boundary value problem. The computation time for this example was approximately 1000ms. If disturbances act on the system during the motion, it may be required to update the motion plan in real time based on actual measurements. The slow computation time makes the approach unsuitable for this purpose. The convergence of the numerical techniques is also contingent on a "good" initial guess for the actual solution. The guess solution used for the trajectory of the unactuated coordinate is:

$$\bar{\theta}_2(t) = \left(10\left(\frac{t}{t_f}\right)^3 - 15\left(\frac{t}{t_f}\right)^4 + 6\left(\frac{t}{t_f}\right)^5\right)(\theta_{2f} - \theta_{20}) + \theta_{20}. \tag{4.8}$$

The initial guess (4.8) is based on the intuition that the unactuated coordinate should change smoothly between the initial and final positions. The simulated trajectory conforms well to the initial guess when the cost function J_0 is used. However, the trajectory shows a marked deviation when the cost function is J_0'.

4.1.2 Parameterized Control Scheme

In this section, we mitigate the convergence issues of the optimal control approach by solving a reduced order boundary value problem. This reduction is achieved by treating the trajectory of the actuated coordinate as a *pseudo input* in lieu of the torque, which is the true input. This redefinition of the input is justified in (3.7).

We gather insights into the structure of the *pseudo input* from the basic nature of the optimal control solution. From Fig. 4-1(a), we note that the actuated joint trajectory must start from the zero position with zero velocity and return to the zero position with zero velocity at the end of the motion. Further, it undergoes one change of sign during motion. This change of sign is required to first accelerate (from zero initial velocity) and then decelerate the unactuated link to zero final velocity. Using these notions, we construct the trajectory of the actuated joint by smoothly patching together piecewise sigmoid polynomial segments, as shown in Fig. 4-2. Such sigmoid polynomials are the lowest order polynomials which are C^2 and also satisfy the boundary conditions.

We parameterize the tilt trajectory as follows:

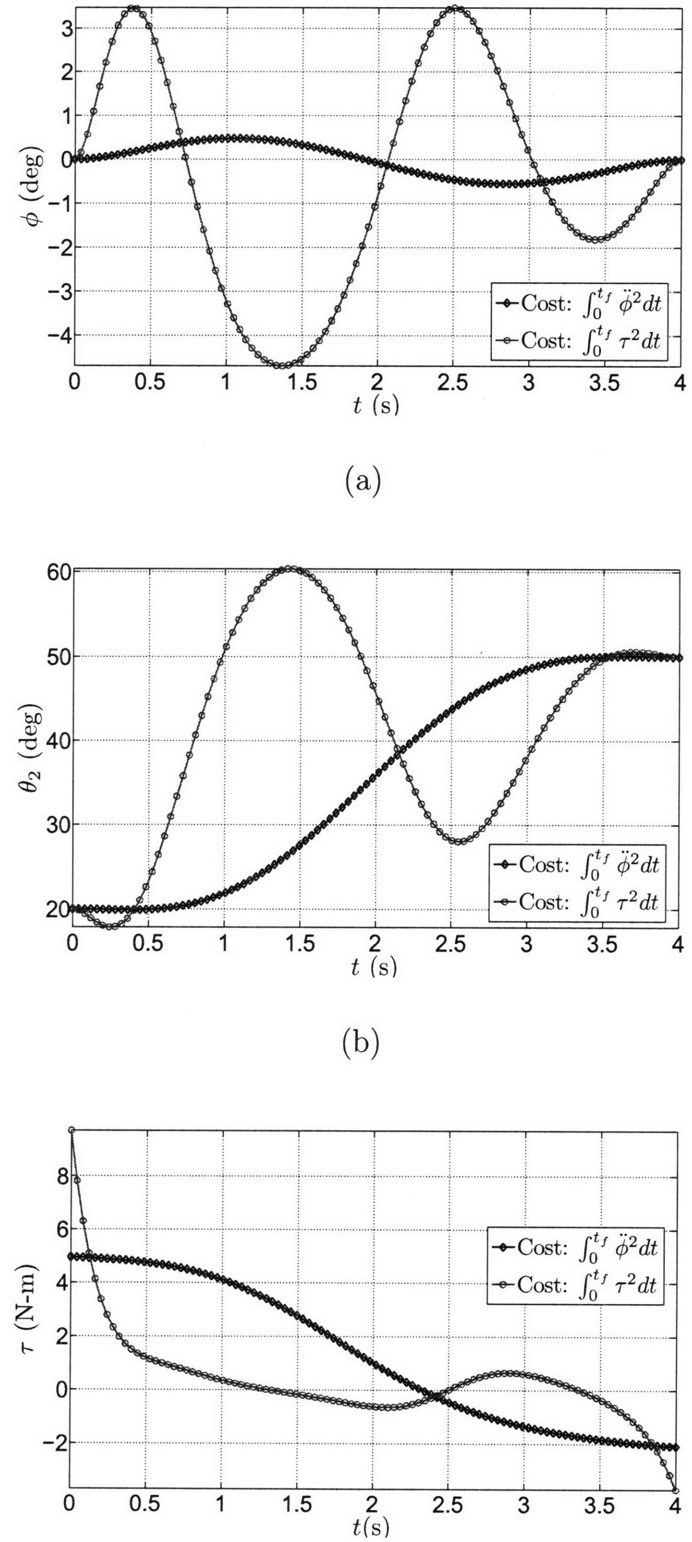

(a)

(b)

(c)

Figure 4-1: Optimal control: (a) Actuated joint trajectory; (b) Unactuated joint trajectory; (c) Joint torque

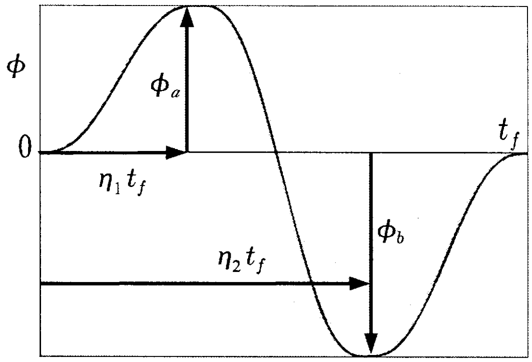

Figure 4-2: Typical parameterized sigmoid trajectory

$$\phi(t) = \begin{cases} (10\mu^3 - 15\mu^4 + 6\mu^5)\phi_a \\ \mu = \frac{t}{\eta_1 t_f}, \quad 0 \le t \le \eta_1 t_f \\ \\ (10\mu^3 - 15\mu^4 + 6\mu^5)(\phi_a - \phi_b) + \phi_b \\ \mu = \frac{\eta_2 t_f - t}{(\eta_2 - \eta_1)t_f}, \quad \eta_1 t_f \le t \le \eta_2 t_f \\ \\ (10\mu^3 - 15\mu^4 + 6\mu^5)\phi_b \\ \mu = \frac{t_f - t}{t_f - \eta_2 t_f}, \quad \eta_2 t_f \le t \le t_f \end{cases} \tag{4.9}$$

We need to determine the parameters ϕ_a, ϕ_b, η_1, η_2 and t_f of the actuated joint trajectory $\phi(t)$ for desired motions of the unactuated joint $\theta_2(t)$ between θ_{20} and θ_{2f}. We do this by substituting the parameterized *pseudo input* in (3.5) and solving it as a 2 point boundary value problem (bvp). (3.5) becomes a 2nd order bvp with 4 boundary conditions and 5 unknown parameters to be determined. The system is clearly indeterminate. We thus fix 3 of the unknown parameters, viz. η_1, η_2 and t_f, and solve the 2^{nd} order bvp for ϕ_a and ϕ_b. This is motivated by the fact that ϕ_a and ϕ_b are linearly involved parameters if we ignore the weak term associated with $\dot{\phi}^2$.

Further, we note that if $\phi(t)$ is an input trajectory for motion of the unactuated coordinate from θ_{20} to θ_{2f} in time t_f, $\phi'(t) = \phi(t_f - t)$ is the input trajectory for motion from to θ_{2f} to θ_{20} in time t_f. If we choose η_1 and η_2 such that $\eta_1 = 1 - \eta_2$, the parameters for the sigmoid trajectory for retraction are $\eta_1' = \eta_1$, $\eta_2' = \eta_2$, $\phi_a' = \phi_b$ and $\phi_b' = \phi_a$. Thus, we do not need to recompute the parameters of the sigmoid trajectory for retraction of the arm. The parameter t_f may be set to get a desired average speed of motion required for point to point movements.

Fig. 4-3 shows the simulation results for $\theta_{20} = 0°$ and $\theta_{2f} = 60°$. The total duration of motion is set at $t_f = 4s$. We consider two choices of the "fixed" parameters η_1 and η_2. The corresponding parameters ϕ_a and ϕ_b are listed below.

1. $\eta_1 = 0.33$, $\eta_2 = 0.67$: $\phi_a = 1.1°$ and $\phi_b = -1.51°$
2. $\eta_1 = 0.20$, $\eta_2 = 0.50$: $\phi_a = 1.51°$ and $\phi_b = -1.26°$

The computation time for this approach is around 450ms.

Remark 4.1.1. *The trajectory of the actuated coordinate may also be parameterized using other smooth functions in lieu of sigmoidal functions. For example, we may use sinusoidal functions to parameterize $\phi(t)$ as*

$$\phi = \phi_a \sin^3 \omega_1 t \qquad 0 \le t \le t_{f1},\ \omega_1 t_{f1} = \pi \tag{4.10}$$

$$\phi = \phi_b \sin^3 \omega_2 (t - t_{f1}) \qquad t_{f1} \le t \le t_{f2},\ \omega_2 (t_{f2} - t_{f1}) = \pi \tag{4.11}$$

The form of the input function ensures that $\phi(0) = \phi(t_{f2}) = \ddot{\phi}(0) = \ddot{\phi}(t_{f2}) = 0$, which also means that the initial and final accelerations of the unactuated joint are zero. As before, the quantities t_{f1} and t_{f2} are fixed a priori and we determine the unknown parameters ϕ_a and ϕ_b by solving the associated boundary value problem.

4.1.3 Optimal vs. Parameterized Control

It is worthwhile to compare the two solution methodologies vis-a-vis the computational costs and the nature of the solutions. A faster computational time is desirable because it may be necessary to dynamically update the motion plan based on actual measurements. Both approaches result in 2 point boundary value problems (bvp). The parameterization approach results in a 4^{th} order bvp, while the optimal control

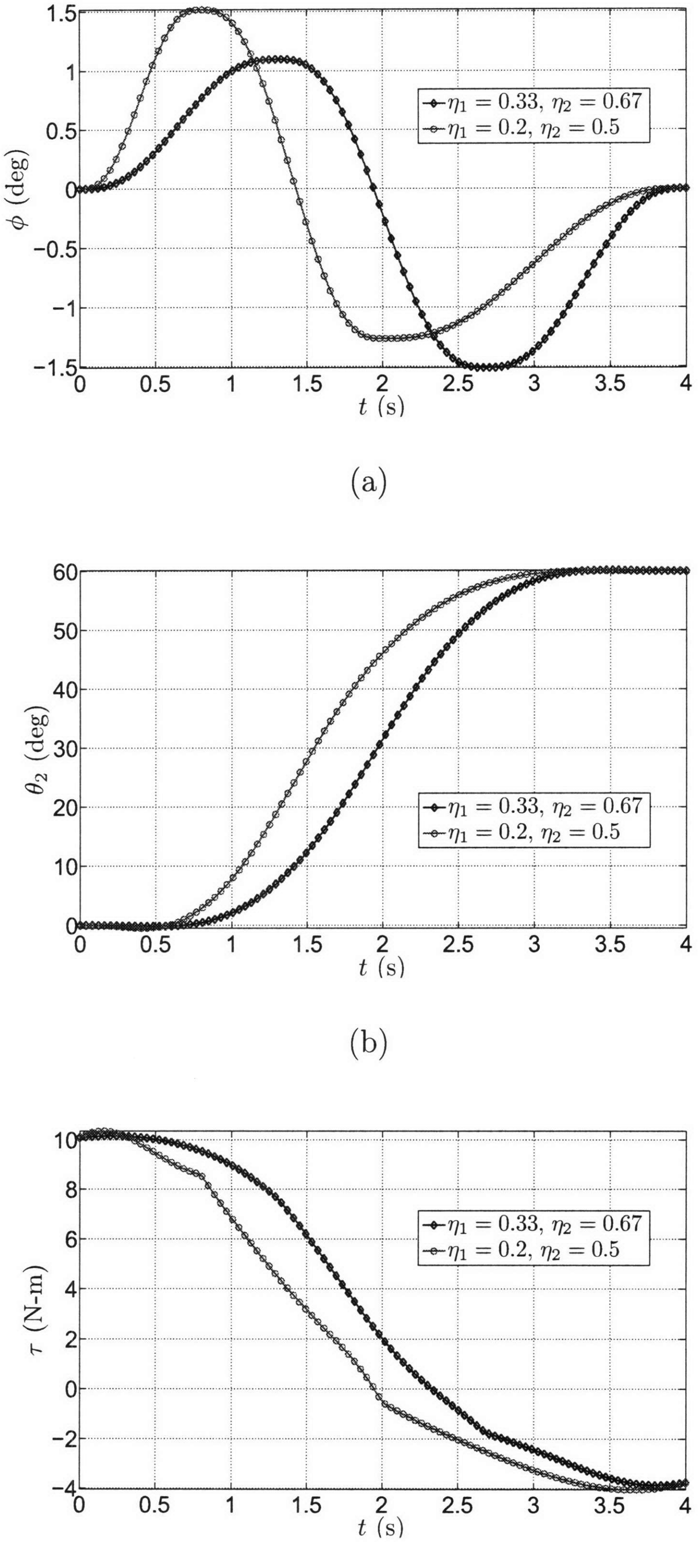

(a)

(b)

(c)

Figure 4-3: Parameterized control: (a) Actuated joint trajectory; (b) Unactuated joint trajectory; (c) Joint torque approach results in an 8^{th} order bvp. The lower order bvp associated with the parameterized formulation results in a 50 percent reduction in the computation time. The use of a sigmoidal parameterization also ensures that the final accelerations of both actuated and unactuated joints are zero. The optimal control approach lack this feature.

The solutions in both approaches are strikingly similar, as seen in Figs. 4-4 and 4-5. Fig. 4-4 shows the case where the *modulating coefficient* $\frac{g_2}{H_{22}}$ (shown in Fig. 3-2), does not change sign during the motion. Thus, the actuated joint has to tilt forward to accelerate the unactuated joint and then tilt backward to decelerate it. As a result, the actuated joint changes sign once during the motion. Fig. 4-4 shows the case where the *modulating coefficient* changes sign (at $\theta_2 \approx 90^\circ$) during the motion. Thus, the actuated joint does not change sign during the motion. These intuitive notions are captured in both numerical approaches.

4.1.4 Arbitrary Axis of Tilt

In this section we consider a deployment scheme where the links of the robot arm are deployed one at a time. The goal is to move link i from an initial position θ_{i0} (relative to link $i-1$) with zero initial velocity to a final position θ_{if} with zero final velocity. By repeating this sequence for each link, the entire arm may be reconfigured. It may be noted that links i to n move as a single rigid body during the motion. The motion planning problem admits an analytical solution if the input is chosen appropriately. The key idea is to design the input so that links i to n emulate the motion of a pendulum in a gravity field.

Fig. 4-6(a) shows the initial configuration of the links and the location of the center of mass of links i to n. Fig. 4-6(b) shows the desired final configuration and the corresponding location of the center of mass. The amplitude of motion is $\Delta\theta_i$. Fig. 4-6(c) shows the choice of the axis of tilt Z_0 in the horizontal plane. The axis of tilt Z_0 is such that the effective direction of gravity is symmetric with respect to the initial and desired final positions of the center of mass. As a result, links i to n move as a pendulum whose equilibrium position is the axis of symmetry of the initial and

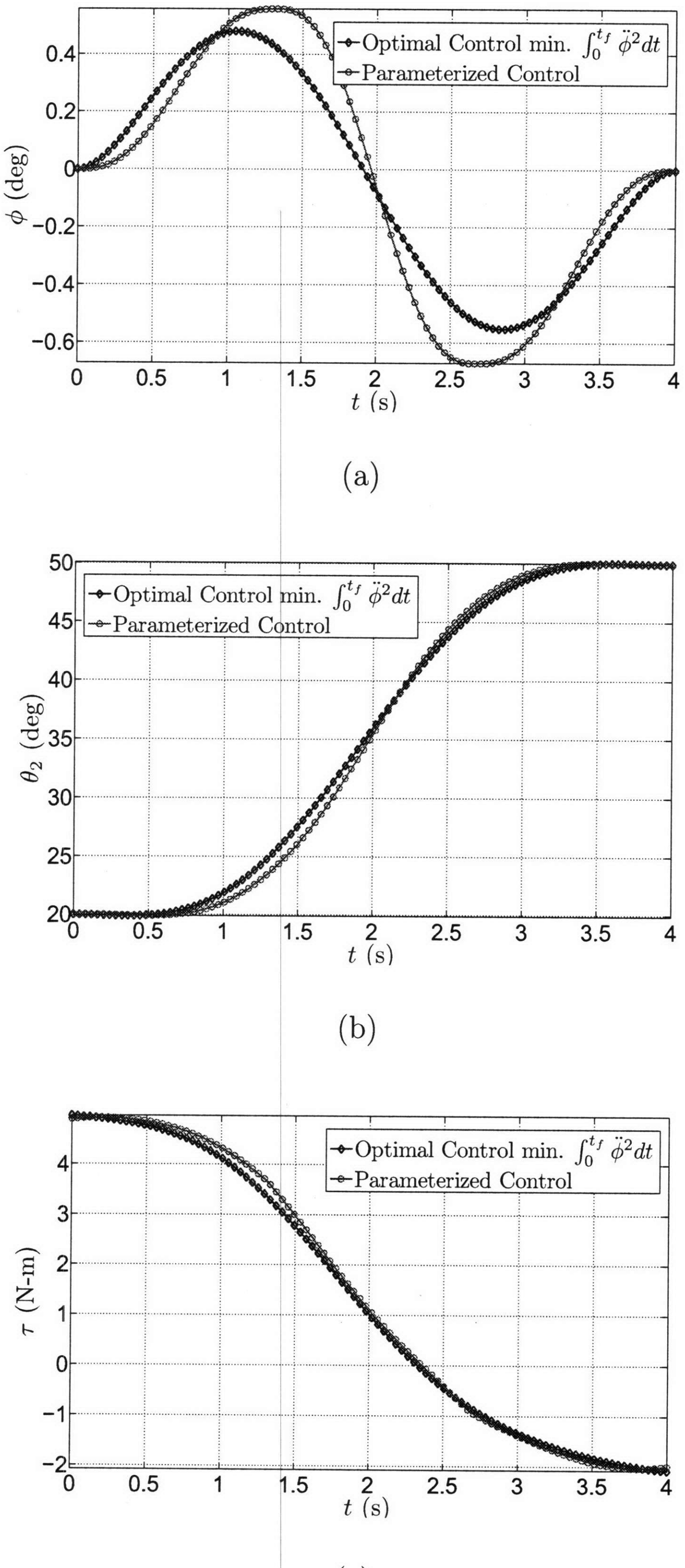

(a)

(b)

(c)

Figure 4-4: Parameterized vs. optimal Control: (a) Actuated joint trajectory; (b) Unactuated joint trajectory; (c) Joint torque

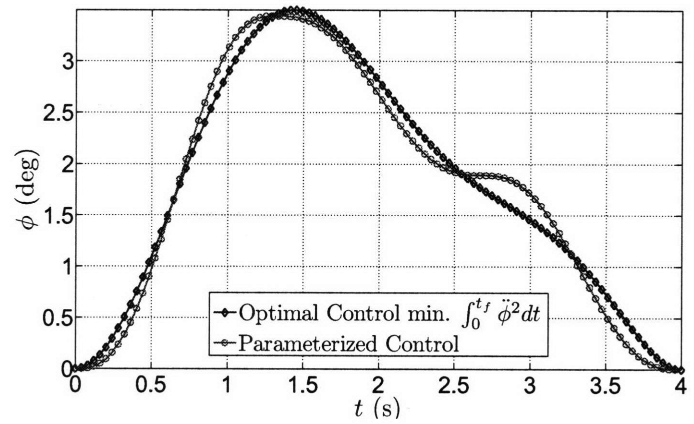

(a)

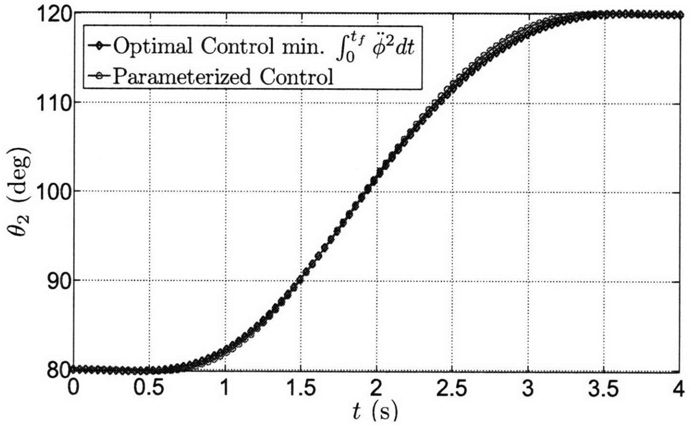

(b)

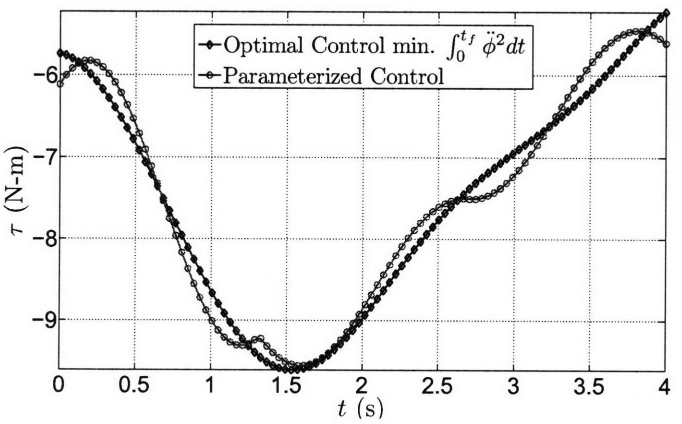

(c)

Figure 4-5: Parameterized vs. optimal control: (a) Actuated joint trajectory; (b) Unactuated joint trajectory; (c) Joint torque desired final positions. Due to symmetry, the pendulum will reach the desired final position with zero velocity.

We may formally arrive at these conclusions from the dynamics represented by (3.14). First, we set the orientation γ of the axis of tilt as

$$\gamma = \alpha_i + \frac{\theta_{i0} + \theta_{if}}{2} \tag{4.12}$$

Next, we set

$$\phi = \phi_0, \ \dot{\phi} = 0 \text{ and } \ddot{\phi} = 0 \tag{4.13}$$

This corresponds to a constant tilt $\phi(t) \equiv \phi_0$ of link 1. Using (4.12) and (4.13) in (3.14), we get

$$\ddot{\theta}_i = A_i \sin(\theta_i - \frac{\theta_{i0} + \theta_{if}}{2}) \sin \phi_0. \tag{4.14}$$

If $\sin(\frac{\theta_{i0}+\theta_{if}}{2}) > 0$ (< 0), we choose ϕ_0 such that $\sin \phi_0 < 0$ (> 0). In either case, (4.14) represents a pendulum whose stable equilibrium position is $\theta_i = \frac{\theta_{i0}+\theta_{if}}{2}$.

The algorithm is summarized below:

1. Determine initial and desired final positions of center of mass of links i to n.
2. Choose axis of tilt (in horizontal plane) orthogonal to the axis of symmetry of initial and desired final positions.
3. Tilt link 1 about chosen axis.
4. Unlock brake to free link i.
5. Lock brake when arm reaches zero velocity.
6. Tilt link 1 back to vertical upright position.

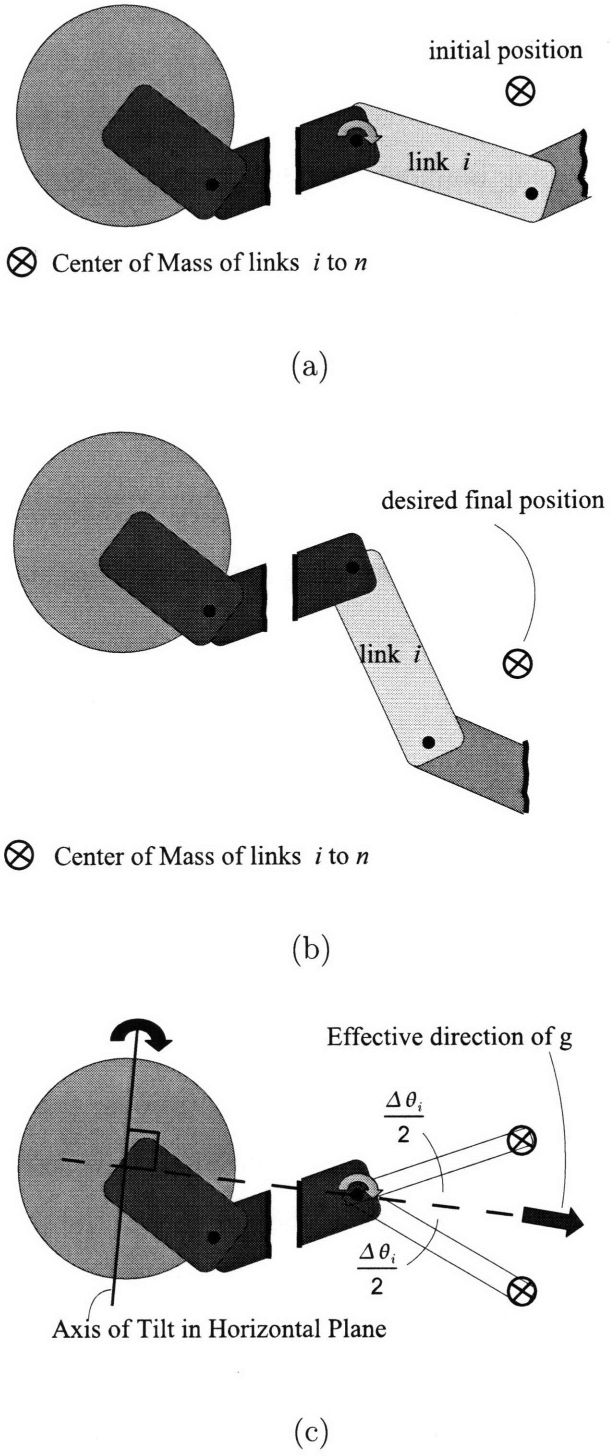

Figure 4-6: Single link deployment: (a) initial position, (b) desired final position, (c) choice of tilt axis

4.2 Concurrent Multi-link Deployment

We consider the case where two unactuated links of the hyper-articulated arm are in motion concurrently. Our goal is to concurrently steer 2 links from their respective initial locations (starting at 0 velocity) to desired final locations with zero final velocity. The corresponding boundary conditions may be written as ($i = 2, 3$)

$$\theta_i(0) = \theta_{i0},\ \theta_i(t_f) = \theta_{if} \text{ and } \dot{\theta}_i(0) = 0,\ \dot{\theta}_i(t_f) = 0. \tag{4.15}$$

(3.22) and (4.15) represent a system of 4^{th} order ODEs with 8 boundary conditions. This problem may be formulated as a boundary value problem if the control input ϕ is parameterized in terms of 4 parameters. These parameters p_j ($1 \leq j \leq 4$) are constant but unknown and the system (3.22) and (4.15) may be augmented with the system

$$\dot{p}_j = 0. \tag{4.16}$$

We propose an algorithm for formalizing this approach.

4.2.1 Control Algorithms

We parameterize the tilt of link 1 along two fixed orthogonal axes, X_0^* and Y_0^* in the horizontal plane. Let us denote the angular rotations by ϕ_X and ϕ_Y respectively. See Fig. 4-7. The trajectories ϕ_X and ϕ_Y comprise three sigmoidal segments each. The parameters correspond to the peaks and troughs of the sigmoidal segments and are denote by ϕ_{Xa}, ϕ_{Xb}, ϕ_{Ya} and ϕ_{Yb}. For finite angular rotations, the sequence of rotations determines the final orientation of a rigid body. However, if $|\phi_X|$ and $|\phi_Y|$ are small, the rotations commute up to first order. We verify *a posteriori*, that this small angle assumption is indeed true.

The orientation γ of the equivalent axis of tilt and the amplitude of tilt are give

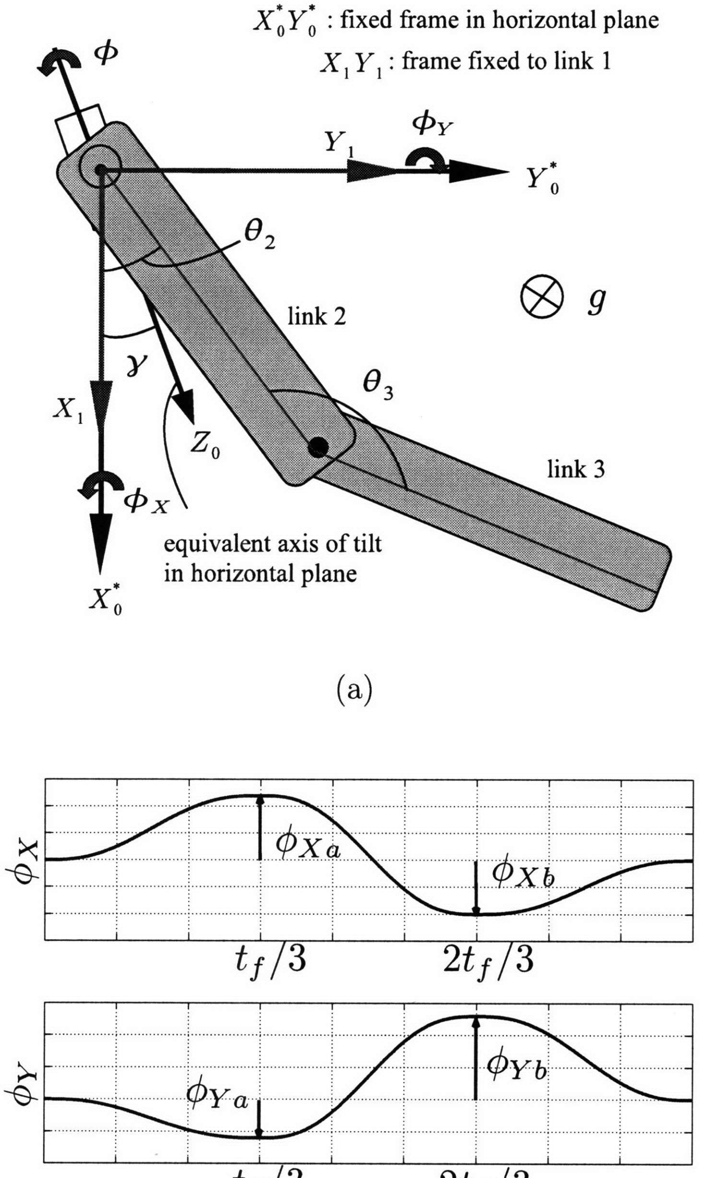

(a)

(b)

Figure 4-7: Tilt scheme for concurrent multi-link deployment by

$$\gamma = \text{atan2}(\phi_Y, \phi_X) \tag{4.17}$$

$$\phi = \sqrt{\phi_X^2 + \phi_Y^2} \tag{4.18}$$

The duration of each sigmoidal segment was fixed at $\frac{t_f}{3}$. As a result, the orientation γ of the axis of tilt remains fixed during each subinterval $(0, \frac{t_f}{3})$, $(\frac{t_f}{3}, \frac{2t_f}{3})$ and $(\frac{2t_f}{3}, t_f)$. These fixed orientations are given by $\gamma_a = \text{atan2}(\phi_{Ya}, \phi_{Xa})$, $\gamma_b = \text{atan2}(\phi_{Yb} - \phi_{Ya}, \phi_{Xb} - \phi_{Xa})$ and $\gamma_a = \text{atan2}(-\phi_{Yb}, -\phi_{Xb})$.

4.2.2 Simulation Results

Fig. 4-8 shows the simulation results for the boundary conditions

$$\theta_2(0) = 0^\circ,\ \theta_2(t_f) = 60^\circ \text{ and } \theta_3(0) = 80^\circ,\ \theta_3(t_f) = 25^\circ.$$
$$\dot\theta_2(0) = 0,\ \dot\theta_2(t_f) = 0 \text{ and } \dot\theta_3(0) = 0,\ \dot\theta_3(t_f) = 0.$$

These boundary conditions correspond to *in-phase* motion of links 2 and 3 (both clockwise). The final time was set at $t_f = 8s$. Fig. 4-8(a) shows the X and Y components of the trajectories of the link 1. The parameters of the sigmoid trajectories obtained from the solution of the boundary value problem are

$$\phi_{Xa} = -0.05^\circ, \phi_{Xb} = -0.20^\circ, \phi_{Ya} = -0.35^\circ, \phi_{Yb} = 0.44^\circ.$$

Fig. 4-9 shows the simulation results for the boundary conditions

$$\theta_2(0) = 0^\circ,\ \theta_2(t_f) = 80^\circ \text{ and } \theta_3(0) = 0^\circ,\ \theta_3(t_f) = 90^\circ.$$
$$\dot\theta_2(0) = 0,\ \dot\theta_2(t_f) = 0 \text{ and } \dot\theta_3(0) = 0,\ \dot\theta_3(t_f) = 0.$$

These boundary conditions correspond to *out-of-phase* motion of links 2 and 3 (link 2 counter-clockwise, link 3 clockwise). The final time was set at $t_f = 8s$. Fig. 4-9(a)

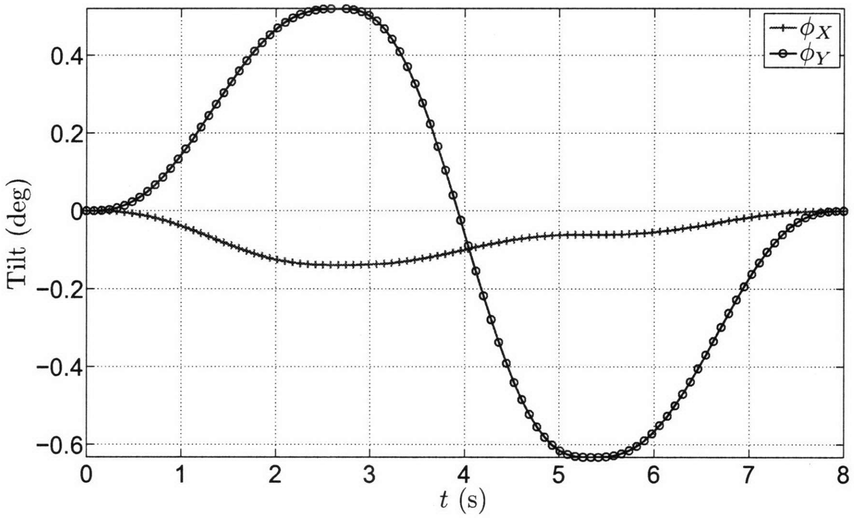

(a)

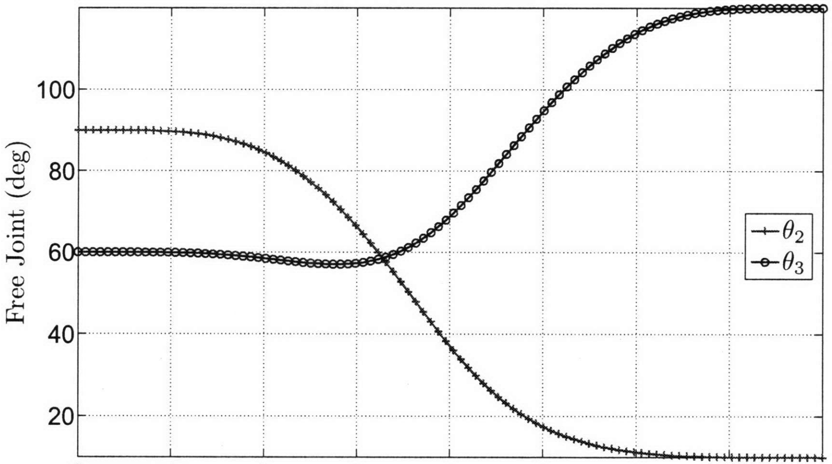

(b)

Figure 4-8: In-phase motion: (a) Tilting table trajectories (ϕ_X and ϕ_Y); (b) Free joint trajectories shows the X and Y components of the trajectories of the link 1. The parameters of the sigmoid trajectories obtained from the solution of the boundary value problem are

$$\phi_{Xa} = -0.39^\circ, \phi_{Xb} = 0.38^\circ, \phi_{Ya} = -0.38^\circ, \phi_{Yb} = 0.32^\circ.$$

In both cases the amplitudes of tilt are small. This verifies, *a posteriori*, the small angle assumption ensuring commutativity of rotations.

Remark 4.2.1. *The concurrent multi-link deployment problem also admits an optimal control formulation. The associated boundary value problem is of order 12. However, as seen in the single link case, the solution obtained from the optimal control formulation is almost identical to the parameterized control formulation. Thus the solution of a higher order boundary value problem is unwarranted.*

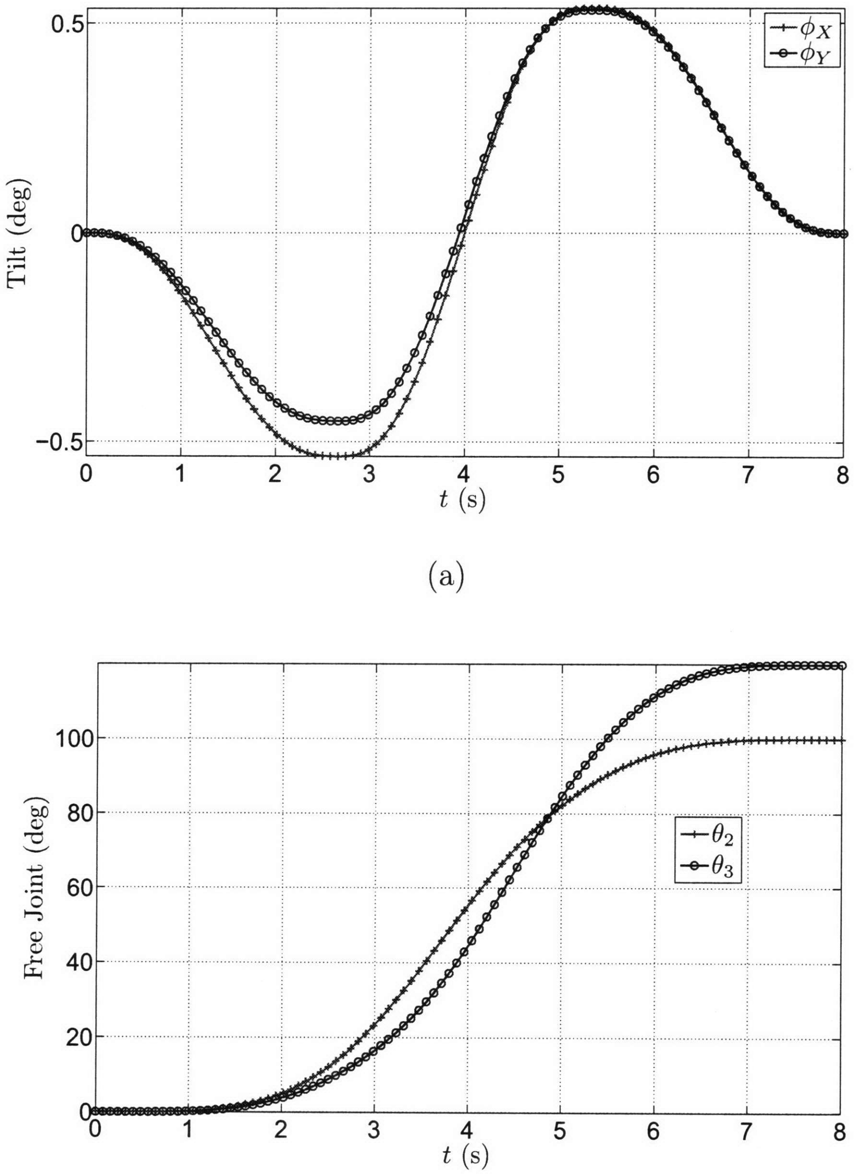

(a)

(b)

Figure 4-9: Out-of-Phase motion: (a) Tilting table trajectories (ϕ_X and ϕ_Y); (b) Free joint trajectories

Chapter 5

Feedback Control

We have proposed several motion planning algorithms suitable for the gravity-assisted underactuated robot arm. They include parameterized trajectory planning for the actuated joint and feed-forward optimal control. These are *open-loop* techniques and work well in the absence of disturbances. Also, an exact knowledge of the system dynamics is needed. In particular, a good estimate of stiction characteristics as well as dynamics associated with assorted cables and hoses is necessary for accurate position control of the robot arm. However, it is unrealistic to assume prior knowledge of such state dependent unknown parameters. This necessitates the development of a *closed-loop* control strategy for our system.

We first propose a feedback control law for sequential link deployment; in this case, only one unactuated link is in motion at any given time. We synthesize a Lyapunov function to prove the convergence of our control law. The Lyapunov function is also used to generate estimates of the domain of convergence for this law. Next, we discuss concurrent multi-link deployment. It is not immediately clear as to how feedback control schemes can be generated to control multiple links using a single input. Instead, we propose an intermittent feedback scheme, where the feed-forward motion plan is smoothly updated based on periodic measurements of the output.

5.1 Feedback Law for Sequential Link Deployment

In this section, we propose a closed loop control law for point-to-point control of the unactuated link. The goal is to transfer the unactuated link from an initial angular position θ_0 ($= \theta_{20}+\alpha$) with zero initial velocity to a final angular position θ_f ($= \theta_{2f}+\alpha$) with zero final velocity. We treat the actuated coordinate ϕ as a *pseudo input* and prescribe a feedback law in terms of the *pseudo input.* The formal justification of this treatment is deferred to Appendix D.

From (3.9), we see that the input ϕ has a bounded effect on the acceleration because $|\sin\phi| \leq 1$. We propose a feedback control law of the form:

$$\sin\phi = \frac{\sin(k_1(\theta_f - \theta) - \bar{k}_2\dot{\theta})\sin\theta}{k}, \tag{5.1}$$

where $k \geq 1$ and $k_1, \bar{k}_2 > 0$ are constants. Also θ_f is the desired final angular position of the unactuated link. We note that ϕ exists because $|\sin(k_1(\theta_f - \theta) - k_2\dot{\theta})\sin\theta/k| \leq 1$. Using (5.1) in (3.9) we get:

$$\ddot{\theta} = \frac{A}{k}\sin(k_1(\theta_f - \theta) - \bar{k}_2\dot{\theta})\sin^2\theta. \tag{5.2}$$

Let us introduce a non-dimensional time scale $\tau \triangleq \omega_n t$, where $\omega_n \triangleq \sqrt{A/k}$. We can now rewrite (5.2) as:

$$\ddot{\theta} = \sin(k_1(\theta_f - \theta) - k_2\dot{\theta})\sin^2\theta. \tag{5.3}$$

Here $k_2 = \omega_n\bar{k}_2$ and it is understood that the derivatives denote differentiation with respect to τ.

5.1.1 Physical Interpretation

The intuition behind the control law (5.1) is to introduce a virtual non-linear spring and damper into the system. These virtual elements introduce a stable equilibrium point $[\theta, \dot{\theta}] = [\theta_f, 0]$ in the system dynamics. In the vicinity of the equilibrium point

$[\theta_f, 0]$, the dynamics (5.3) may be approximated as:

$$\ddot{\theta} \approx (k_1 \sin^2 \theta_f)(\theta_f - \theta) - (k_2 \sin^2 \theta_f)\dot{\theta}. \tag{5.4}$$

The parameters k_1 and k_2 are measures of stiffness and damping respectively. Further, the multiplicative term $\sin\theta$ in (5.1) ensures that the *sign* of the acceleration $\ddot{\theta}$ in (5.3) is not affected by the regime of motion ($\sin\theta > 0$ or $\sin\theta < 0$). It is only affected by the deviation from the desired final state $[\theta, \dot{\theta}] = [\theta_f, 0]$.

The linearized system (5.4) does not provide any insight about the domain of convergence of the control law for different choices of k_1 and k_2. Also, the linearization of (5.3) about the other equilibrium point $[0, 0]$ is degenerate and the stability of the non-linear system cannot be inferred. These issues are formally addressed in the non-linear convergence analysis below.

5.1.2 Proof of Convergence

Let us consider the domain $\Omega = \{[\theta, \dot{\theta}] : |k_1(\theta_f - \theta) - k_2\dot{\theta}| \leq \pi/2 \text{ and } |\theta| < \pi\}$, and a Lyapunov function candidate (defined on Ω):

$$V(\theta, \dot{\theta}) = \frac{1}{k_1} \int_0^{\psi} \sin x \sin^2(\frac{x + k_2\dot{\theta}}{k_1} - \theta_f) dx + \frac{1}{2}\dot{\theta}^2, \tag{5.5}$$

where $\psi = k_1(\theta_f - \theta) - k_2\dot{\theta}$.

Proposition. *The control law (5.1) guarantees local asymptotic convergence of the state* $[\theta, \dot{\theta}]$ *in (5.3) to* $[\theta_f, 0]$ *for arbitrary gains* $k_1, k_2 > 0$. *Further,* $\exists\ l(k_1, k_2) > 0$ *for which an estimate of the domain of attraction of the control law is the bounded region* $\Omega_l = \{[\theta, \dot{\theta}] : V(\theta, \dot{\theta}) < l\} \subset \Omega$.

Proof. The scalar function $V(\theta, \dot{\theta})$ defined in (5.5) is positive definite in Ω because it satisfies the following conditions:

1. $V(\theta_f, 0) = 0$.

2. $V(\theta, \dot{\theta}) > 0$ in Ω $\forall$ $[\theta, \dot{\theta}] \neq [\theta_f, 0]$.

The 1^{st} condition follows from direct substitution in (5.5) and noting that $[\theta, \dot{\theta}] = [\theta_f, 0]$ implies $\psi = 0$. The 2^{nd} condition follows by noting that $\sin x > 0$ for $\pi/2 \geq x > 0$ and $\sin x < 0$ for $-\pi/2 \leq x < 0$. Thus, for $0 < |\psi| \leq \pi/2$:

$$\int_0^{\psi} \sin x \sin^2\left(\frac{x + k_2\dot{\theta}}{k_1} - \theta_f\right) dx > 0. \tag{5.6}$$

Henceforth, we abbreviate $V(\theta, \dot{\theta})$ as V. It is convenient to rewrite (5.5) as:

$$V = \begin{cases} \frac{k_1(\cos\psi - \cos\frac{2\psi}{k_1})\cos 2\theta + (k_1 \sin\frac{2\psi}{k_1} - 2\sin\psi)\sin 2\theta}{2(k_1^2 - 4)} + \frac{1}{2k_1}(1 - \cos\psi) + \frac{1}{2}\dot{\theta}^2, & k_1 \neq 2. \\ \frac{1}{8}(\sin\psi \sin 2\theta - \psi \sin(\psi + 2\theta) + 4\sin^2\frac{\psi}{2}) + \frac{1}{2}\dot{\theta}^2, & k_1 = 2. \end{cases} \tag{5.7}$$

Appendix E shows a construction of l such that the region Ω_l is a subset of Ω. The time derivative of (5.7) along system trajectories is given by:

$$\dot{V} = \frac{\partial V}{\partial \theta}\dot{\theta} + \frac{\partial V}{\partial \dot{\theta}}\ddot{\theta}$$

$$= \begin{cases} -\frac{k_2 \sin^2\theta}{k_1(4 - k_1^2)}(k_1 \sin\psi(\sin 2\theta \cos\psi - \sin 2(\frac{\psi}{k_1} + \theta)) + (2 - k_1^2 \sin^2\theta)\sin^2\psi), & k_1 \neq 2. \\ -\frac{k_2 \sin^2\theta}{8}((1 + 2\sin^2\theta)\sin^2\psi - \psi \sin\psi \cos(2\theta + \psi)), & k_1 = 2. \end{cases} \tag{5.8}$$

It may be shown that $\dot{V} \leq 0$ in Ω for all $k_1, k_2 > 0$. In the interest of brevity, we just prove this assertion for $k_1 = 1$ and $k_2 > 0$. We defer the proof of the general case to Appendix A. Substituting $k_1 = k_2 = 1$ in (5.8) and after some rearrangement we get:

$$\begin{aligned} \dot{V} = &-\frac{B^2}{3}\sin^2\theta(1 - \cos\psi)[3\sin^2\theta\cos\psi(1 - \cos\psi) + (2\sin\theta\cos\psi + \sin\psi\cos\theta)^2 \\ &+ (\sin\psi\cos\theta + \sin\theta)^2 + \sin^2\theta\cos^2\psi] \end{aligned} \tag{5.9}$$

We note the $0 \leq \cos\psi \leq 1$ in Ω. Thus, the expression in square brackets in (5.9) is always non-negative. Hence, $\dot{V} \leq 0$ in Ω. Also, from (5.9):

$$\begin{aligned} &\dot{V} = 0 \\ \Rightarrow\ &\dot{\theta} = 0 \text{ or } \psi = 0 \end{aligned} \tag{5.10}$$

Using (5.12) in (5.2) we get:

$$\dot{V} = 0 \Rightarrow\ \ddot{\theta} = 0 \tag{5.11}$$

Since $\dot{V}$ is only *negative semi-definite*, we next analyze the invariant sets where $\dot{V} = 0$. From (C.5):

$$\dot{V} = 0 \Rightarrow\ \dot{\theta} = 0 \text{ or } \psi = 0 \tag{5.12}$$

Using (5.12) in (5.2) we get:

$$\dot{V} = 0 \Rightarrow\ \ddot{\theta} = 0 \tag{5.13}$$

From (5.12) and (5.13), the largest invariant set where $\dot{V} = 0$ is given by $\{[\theta, \dot{\theta}] = [0, 0] \cup [\theta_f, 0]\}$. Using *La Salle's invariant set theorem*, we conclude that the state $[\theta, \dot{\theta}]$ converges to $[\theta = 0, \dot{\theta} = 0]$ or $[\theta = \theta_f, \dot{\theta} = 0]$.

It remains to establish the stability of the equilibrium points. If $\theta_f = 0$, the largest invariant set is $\{[\theta, \dot{\theta}] = [0, 0]\}$. Thus, $[\theta_f, 0]$ is a stable equilibrium point. If $\theta_f \neq 0$, we show that $[\theta = 0, \dot{\theta} = 0]$ is unstable and $[\theta = \theta_f, \dot{\theta} = 0]$ is a stable equilibrium point. From (5.7):

$$\left.\frac{\partial^2 V}{\partial \theta^2}\right|_{0,0} = 0 \text{ and } \left.\frac{\partial^3 V}{\partial \theta^3}\right|_{0,0} = -2\sin(k_1\theta_f) \neq 0.$$

This implies that $[\theta = 0, \dot{\theta} = 0]$ is not a local minimum for V and thus an *unstable*

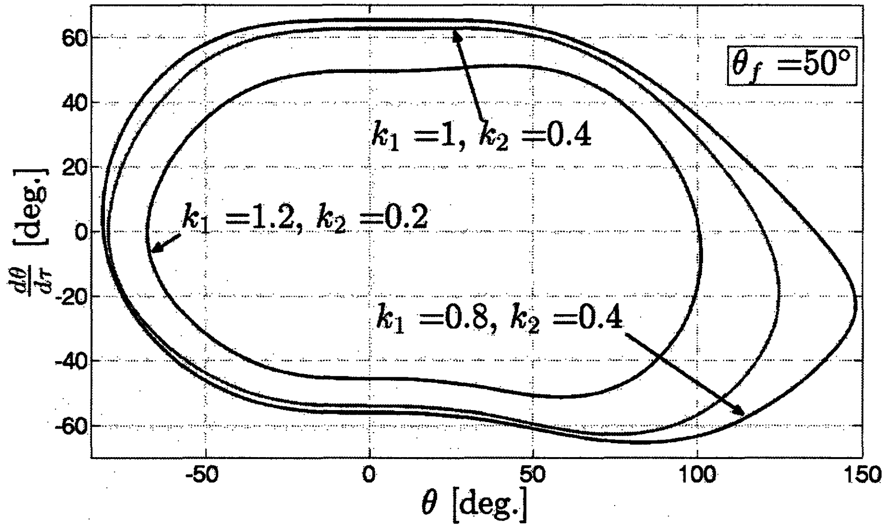

Figure 5-1: Estimates of domain of convergence for various gains

equilibrium point. Once again, from (5.7):

$$\nabla^2 V\Big|_{\theta_f,0} = \begin{bmatrix} k_1\sin^2\theta_f & k_2\sin^2\theta_f \\ k_2\sin^2\theta_f & \frac{k_2^2}{k_1}\sin^2\theta_f+1 \end{bmatrix}.$$

This implies that $\nabla^2 V$ is positive definite and $[\theta = \theta_f, \dot{\theta} = 0]$ is a local minimum for V and thus a *stable* equilibrium point. Thus the state $[\theta, \dot{\theta}]$ in (5.2) converges to $[\theta_f, 0]$ as long as it does not start from $[0, 0]$. $\square$

Remark 5.1.1. *Fig. 5-1 shows a comparison of the estimates of the domain of convergence for various choices of* k_1 *and* k_2. *The desired final position was* $\theta_f = 50°$ *in each case.*

Remark 5.1.2. *The Hamiltonian of the undamped system (setting* $k_2 = 0$ *in (5.3)) may also serve as a Lyapunov function candidate. This Hamiltonian is given by* $H = \frac{1}{k_1}\int_0^{k_1(\theta_f-\theta)} \sin x \sin^2(\frac{x}{k_1} - \theta_f)dx + \frac{1}{2}\dot{\theta}^2$. *However, the domain of convergence is smaller than that obtained from the Lyapunov function (5.5). This is shown in Fig. 5-2.*

Remark 5.1.3. *It may be noted that the instability of the equilibrium point* $[\theta = 0, \dot{\theta} = 0]$ *does not follow from linearization because the linearized system has zero eigenvalues*

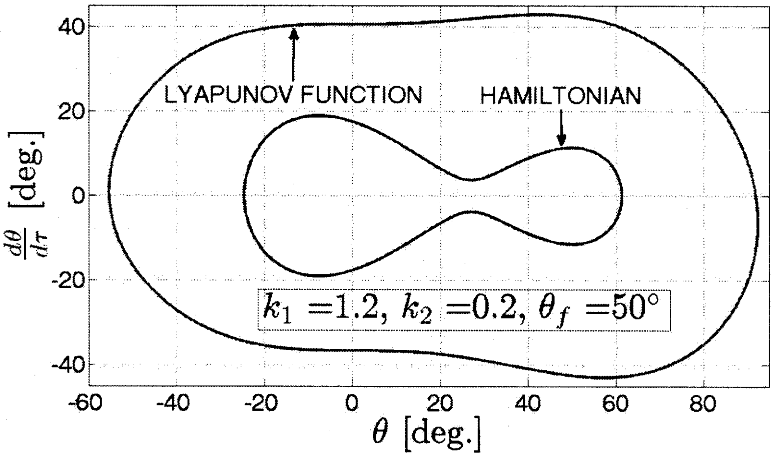

Figure 5-2: Comparison of estimates of domain of convergence: lyapunov function and hamiltonian

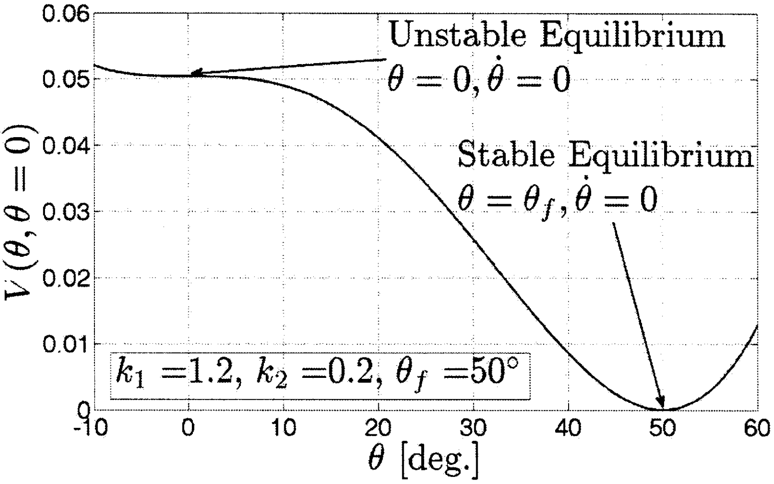

Figure 5-3: Stable and unstable equilibria of system dynamics

at that point. Fig. 5-3 shows the variation of the Lyapunov function as a function of θ *on the plane* $\dot{\theta} = 0$. *The parameter values were* $k_1 = 1.2$, $k_2 = 0.2$ *and* $\theta_f = 50°$. *The equilibrium* $[\theta = 0, \dot{\theta} = 0]$ *is unstable, while the destination* $[\theta = \theta_f, \dot{\theta} = 0]$ *is stable.*

5.1.3 Simulation Results

Fig. 5-4 shows the simulation results for various control gains. The parameters in (3.10) and (3.11) are set at $A = 32.8$ and $\alpha = -3.22°$ for the simulations. These correspond to our experimental setup presented in Chapter 6. We also introduced some viscous friction in simulations. The tilt trajectory (ϕ) of link 1 is shown in Fig. 5-4(a) for various choices of the control gains. A small amplitude of ϕ is very important in practice because the arm operates inside an aircraft wing. If link 2 starts at θ_0 with zero initial velocity, the initial tilt of link 1 is given by:

$$\sin\phi_0 = \frac{\sin(k_1(\theta_f - \theta_0))\sin\theta_0}{k} \tag{5.14}$$

The maximum tilt is 1.3° for the case $k = 12$ and $k_1 = 1.2$. This is acceptable for operation inside the wing-box.

The trajectory (θ_2) of the free link is shown in Fig. 5-4b for various control gains. From (5.4), the quantity $k_2/\sqrt{k_1}$ ($= \bar{k}_2/\sqrt{k k_1}$) may be interpreted as a measure of "damping ratio" for the closed loop dynamics. As expected, less overshoot is observed as the "damping ratio" is increased. A lower "damping ratio" also results in a faster rise time. However, the corresponding settling time is also larger because of oscillations. These observations are evident in Fig. 5-4(b).

5.1.4 Extension of Control Law

A primary drawback of the proposed control law arises from the conflicting requirements of small amplitude of tilt of link 1 and small steady state error for link 2. This is readily seen from (5.14). The initial tilt ϕ_0 may be large if the amplitude of motion $|\theta_f - \theta_0|$ is large. To achieve smaller values of ϕ_0, the scaling factor k may be increased or the gain k_1 may be reduced. As noted before, the ratio k_1/k is a measure of the stiffness of the virtual non-liner spring introduced by the controller. Increasing k and reducing k_1 would result in lower stiffness. This would lower the speed of convergence and also increase the steady state error induced by Coulomb friction.

We address this issue by replacing the fixed reference θ_f in (5.1) by a time varying reference $\theta_{ref}(t)$ starting at θ_0 and changing smoothly to θ_f. In particular, the

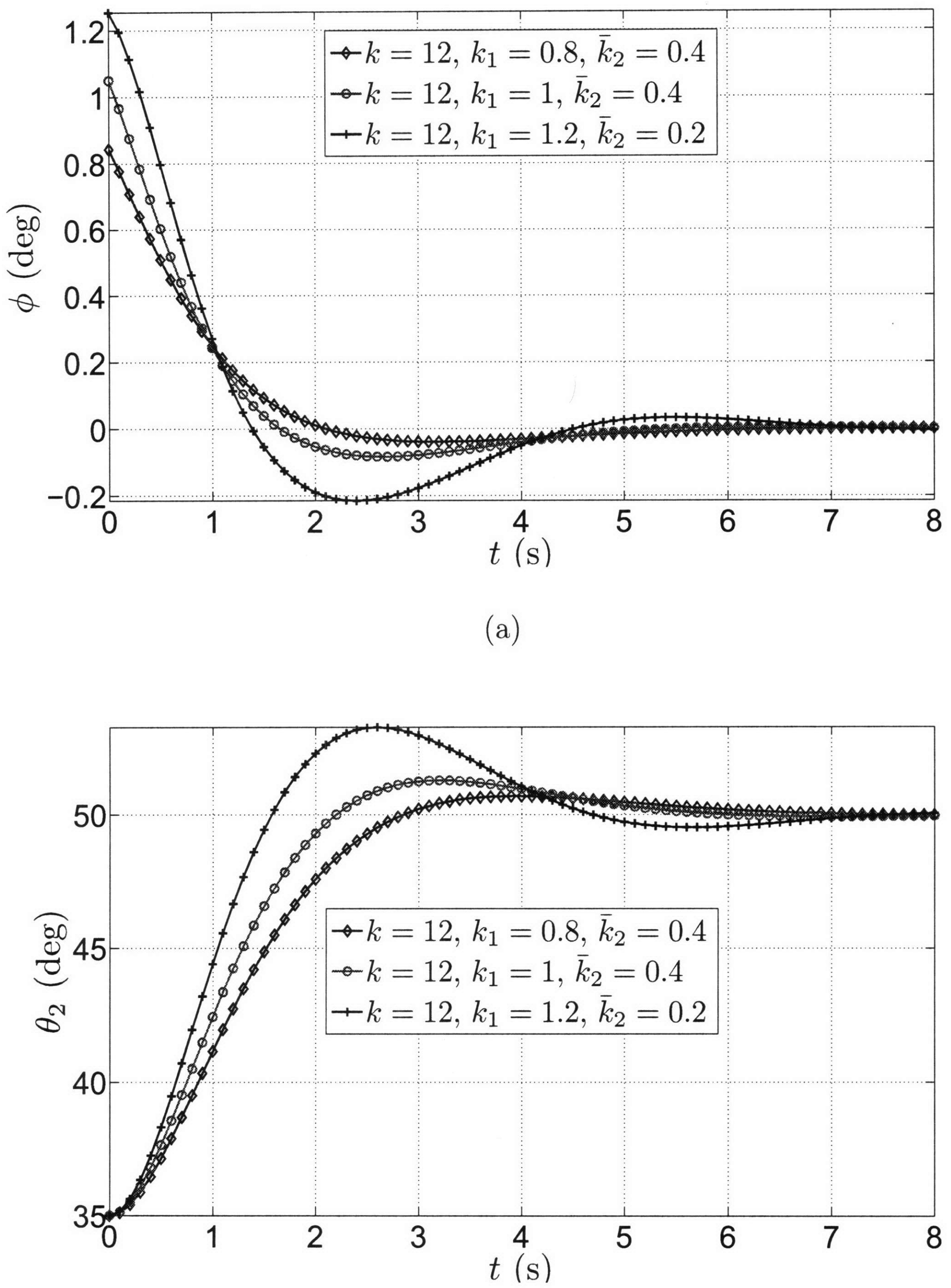

(a)

(b)

Figure 5-4: Feedback control: (a) actuated joint trajectory; (b) Unactuated joint trajectory reference may be a sigmoidal trajectory given by:

$$\theta_{ref}(t) = \begin{cases} \theta_0 + \left(10(\frac{t}{t_{f1}})^3 - 15(\frac{t}{t_{f1}})^4 + 6(\frac{t}{t_{f1}})^5\right)(\theta_f - \theta_0) & 0 \leq t \leq t_{f1} \\ \theta_f & t \geq t_{f1} \end{cases} \tag{5.15}$$

We may choose t_{f1} to set a desired average speed of motion $|\theta_f - \theta_0|/t_{f1}$. Substituting (5.15) in (5.1), we obtain the modified control law:

$$\sin\phi = \frac{\sin(k_1(\theta_{ref}(t) - \theta) + k_2(\dot{\theta}_{ref}(t) - \dot{\theta}))\sin\theta}{k}. \tag{5.16}$$

Fig. 5-5 shows the simulation results using the modified control law (5.16). The parameter t_{f1} was set at $10s$. The trajectory of the unactuated joint is shown in Fig. 5-5(a). Fig. 5-5(b) shows the corresponding actuated joint trajectories for various gains. The maximum amplitude of tilt is 0.4°. This is well within acceptable limits. The Fig. 5-5(c) shows the actuated joint trajectories, when a fixed reference θ_f is used. The maximum amplitude of tilt is 10°, which is too large for operation inside an aircraft wing.

Remark 5.1.4. *The convergence proof presented for the autonomous case does not carry over for the time varying control law. However, as seen from (5.15), the system is autonomous for* $t \geq t_{f1}$. *From (5.2), we see that the magnitude of the acceleration* $|\ddot{\theta}|$ *is upper bounded by* A. *Thus, the position and velocity of the system at time* t_{f1} *are also bounded. Some conservative estimates of these bounds are* $|\theta(t_{f1})| < |\theta(0)| + \frac{A}{k}|\dot{\theta}(0)|t_{f1} + \frac{A}{2k}t_{f1}^2$ *and* $|\dot{\theta}(t_{f1})| < |\dot{\theta}(0)| + \frac{A}{k}t_{f1}$. *If the state* $[\theta, \dot{\theta}]$ *at time* t_{f1} *is within the domain of attraction for the autonomous control law, the system is guaranteed to converge to* $[\theta_f, 0]$. *However, these bounds are too conservative to be practically useful.*

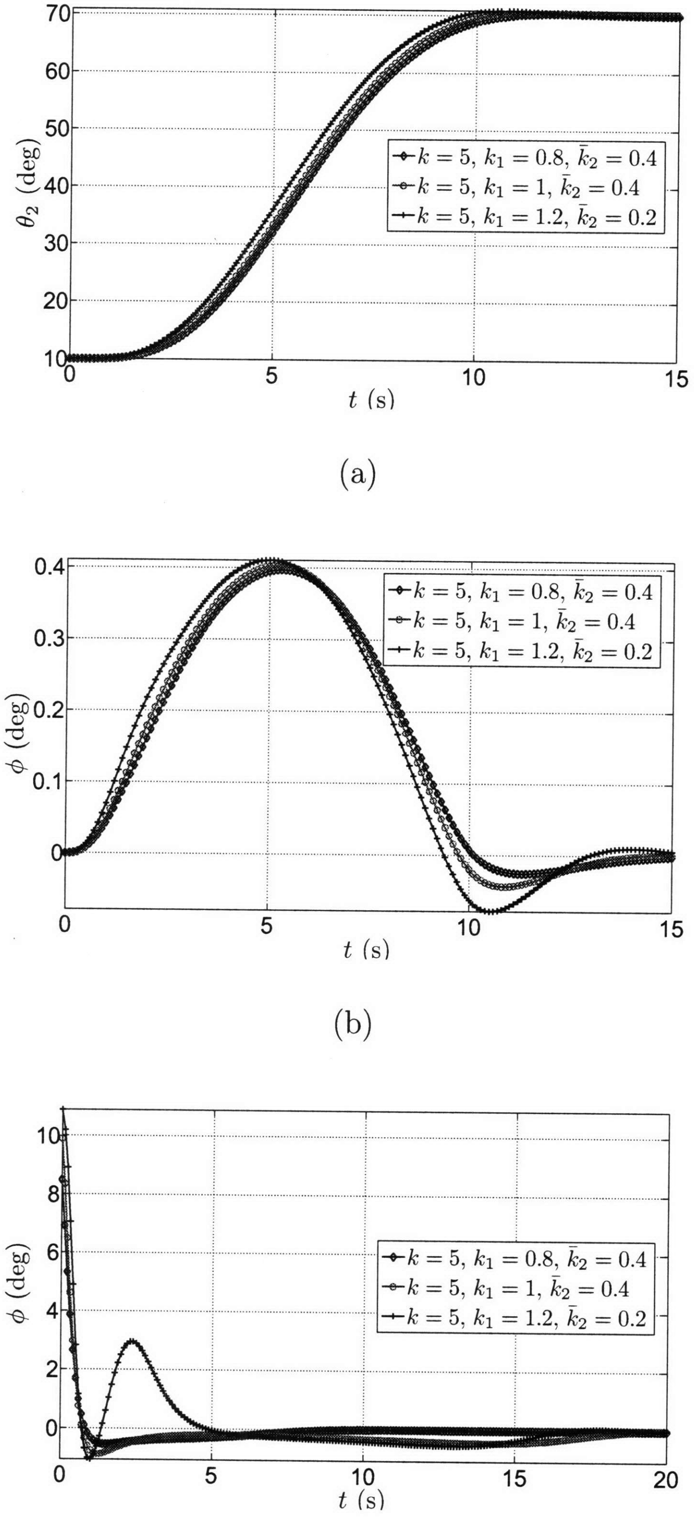

(c)

Figure 5-5: Feedback control with sigmoidal reference input: (a) Unactuated joint trajectory; (b) Actuated joint trajectory; (c) Actuated joint trajectory with fixed reference input

5.2 Intermittent Feedback for Concurrent Multi-link Deployment

The feedback control scheme for sequential link deployment cannot be readily extended to concurrent multi-link deployment. It is not immediately clear as to how error signals from multiple free joints may be used to generate a single feedback input for the actuated joint. Instead, we present a scheme whereby the planned input trajectory may be periodically modified based on actual measurements of the positions and velocities of the free links.

5.2.1 Control Algorithm

The key idea is to update the pre-computed motion plan based on measurements of the actual system states. Fig. 5-6 shows a block diagram of the intermittent feedback control scheme. The "Actual System" block corresponds to the true physical system, while the "Dynamic Model" corresponds to our approximate model (3.22). The switches S_1 and S_2 are closed at $t = 0$ and then again at $t = t_c$, when the actual outputs $[\dot{\theta}_2(t_c), \dot{\theta}_3(t_c), \theta_2(t_c), \theta_3(t_c)]$ are checked against the model-based outputs $[\dot{\overline{\theta}}_2(t_c), \dot{\overline{\theta}}_3(t_c), \overline{\theta}_2(t_c), \overline{\theta}_3(t_c)]$.

At $t = 0$, we start with pre-computed sigmoidal input trajectories along two orthogonal axes in the horizontal plane, given by $\overline{\phi}_X(t)$ (parameters $\overline{\phi}_{Xa}$ and $\overline{\phi}_{Xb}$) and $\overline{\phi}_Y(t)$ (parameters $\overline{\phi}_{Ya}$ and $\overline{\phi}_{Yb}$). At $t = t_c$, if the actual output differs significantly from the model-based output, we recompute the input trajectory parameters. The "Input Parameter Generator" generates the updated parameters $[\phi_{Xa}, \phi_{Xb}, \phi_{Ya}, \phi_{Yb}]$, as well as the additional time frame Δt_f for which the motion is executed. These parameters are generated from the solution of the associated boundary value problem with the actual outputs as updated initial conditions. The parameter Δt_f is determined from considerations on maximum allowable acceleration of the tilt trajectory. The updated input trajectories at $t = t_c$ are patched smoothly with the pre-computed ones.

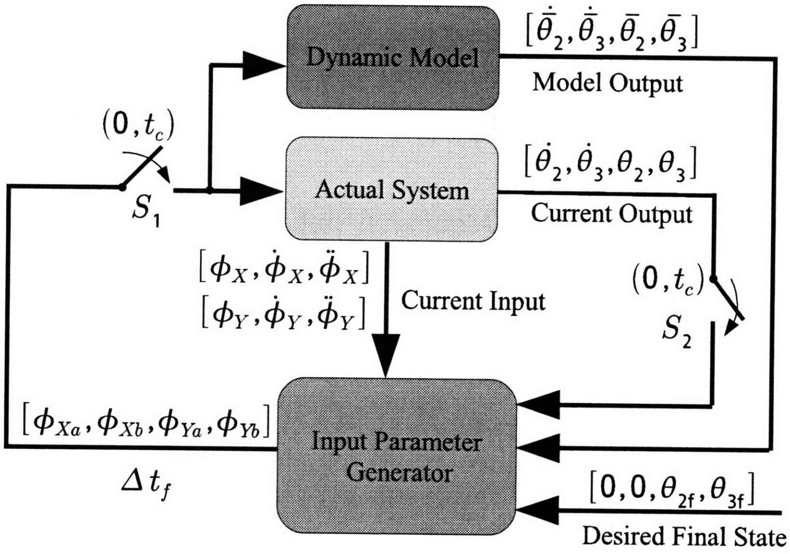

Figure 5-6: Block diagram for intermittent feedback control

Fig. 5-7 shows the pre-computed and updated sigmoidal trajectory segments. Let us denote the position, velocity and acceleration of the pre-computed sigmoidal trajectory at time t_c by ϕ_c, ω_c and α_c respectively. The updated sigmoidal trajectory must match these initial conditions for a smooth transition. Also, let us denote the final position, velocity and acceleration by ϕ_f, ω_f and α_f respectively. A sigmoid with these boundary conditions is given by:

$$\phi(t) = \sum_{i=0}^{5} a_i \left(\frac{t}{\Delta t}\right)^i \qquad 0 \le t \le \Delta t \tag{5.17}$$

where

$$a_5 = 6(\phi_f - \phi_c) - 3(\omega_f + \omega_c)\Delta t + \frac{1}{2}(\alpha_f - \alpha_c)(\Delta t)^2 \tag{5.18}$$

$$a_4 = -15(\phi_f - \phi_c) + (7\omega_f + 8\omega_c)\Delta t - \frac{1}{2}(2\alpha_f - 3\alpha_c)(\Delta t)^2 \tag{5.19}$$

$$a_3 = 10(\phi_f - \phi_c) - (4\omega_f + 6\omega_c)\Delta t + \frac{1}{2}(\alpha_f - 3\alpha_c)(\Delta t)^2 \tag{5.20}$$

$$a_2 = \frac{1}{2}\alpha_c(\Delta t)^2 \tag{5.21}$$

$$a_1 = \omega_c \Delta t \tag{5.22}$$

$$a_0 = \phi_c \tag{5.23}$$

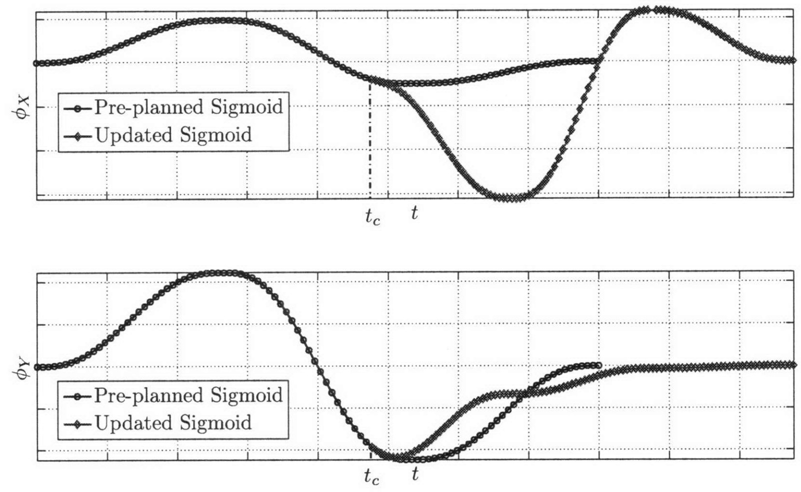

Figure 5-7: Pre-planned and updated sigmoid trajectories

5.2.2 Simulation Results

Fig. 5-8 shows the simulation results for the boundary conditions

$$\theta_2(0) = 0^\circ,\ \theta_2(t_f) = 100^\circ \text{ and } \theta_3(0) = 0^\circ,\ \theta_3(t_f) = 120^\circ.$$

$$\dot{\theta}_2(0) = 0,\ \dot{\theta}_2(t_f) = 0 \text{ and } \theta_3(0) = 0,\ \dot{\theta}_3(t_f) = 0.$$

The pre-computed motion plan was over a duration $t_f = 8s$. At time $t_c = 4.77s$, the output (position and velocity of the unactuated links) was "measured". The discrepancies ($\Delta\theta_2(t_c) = 10^\circ$, $\Delta\theta_3(t_c) = -30^\circ$) in the actual and pre-computed outputs are shown in Fig. 5-8(b). The boundary value problem was solved with the updated initial conditions and the updated sigmoidal trajectory was smoothly patched (using (5.17)) with the pre-computed sigmoidal trajectory. The final time was extended by $\Delta t_f = 6s$. The pre-computed and updated sigmoidal trajectories are shown in Fig. 5-8(a). Using the updated sigmoidal input, the output satisfies the desired boundary conditions at the final time $t_c + \Delta t_f$. This is shown in Fig. 5-8(b).

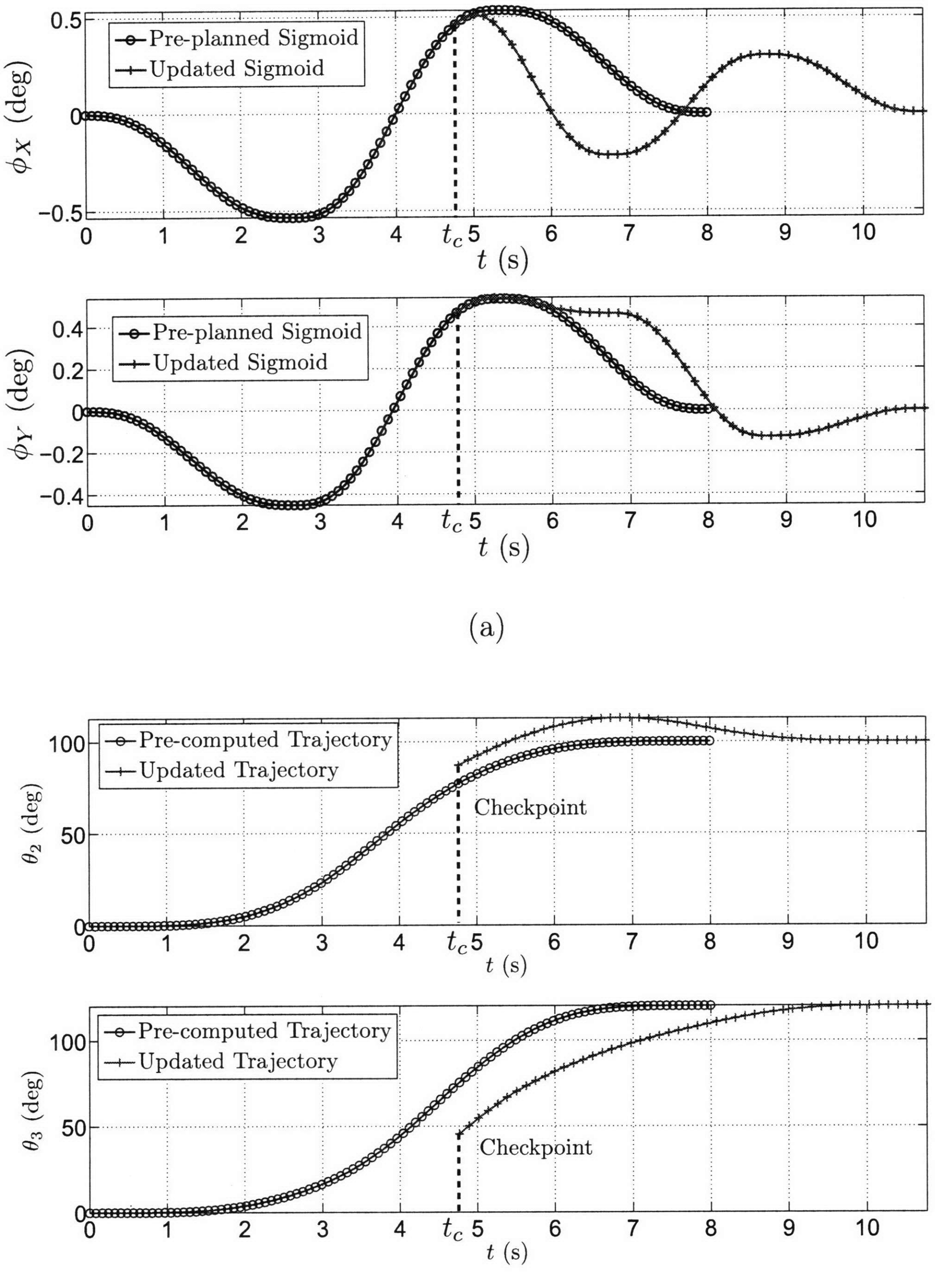

(a)

(b)

Figure 5-8: (a) Tilt trajectories; (b) Unactuated link trajectory

Fig. 5-9 shows the simulation results for the boundary conditions

$$\theta_2(0) = 90^\circ,\ \theta_2(t_f) = 10^\circ \text{ and } \theta_3(0) = 60^\circ,\ \theta_3(t_f) = 120^\circ.$$

$$\dot{\theta}_2(0) = 0,\ \dot{\theta}_2(t_f) = 0 \text{ and } \theta_3(0) = 0,\ \dot{\theta}_3(t_f) = 0.$$

The pre-computed motion plan was over a duration $t_f = 8s$. At time $t_c = 4.77s$, the output (position and velocity of the unactuated links) was measured. The discrepancy in the pre-computed and actual output is shown in Fig. 5-9(b). The boundary value problem was solved with the updated initial conditions and the updated sigmoidal trajectory was smoothly patched with the pre-computed trajectory. The final time was extended by $\Delta t_f = 6s$. The pre-computed and updated sigmoidal trajectories are shown in Fig. 5-9(a). Using the updated sigmoidal input, the output satisfies the desired boundary conditions at the final time $t_c + \Delta t_f$. This is shown in Fig. 5-9(b).

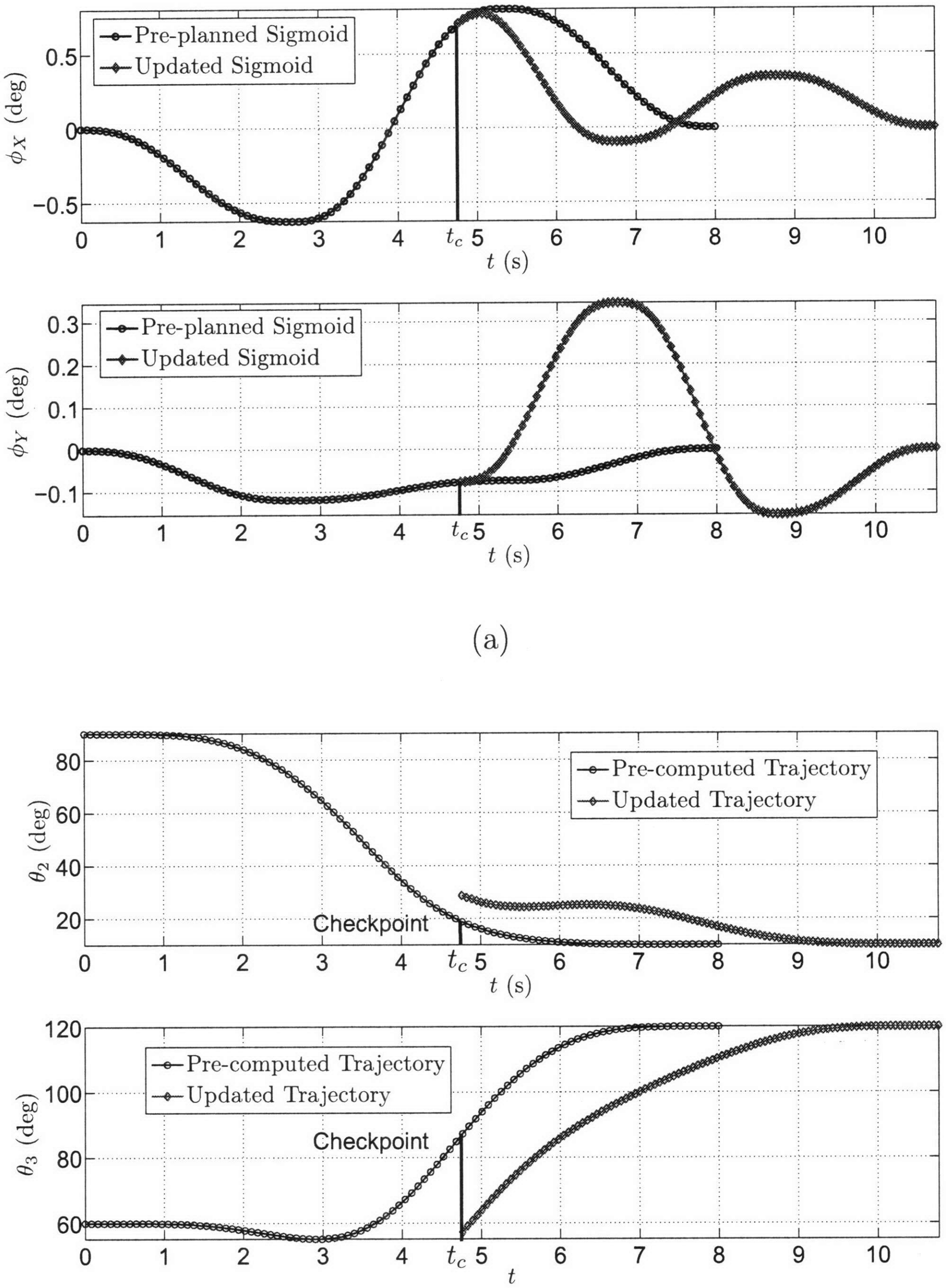

(a)

(b)

Figure 5-9: (a) Tilt trajectories; (b) Unactuated link trajectory

Chapter 6

Implementation and Experiments

6.1 Fixed Axis of Tilt

We conducted position control experiments on a prototype system with 3 links which is shown in Fig. 6-1. The link mechanism, which operates inside the wing-box, is shown in Fig. 6-1(a). The links are essentially C-channels which are serially connected by 1 d.o.f rotary joints. Link 1 is the *only* servoed link. Links 2 and 3 are equipped with *on-off* pneumatic brakes. The relative angular displacement of each link is measured using an optical encoder placed at the rotary joint. The resolution of each encoder is 1000 pulses per revolution.

The actuators and transmission mechanisms for link 1 are completely outside the wing-box and are shown in Fig. 6-1(b). They comprise a servoed *tilting mechanism* and a servoed *azimuthal positioning mechanism.* The *tilting mechanism* is used to tilt link 1 relative to a vertical axis. Depending on the state (*on* or *off*) of the pneumatic brakes, the unactuated links (2 and 3) may be deployed by exploiting gravity and dynamic coupling with link 1. The *azimuthal positioning mechanism* is used for angular positioning of the entire link mechanism inside the wing-box and serves to expand the workspace of the robot arm. This mechanism is used after the links have been deployed using the *tilting mechanism.* The pneumatic brakes are in the *on* state when the *azimuthal positioning mechanism* is in use. Both mechanisms have harmonic drive gearing (100:1) coupled to AC servomotors (0.64 Nm, 3000rpm).

In the experiments that follow, the *azimuthal positioning mechanism* is not used. We only use the tilting mechanism to deploy the links and verify the proposed control law.

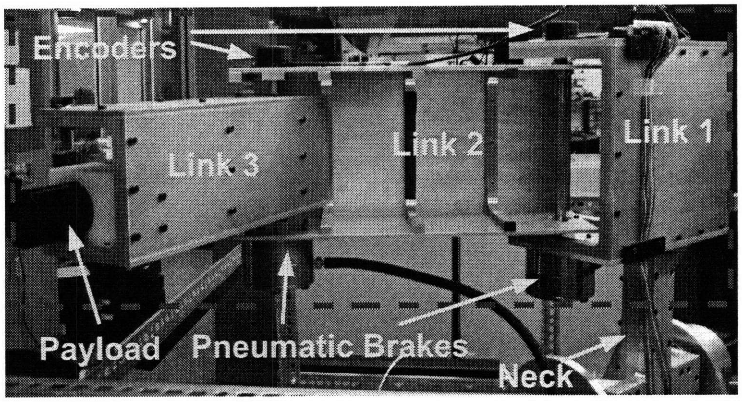

(a) Link mechanism (operates inside wing-box)

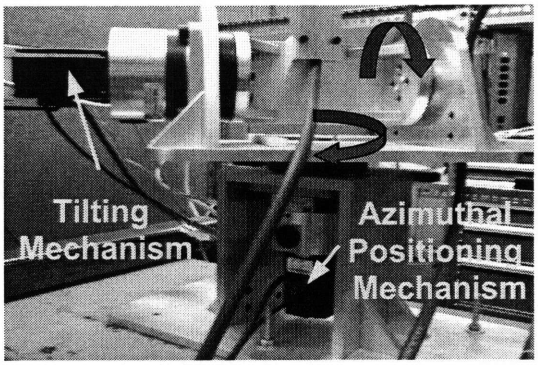

(b) Actuation Mechanisms (operate outside wing-box)

Figure 6-1: 3-link prototype arm

6.1.1 Feed-forward Control

Fig. 6-2 shows the experimental results for motion of the free link using a sigmoidal parameterization for the tilt trajectory. The initial position of link 2 was $\theta_{20} = 0°$ and the desired final position was $\theta_{2f} = 50°$. The 3^{rd} link was kept fixed at 0° during the motion. Fig. 6-2(a) shows the tilt trajectory. The 2 unknown parameters for the tilt trajectory $\phi(t)$ are $\phi_a = 1.10°$ and $\phi_b = -1.10°$. The other parameters were fixed at $\eta_1 = 0.33$ and $\eta_2 = 0.67$. The total duration of motion was $t_f = 4$ s. A viscous friction coefficient of $b_v = 0.2$ N-m/s was introduced into the model to determine the parameters for the tilt trajectory $\phi(t)$. The trajectory of the free link is shown in Fig. 6-2(b). The actual final position was $\theta_{2f} = 51°$.

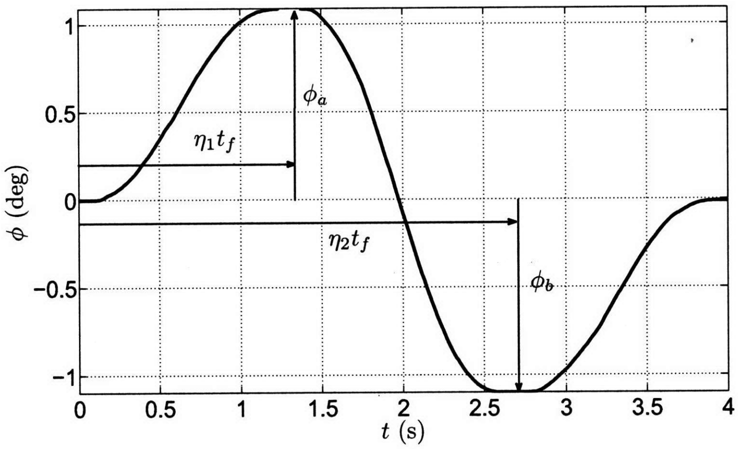

(a)

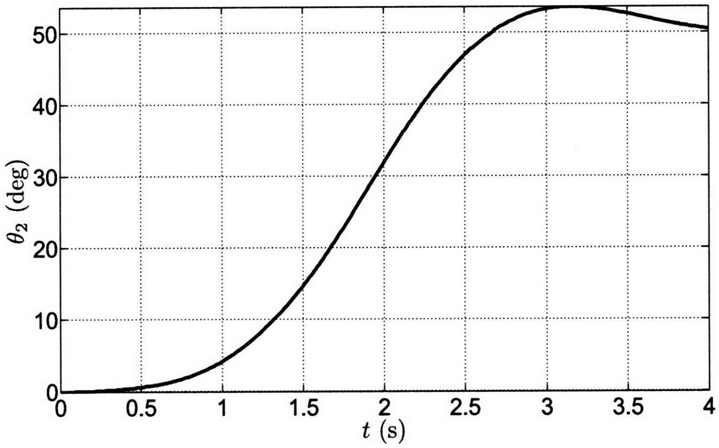

(b)

Figure 6-2: Feed-forward control algorithm on 3-link prototype: (a) Actuated joint trajectory; (b) Unactuated joint trajectory

6.1.2 Feedback Control

The dynamical system (3.9) corresponding to our experimental setup has the parameters $A = 32.8s^{-2}$ and $\alpha = -3.22°$. The experimental results are shown in Fig. 6-3. The goal was to move link 2 from an initial position $\theta_{20} = 35°$ to a desired final position of $\theta_{2f} = 50°$. Link 3 was kept fixed at 30° relative to link 2. The experiments were conducted for 3 sets of gains:

(a) $k = 12$, $k_1 = 1.2$ and $\bar{k}_2 = 0.2$ s,

(b) $k = 12$, $k_1 = 1$ and $\bar{k}_2 = 0.4$ s and

(c) $k = 12$, $k_1 = 0.8$ and $\bar{k}_2 = 0.4$ s.

It may be verified that these controller parameters ensure that the initial position lies within the estimated domain of convergence for the desired final position $\theta_{2f} = 50°$.

The tilt trajectory (ϕ) of link 1 is shown in Fig. 6-3(a) for various choices of the control gains. A small amplitude of ϕ is very important in practice because the arm operates inside an aircraft wing. The maximum tilt is 1.3° for the case $k = 12$ and $k_1 = 1.2$. This is small enough for operation inside the wing-box.

The trajectory (θ_2) of the free link is shown in Fig. 6-3(b). From (5.4), the quantity $k_2/\sqrt{k_1}$ $(= \bar{k}_2/\sqrt{kk_1})$ may be interpreted as a measure of "damping ratio" for the closed loop dynamics. As expected, less overshoot is observed as the "damping ratio" is increased. A lower "damping ratio" also results in a faster rise time. However, the corresponding settling time is also larger because of oscillations. As seen in Fig. 6-3b, the convergence time was $6.5s$, $4s$ and $2.5s$ for the various control gains.

Fig. 6-4 shows a comparison of the gravitational, inertial and centrifugal contributions to the angular acceleration of link 2 for each set of control gains. We use the full system model to compute the various effects. The angles and angular velocities used in the computation are based on actual data. The gravitational contribution clearly dominates the other dynamical effects in each case. This demonstrates, *a posteriori*, the validity of the approximations made in our dynamic modeling.

The control law (5.1) demonstrates reasonable positioning accuracy of the unactuated links. The performance is achieved without any knowledge of stiction or the dynamics introduced by the flexible hose supplying air to the pneumatic brakes.

We also conducted experiments with the modified time varying control law (5.16) on our prototype system. The goal was to move link 2 from an initial position

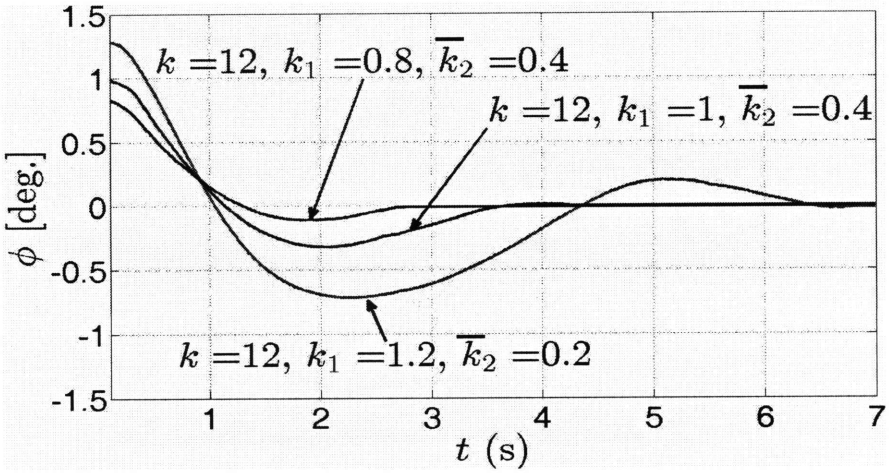

(a) Link 1 trajectory (servoed joint)

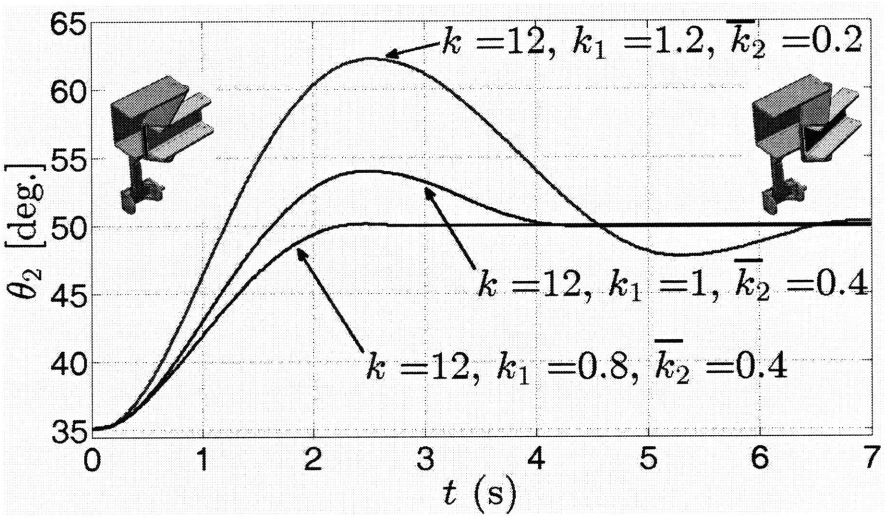

(b) Link 2 trajectory (unactuated joint)

Figure 6-3: Feedback control algorithm on 3-link prototype: (a) Actuated joint trajectory; (b) Unactuated joint trajectory

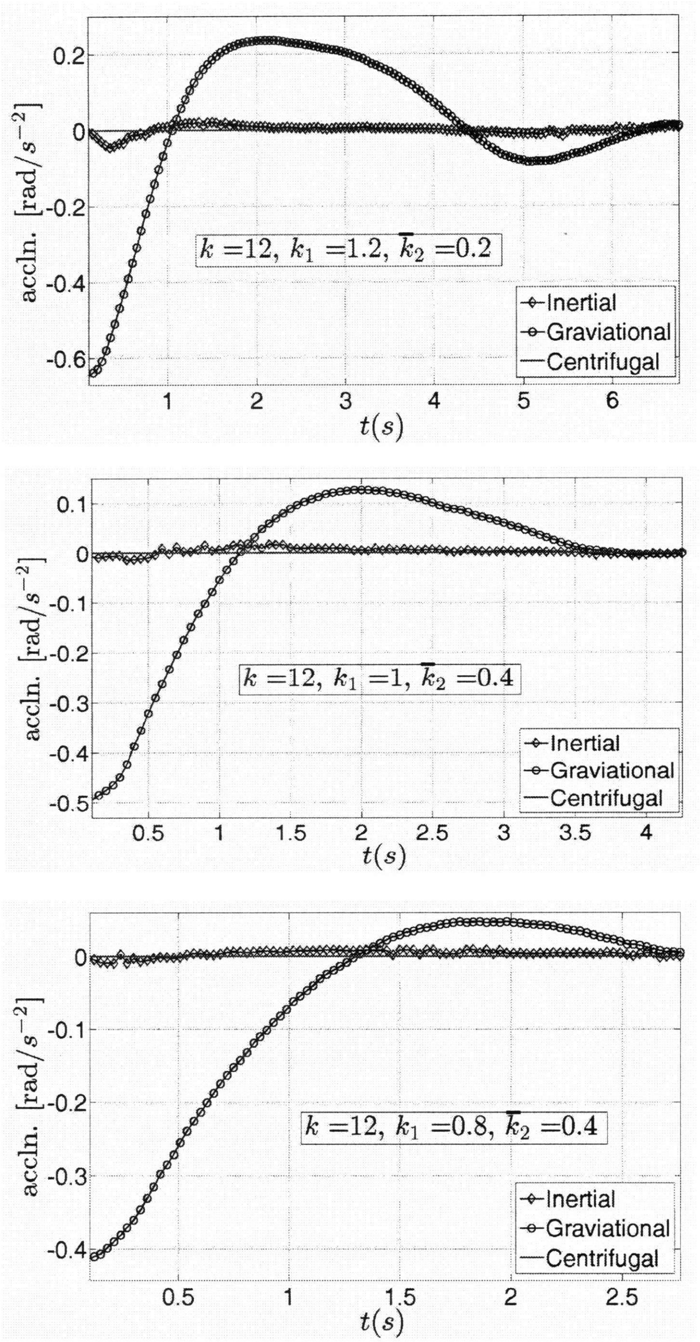

Figure 6-4: Comparison of gravitational, inertial and centrifugal contributions to acceleration of free link

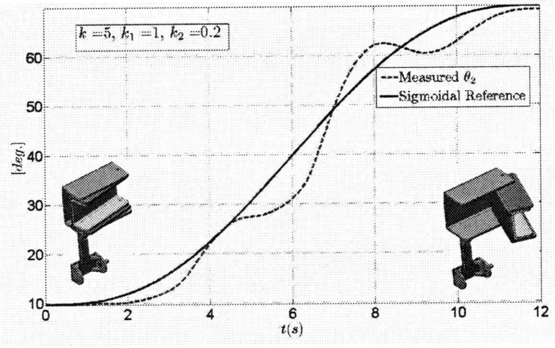

(a) Link 2 trajectory (unactuated joint)

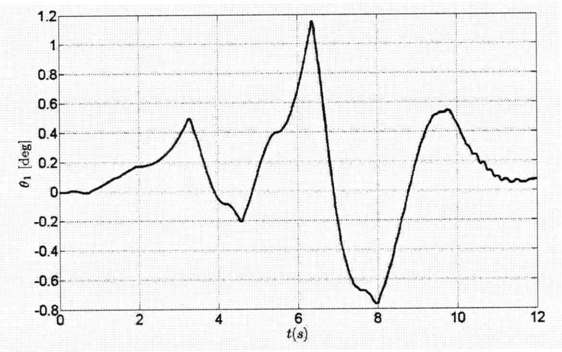

(b) Link 1 trajectory (servoed joint)

Figure 6-5: Experimental results for modified control law using sigmoidal reference trajectory

$\theta_{20} = 10°$ to a desired final position of $\theta_{2f} = 70°$. Link 3 was kept fixed at 0° relative to link 2. The controller parameter values in (5.16) were set at $k = 5$, $k_1 = 1$ and $k_2 = 0.2s$, $t_{f1} = 12s$. The experimental results are shown in Fig. 6-5. The actual final position was 69.7° at the end of $12s$, as shown in Fig. 6-5a. The tilt trajectory of link 1 is shown in Fig. 6-5b. The maximum amplitude of tilt of link 1 was 1.1° which is within the acceptable limits.

6.2 Arbitrary Axis of Tilt

We conducted position control experiments on a prototype system with 4 links. The links are deployed using a hexapod mechanism, which is shown in Fig. 6-6. By coordinating the motion of the six legs of the hexapod, it is possible to choose the orientation of the axis of tilt and the angle of tilt of the hexapod table arbitrarily. The legs of the hexapod are actuated by means of AC servomotors coupled to linear ball screw mechanisms. The hexapod table is equipped with a dual-axis MEMS tilt sensor for determining its absolute orientation with respect to the direction of gravity. The hexapod table interfaces with the hyper-articulated link mechanism through a coupling comprising two parts:

1. Azimuthal positioning mechanism.
2. Neck

These are shown in Fig. 6-7(a). The *azimuthal positioning mechanism* is used for angular positioning of the entire link mechanism inside the wing-box and serves to expand the workspace of the robot arm. It may be noted that the limited azimuthal rotation range of the hexapod table necessitates the additional *azimuthal positioning mechanism.* We use harmonic drive gearing (100:1) coupled to an AC servomotor (0.64 N-m, 3000 rpm) for the azimuthal positioning mechanism. The *neck* is essentially a hollow cylindrical tube connecting the link mechanism with the *azimuthal positioning mechanism.*

The link mechanism, which operates inside the wing-box, is shown in Fig. 6-7(b). The links are essentially C-channels which are serially connected by 1 degree-of-freedom rotary joints. Link 1 is the *only* actuated link. Links 2, 3 and 4 are equipped with *on-off* electromagnetic brakes. The brakes for links 2, 3 and 4 are rated at 50 N-m, 20 N-m and 12 N-m respectively. The relative angular position of the links are measured using optical encoders placed at the rotary joints. They have a resolution of 1000 pulses per revolution.

The hexapod is used to tilt link 1 about an arbitrary axis in the horizontal plane. Depending on the state (*on* or *off*) of the electromagnetic brakes, the unactuated links (2, 3 and 4) may be deployed by exploiting gravity and dynamic coupling with link 1. The *azimuthal positioning mechanism* is used after the links have been deployed using the hexapod. The electromagnetic brakes are in the *on* state when this mechanism is in use. In the experiments that follow, the *azimuthal positioning mechanism* is not used. We only use the tilting mechanism to deploy the links and verify the proposed control laws.

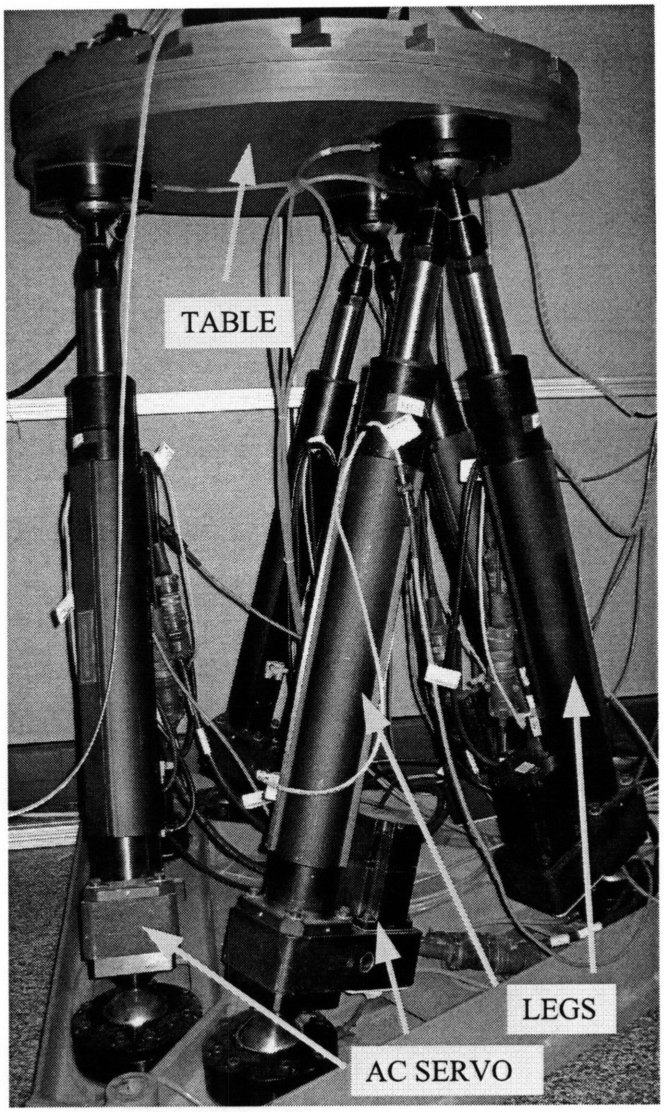

Figure 6-6: Hexapod mechanism

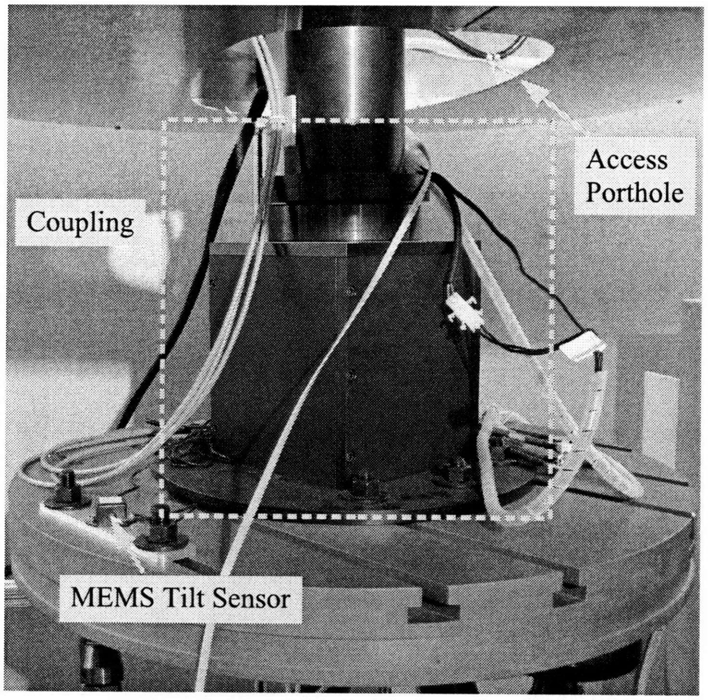

(a)

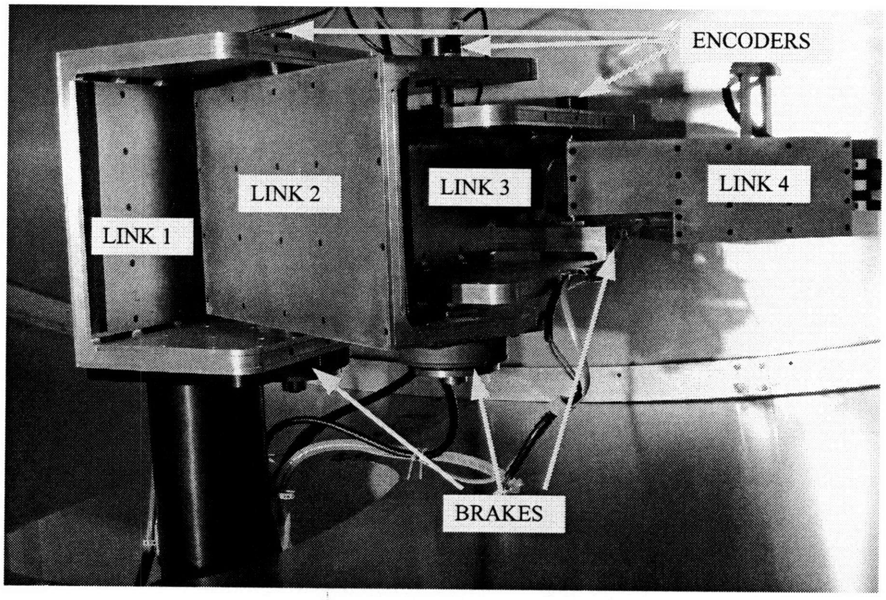

(b)

Figure 6-7: Prototype 4 link system: (a) Azimuthal rotation mechanism; (b) Link mechanism

6.2.1 Sequential Deployment

We conducted position control experiments on our prototype system. We used the algorithm presented in Section 4.1.4, where the axis of tilt is chosen symmetrically with respect to the initial and final positions of the center-of-mass. Fig. 6-8 shows the results for an initial position of $\theta_{20} = 0°$ and desired final position $\theta_{2f} = 90°$. The actual final position was $\theta_{2f} = 87.75°$. This discrepancy is due to unmodelled dynamical effects such as cabling and friction. This may be corrected by using the feedback control scheme presented in Chapter 5

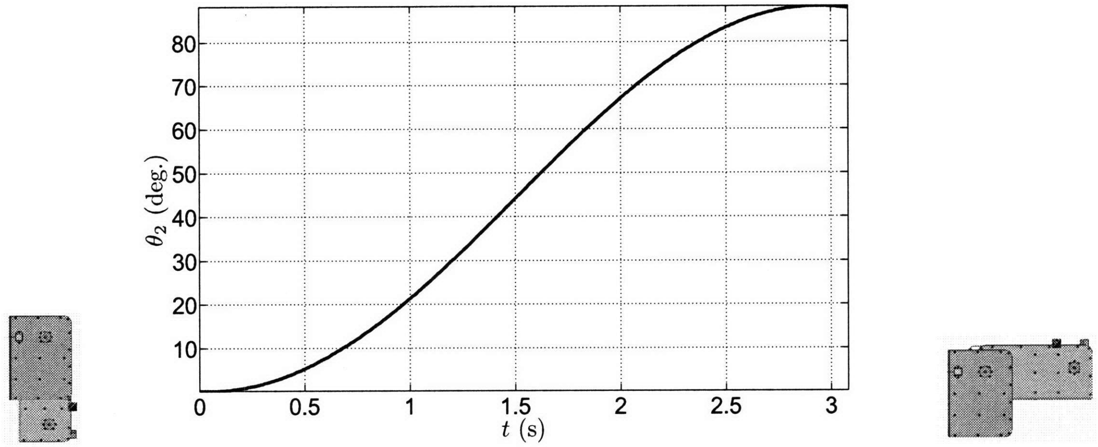

Figure 6-8: Link 2 trajectory

6.2.2 Concurrent Multi-link Deployment

We conducted position control experiments on the prototype system to verify the control algorithms for concurrent multi-link deployment. We verify the theoretical predictions for both *in-phase* and *out-of-phase* motion. Fig. 6-9(a) shows the experimental results for *in-phase* motion. The boundary conditions and duration of motion are identical to those of the simulation results presented in Fig. 4-8. Fig. 6-9(b) shows the experimental results for *out-of-phase* motion. The boundary conditions and duration of motion correspond to the simulation results presented in Fig. 4-9. The actual final positions were $[\theta_2(t_f), \theta_3(t_f)] = [56.25°, 29.97°]$ for *in-phase* motion and $[\theta_2(t_f), \theta_3(t_f)] = [77.58°, 90.45°]$ for *out-of-phase* motion. The experimental results show reasonable agreement with the theoretical predictions. The errors in the final positions may be attributed to unmodelled dynamical effects such as friction and presence of cables. These errors may be compensated by using the sequential closed-loop control scheme presented in Chapter 5.

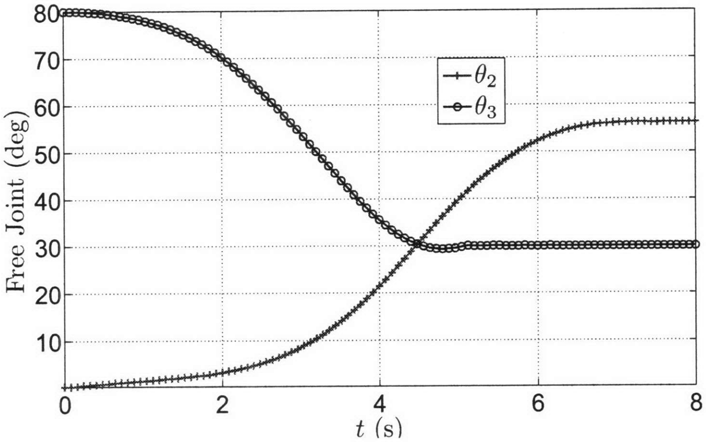

(a)

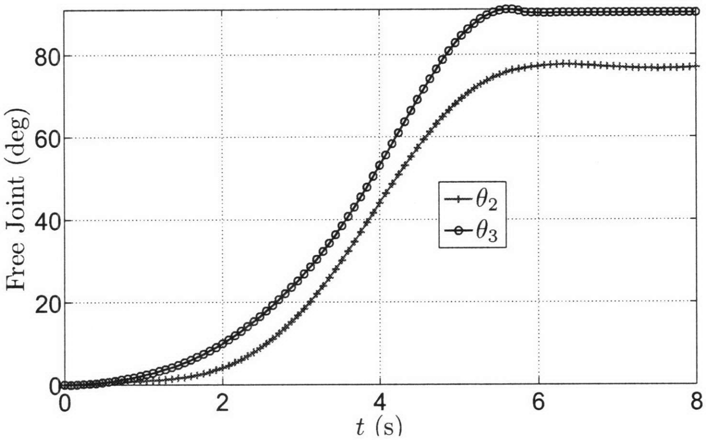

(b)

Figure 6-9: Experimental results: (a) In-phase motion; (b) Out-of-phase motion

Chapter 7

Conclusions

7.1 Summary of Contributions

This thesis presented a new design and actuation mechanism for a hyper-articulated robot arm. The arm is underactuated with just a few active joints driving a multitude of passive joints. This underactuated arm design was motivated by the need for a compact snake-like robot for assembly operations inside an aircraft wing.

- We proposed a "nested-channel" hyper-articulated mechanism, which is extremely compact and has a high expansibility. The joints of the hyper-articulated arm have no dedicated actuators. Instead, they are deployed by modulating gravitational torques. By tilting the base link appropriately, the gravitational torque drives each unactuated link to a desired angular position. With simple, compact locking mechanisms, the arm can change its configuration using the actuated base placed outside the wing. This underactuated design results in a compact arm with a high payload carrying capacity. These characteristics make the arm particularly well suited to high payload assembly operations inside an aircraft wing.

- We analyzed dynamical models for fixed as well as arbitrary axes of tilt in the horizontal plane. For sequential link deployment, we showed that the dynamics of the free links are primarily influenced by gravity; the centrifugal, Coriolis and inertial effects are negligible. For concurrent multi-link deployment, the centrifugal, Coriolis and inertial coupling between free links is significant. The behavior of the system is akin to a k-pendulum in a modulated gravity field. The simplified system models greatly facilitate the synthesis of control laws.

- The dynamics (actual, as well as approximate) of the free links are essentially 2^{nd} order non-holonomic constraints. We proposed several motion planning algorithms which satisfy these constraints. The motion planning problem is formulated as a non-linear two point boundary value problem through a suitable parameterization of the input. This formulation may be used to generate input trajectories for both sequential and concurrent multi-link deployment.

- We proposed a closed loop control algorithm for sequential deployment of the unactuated links. This algorithm is based on the simple idea of introducing a virtual non-linear spring and damper into the system dynamics. A Lyapunov function was synthesized to prove the convergence of the control law. The Lyapunov function is used to generate estimates of the domain of convergence of the control law for various control gains. These estimates are usually less conservative than those provided by the Hamiltonian.

- We proposed an open-feedback scheme for deploying multiple links in unison. This is done by updating the motion plan based on periodic measurements of the output. The updated motion plan is generated by solving the associated boundary value problem with updated initial conditions from the measured output. The updated input is patched smoothly with the pre-computed input. This results in improved positioning accuracy of multiple free links.

- We built two prototypes to demonstrate our design and control algorithms. The first prototype has one actuated link and three unactuated links. The axis of tilt is fixed in the horizontal plane. It has two unactuated links. The second prototype has one actuated link and three unactuated links. The axis of tilt may be chosen arbitrarily in the horizontal plane. This is accomplished using a hexapod.

- The motion planning and closed loop control algorithms were applied to both prototypes. The experimental results demonstrate the efficacy of the control laws in the absence of prior knowledge of friction and other unmodelled dynamical effects.

7.2 Future Directions

- **Unactuated joint redesign:** The unactuated joints of the robot arm may be made more compact by integrating the bearings and encoders with the electromagnetic brakes. Using this approach, it may not be necessary to shrink the link dimensions.
- **Existence of solution for the motion planning problem:** We formulated the motion planning problem as a boundary value problem and solved it numerically. The input was limited to the class of polynomial sigmoidal functions. The numerical solution to the boundary value problem converged for all the boundary conditions that we tried. However, the existence of solutions to this boundary value problem remains to be theoretically established.
- **Hybrid control formulation for concurrent multi-link motion:** We formulated the motion planning problem such that multiple free links are unlocked and locked simultaneously at the beginning and end of motion respectively. Alternatively, the brakes may be treated as binary inputs which may be switched at appropriate time instants during the motion. The discrete binary inputs combined with the continuous tilt input open up interesting possibilities for hybrid control design.
- **Closed loop control with time varying reference:** The modified closed-loop control law for sequential link deployment results in a non-autonomous dynamical system. Our current proof has to be suitably modified to prove asymptotic convergence of the output using the modified control scheme.

- **Closed loop control for concurrent multi-link deployment:** We have presented motion planning and open-feedback schemes for concurrent multi-link deployment. It is not immediately clear as to how feedback control laws may be synthesized for concurrent multi-link deployment.

Appendix A

Dynamics of 2-link Arm

The dynamics of the 2-link arm may be written as

$$\begin{bmatrix} H_{11} & H_{12} \\ H_{12} & H_{22} \end{bmatrix} \begin{bmatrix} \ddot{\phi} \\ \ddot{\theta}_i \end{bmatrix} + \begin{bmatrix} F_1 \\ F_2 \end{bmatrix} + \begin{bmatrix} G_1 \\ G_2 \end{bmatrix} = \begin{bmatrix} \tau_1 \\ 0 \end{bmatrix}$$

The components of the 2×2 symmetric positive definite inertia matrix H are given by

$$\begin{aligned} H_{11} &= I_{yy1} + M_1((x_{c1} + a_1)^2 + z_{c1}^2) + I_{xx2}\sin^2\theta_2 + I_{yy2}\cos^2\theta_2 - I_{xy2}\sin 2\theta_2 \\ &\quad + M_2((y_{c2}\sin\theta_2 - (x_{c2} + a_2)\cos\theta_2 - a_1)^2 + (z_{c2} + d_2)^2), \qquad \text{(A.1)} \\ H_{12} &= M_2(z_{c2} + d_2)(y_{c2}\cos\theta_2 + (x_{c2} + a_2)\sin\theta_2) \\ &\quad + I_{yz2}\cos\theta_2 + I_{xz2}\sin\theta_2, \qquad \text{(A.2)} \\ H_{22} &= I_{zz2} + M_2((x_{c2} + a_2)^2 + y_{c2}^2). \qquad \text{(A.3)} \end{aligned}$$

M_1 and M_2 denote the masses of links 1 and 2 respectively. I_{xy2} etc. denote the moments of inertia of link 2 about a centroidal coordinate frame. The parameters x_{c2}, y_{c2}, z_{c2} are the coordinates of the center-of-mass of link 2 in the link-attached frame. Also, a_2, d_2 etc. refer to the corresponding Denavit-Hartenberg parameters.

The Coriolis and centrifugal effects are given by

$$
\begin{aligned}
F_1 &= (M_2(z_{c2} + d_2)((x_{c2} + a_2)\cos\theta_2 - y_{c2}\sin\theta_2) - I_{yz2}\sin\theta_2 + I_{xz2}\cos\theta_2)\dot{\theta}_2^2 \\
&\quad + (2M_2(a_1 + (x_{c2} + a_2)\cos\theta_2 - y_{c2}\sin\theta_2)((x_{c2} + a_2)\sin\theta_2 + y_{c2}\cos\theta_2) \\
&\quad - 2I_{xy2}\cos 2\theta_2 + (I_{yy2} - I_{xx2})\sin 2\theta_2)\dot{\phi}\dot{\theta}_2
\end{aligned}
\tag{A.4}
$$

$$
\begin{aligned}
F_2 &= M_2(a_1 + (x_{c2} + a_2)\cos\theta_2 - y_{c2}\sin\theta_2)((x_{c2} + a_2)\sin\theta_2 + y_{c2}\cos\theta_2)\dot{\phi}^2 \\
&\quad + (I_{xy2}\cos 2\theta_2 + 0.5(I_{yy2} - I_{xx2})\sin 2\theta_2)\dot{\phi}^2.
\end{aligned}
\tag{A.5}
$$

The gravitational effects G_1 and G_2 are given by

$$
\begin{aligned}
G_1 &= -M_1 g(z_{c1}\sin\phi - (x_{c1} + a_1)\cos\phi) \\
&\quad - M_2 g(y_{c2}\sin\theta_2 - (x_{c2} + a_2)\cos\theta_2 - a_1)\cos\phi + (z_{c2} + d_2)\sin\phi)
\end{aligned}
\tag{A.6}
$$

$$
G_2 = -M_2 g((x_{c2} + a_2)\sin\theta_2 + y_{c2}\cos\theta_2)\sin\phi.
\tag{A.7}
$$

Appendix B

Verifying LARC and HNC

Let us define:

$$b_0 \triangleq g = \begin{bmatrix} N_{11} \\ N_{12} \\ 0 \\ 0 \end{bmatrix} \tag{B.1}$$

$$\frac{\partial g}{\partial x} = \begin{bmatrix} 0 & 0 & 0 & \frac{\partial N_{11}}{\partial \theta_i} \\ 0 & 0 & 0 & \frac{\partial N_{12}}{\partial \theta_i} \\ 0 & 0 & 0 & 0 \\ 0 & 0 & 0 & 0 \end{bmatrix} \tag{B.2}$$

$$f = \begin{bmatrix} -N_{11}(F_1 + G_1) - N_{12}(F_2 + G_2) + N_{11}(x^*)G_1(x^*) \\ -N_{12}(F_1 + G_1) - N_{22}(F_2 + G_2) + N_{12}(x^*)G_1(x^*) \\ 0 \\ 0 \end{bmatrix} \tag{B.3}$$

$$\frac{\partial f}{\partial x} = \begin{bmatrix} -N_{11}\frac{\partial F_1}{\partial \dot{\phi}} - N_{12}\frac{\partial F_2}{\partial \dot{\phi}} & -N_{11}\frac{\partial F_1}{\partial \dot{\theta}_i} & -N_{11}\frac{\partial G_1}{\partial \phi} - N_{12}\frac{\partial G_2}{\partial \phi} & -N_{11}\frac{\partial G_1}{\partial \theta_i} - N_{12}\frac{\partial G_2}{\partial \theta_i} \\ -N_{12}\frac{\partial F_1}{\partial \dot{\phi}} - N_{22}\frac{\partial F_2}{\partial \dot{\phi}} & -N_{12}\frac{\partial F_1}{\partial \dot{\theta}_i} & -N_{12}\frac{\partial G_1}{\partial \phi} - N_{22}\frac{\partial G_2}{\partial \phi} & -N_{12}\frac{\partial G_1}{\partial \theta_i} - N_{22}\frac{\partial G_2}{\partial \theta_i} \\ 1 & 0 & 0 & 0 \\ 0 & 1 & 0 & 0 \end{bmatrix} \tag{B.4}$$

Let us define:

$$b_1 \triangleq [f, g] = \frac{\partial g}{\partial x} f - \frac{\partial f}{\partial x} g = \begin{bmatrix} \frac{\partial N_{11}}{\partial \theta_i}\dot{\theta}_i + N_{11}^2 \frac{\partial F_1}{\partial \dot{\phi}} + N_{11}N_{12}(\frac{\partial F_2}{\partial \dot{\phi}} + \frac{\partial F_1}{\partial \dot{\theta}_i}) \\ \frac{\partial N_{12}}{\partial \theta_i}\dot{\theta}_i + N_{11}N_{12}\frac{\partial F_1}{\partial \dot{\phi}} + N_{12}^2 \frac{\partial F_1}{\partial \dot{\theta}_i} + N_{11}N_{22}\frac{\partial F_2}{\partial \dot{\phi}} \\ -N_{11} \\ -N_{12} \end{bmatrix} \tag{B.5}$$

$$b_1(x^*) = \begin{bmatrix} 0 \\ 0 \\ -N_{11} \\ -N_{12} \end{bmatrix} \tag{B.6}$$

$$\begin{aligned} \frac{\partial b_1}{\partial x} &= \begin{bmatrix} N_{11}N_{12}(\frac{\partial^2 F_2}{\partial \dot{\phi}^2} + \frac{\partial^2 F_1}{\partial \dot{\phi}\partial \dot{\theta}_i}) & \frac{\partial N_{11}}{\partial \theta_i} + N_{11}^2 \frac{\partial^2 F_1}{\partial \dot{\phi}\partial \dot{\theta}_i} + N_{11}N_{12}\frac{\partial^2 F_1}{\partial \dot{\theta}_i^2} & * & * \\ N_{11}N_{22}\frac{\partial^2 F_1}{\partial \dot{\phi}^2} + N_{12}^2 \frac{\partial^2 F_1}{\partial \dot{\phi}\partial \dot{\theta}_i} & \frac{\partial N_{12}}{\partial \theta_i} + N_{11}N_{12}\frac{\partial^2 F_1}{\partial \dot{\phi}\partial \dot{\theta}_i} + N_{12}^2 \frac{\partial^2 F_1}{\partial \dot{\theta}_i^2} & * & * \\ 0 & 0 & 0 & * \\ 0 & 0 & 0 & * \end{bmatrix} \\ &= \begin{bmatrix} 0 & \frac{\partial N_{11}}{\partial \theta_i} + N_{11}^2 \frac{\partial H_{11}}{\partial \theta_i} + 2N_{11}N_{12}\frac{\partial H_{12}}{\partial \theta_i} & * & * \\ -N_{11}N_{22}\frac{\partial H_{11}}{\partial \theta_i} + N_{12}^2 \frac{\partial H_{11}}{\partial \theta_i} & \frac{\partial N_{12}}{\partial \theta_i} + N_{11}N_{12}\frac{\partial H_{11}}{\partial \theta_i} + 2N_{12}^2 \frac{\partial H_{12}}{\partial \theta_i} & * & * \\ 0 & 0 & 0 & * \\ 0 & 0 & 0 & * \end{bmatrix} \end{aligned} \tag{B.7}$$

Let us define:

$$b_2 \triangleq [g, b_1] = \frac{\partial b_1}{\partial x} g - \frac{\partial g}{\partial x} b_1 = \begin{bmatrix} \frac{\partial N_{11}}{\partial \theta_i} \dot{\theta}_i + N_{11}^2 \frac{\partial F_1}{\partial \dot{\phi}} + N_{11} N_{12} (\frac{\partial F_2}{\partial \dot{\phi}} + \frac{\partial F_1}{\partial \dot{\theta}_i}) \\ \frac{\partial N_{12}}{\partial \theta_i} \dot{\theta}_i + N_{11} N_{12} \frac{\partial F_1}{\partial \dot{\phi}} + N_{12}^2 \frac{\partial F_1}{\partial \dot{\theta}_i} + N_{11} N_{22} \frac{\partial F_2}{\partial \dot{\phi}} \\ -N_{11} \\ -N_{12} \end{bmatrix} \tag{B.8}$$

Here:

$$b_{21} = \frac{H_{12} H_{22}}{\Delta^3} \frac{\partial \Delta}{\partial \theta_i} \tag{B.9}$$

$$b_{22} = -\frac{1}{\Delta^3} \left(H_{11} H_{22} \frac{\partial \Delta}{\partial \theta_i} - 2 H_{12}^3 \frac{\partial H_{12}}{\partial \theta_i} \right) \tag{B.10}$$

$$\Delta = H_{11} H_{22} - H_{12}^2 \tag{B.11}$$

$$\frac{\partial b_2}{\partial x} = \begin{bmatrix} 0 & 0 & 0 & \frac{\partial b_{21}}{\partial \theta_i} \\ 0 & 0 & 0 & \frac{\partial b_{22}}{\partial \theta_i} \\ 0 & 0 & 0 & 0 \\ 0 & 0 & 0 & 0 \end{bmatrix} \tag{B.12}$$

Let us define:

$$b_3 \triangleq [f, b_2] = \frac{\partial b_2}{\partial x} f - \frac{\partial f}{\partial x} b_2 = \begin{bmatrix} \frac{\partial b_{21}}{\partial \theta_i} \dot{\theta}_i - \left(\frac{\partial f}{\partial x} \right)_{11} b_{21} - \left(\frac{\partial f}{\partial x} \right)_{12} b_{22} \\ \frac{\partial b_{22}}{\partial \theta_i} \dot{\theta}_i - \left(\frac{\partial f}{\partial x} \right)_{21} b_{21} - \left(\frac{\partial f}{\partial x} \right)_{22} b_{22} \\ -b_{21} \\ -b_{22} \end{bmatrix} \tag{B.13}$$

$$b_3(x^*) = \begin{bmatrix} 0 \\ 0 \\ -b_{21} \\ -b_{22} \end{bmatrix} \tag{B.14}$$

We note that $N_{11}b_{22} \neq N_{12}b_{21}$. This implies that $b_0(x^*)$, $b_1(x^*)$, $b_2(x^*)$ and $b_3(x^*)$ span $\mathbb{R}^4$. Thus the set L satisfies the $LARC$ at x^* and the system is locally accessible at x^*.

Further, we verify that the **Hermes necessary condition** is satisfied at x^*, i.e.,

$$[g, [f, g]] \in \operatorname{span}\{f, g, [f, [f, g]]\}.$$

Indeed,

$$[f, [f, g]] = [f, b_1] = \frac{\partial b_1}{\partial x} f - \frac{\partial f}{\partial x} b_1 = - \begin{bmatrix} N_{11}^2 \frac{\partial G_1}{\partial \phi} + N_{1i} \frac{\partial N_1 1}{\partial \theta_i} G_1 \\ N_{11} N_{1i} \frac{\partial G_1}{\partial \phi} + N_{1i} \frac{\partial N_{1i}}{\partial \theta_i} G_1 \\ 0 \\ 0 \end{bmatrix}$$

Thus $[g, [f, g]]$ is spanned by g and $[f, [f, g]]$.

Appendix C

Negative Semi-Definiteness of $\dot{V}$

We establish the negative semi-definiteness of $\dot{V}$ for all $k_1, k_2 > 0$. Let us define:

$$F_{k_1}(\theta,\psi) = (P_{k_1}(\psi) + R_{k_1}(\psi))\tan^2\theta + 2Q_{k_1}(\psi)\tan\theta + R_{k_1}(\psi) \tag{C.1}$$

$$P_{k_1}(\psi) = k_1^2\sin^2\psi - 2k_1\sin\psi\sin\frac{2\psi}{k_1} \tag{C.2}$$

$$Q_{k_1}(\psi) = k_1\sin\psi(\cos\frac{2\psi}{k_1} - \cos\psi) \tag{C.3}$$

$$R_{k_1}(\psi) = k_1\sin\psi\sin\frac{2\psi}{k_1} - 2\sin^2\psi \tag{C.4}$$

We may rewrite (5.8) as:

$$\begin{aligned}\dot{V} &= -\frac{B^2k_2\sin^2\theta}{k_1(k_1^2-4)}[P_{k_1}(\psi)\sin^2\theta + Q_{k_1}(\psi)\sin 2\theta + R_{k_1}(\psi)]\\ &= -\frac{B^2k_2\sin^2\theta\cos^2\theta}{k_1(k_1^2-4)}[(P_{k_1}(\psi)+R_{k_1}(\psi))\tan^2\theta + 2Q_{k_1}(\psi)\tan\theta + R_{k_1}(\psi)]\\ &= -\frac{B^2k_2\sin^2\theta\cos^2\theta}{k_1(k_1^2-4)}F_{k_1}(\theta,\psi) \end{aligned} \tag{C.5}$$

We consider three cases to prove the negative semi-definiteness of $\dot{V}$ in Ω.

(i) $k_1 > 2$: In this case, we prove that $F_{k_1}(\theta,\psi) \geq 0$. We note that for $k_1 > 2$, $P_{k_1}(\psi), R_{k_1}(\psi) \geq 0$. Let us define:

$$S_{k_1}(\psi) \triangleq (P_{k_1}(\psi) + R_{k_1}(\psi))R_{k_1}(\psi) - Q_{k_1}^2(\psi). \tag{C.6}$$

Thus, $F_{k_1}(\theta, \psi) \geq 0$ *iff* $S_{k_1}(\psi) \geq 0$. Substituting (C.2) - (C.4) in (C.6) we have:

$$S_{k_1}(\psi) = k_1^3 \sin\psi \sin\frac{2\psi}{k_1} + 2k_1^2 \cos\frac{2\psi}{k_1} \cos\psi - (k_1^2 - 4)\sin^2\psi - 2k_1^2. \qquad \text{(C.7)}$$

We note that $S_{k_1}(0) = 0$ and $S_{k_1}(\psi) = S_{k_1}(-\psi)$. Also:

$$\frac{\partial S_{k_1}}{\partial \psi} = (k_1^2 - 4)(k_1 \sin\frac{2\psi}{k_1} - 2\sin\psi)\cos\psi \geq 0 \qquad 0 \leq \psi \leq \pi/2. \qquad \text{(C.8)}$$

Thus, $S_{k_1}(\psi) \geq 0$ for $|\psi| \leq \pi/2$.

(ii) $0 < k_1 < 2$: In this case, we prove that $F_{k_1}(\theta, \psi) \leq 0$. The argument follows along the same lines noting that $R_{k_1}(\psi) \leq 0$ and $P_{k_1}(\psi) + R_{k_1}(\psi) \leq 0$. Thus, $F_{k_1}(\theta, \psi) \leq 0$.

(iii) $k_1 = 2$: In this case, we prove that

$$f_2(\psi) \triangleq \lim_{k_1 \to 2} \frac{F_{k_1}(\theta, \psi)}{k_1 - 2} = [(p_2 + r_2)\tan^2\theta + 2q_2 \tan\theta + r_2] \geq 0 \qquad \text{(C.9)}$$

Here:

$$p_2(\psi) = \lim_{k_1 \to 2} \frac{P_{k_1}(\psi)}{k_1 - 2} = 2\sin^2\psi + 2\psi \sin\psi \cos\psi \qquad \text{(C.10)}$$

$$q_2(\psi) = \lim_{k_1 \to 2} \frac{Q_{k_1}(\psi)}{k_1 - 2} = \psi \sin^2\psi \qquad \text{(C.11)}$$

$$r_2(\psi) = \lim_{k_1 \to 2} \frac{R_{k_1}(\psi)}{k_1 - 2} = \sin^2\psi - \psi \sin\psi \cos\psi \qquad \text{(C.12)}$$

As before, we note that $p_2(\psi), r_2(\psi) \geq 0$. Let us define:

$$s_2(\psi) \triangleq (p_2(\psi) + r_2(\psi))r_2(\psi) - q_2^2(\psi). \qquad \text{(C.13)}$$

Thus $f_2(\psi) \geq 0$ *iff* $s_2(\psi) \geq 0$. Substituting (C.10) - (C.12) in (C.13) we have:

$$s_2(\psi) = 3\sin^2\psi - 2\psi \sin\psi \cos\psi + \psi^2. \qquad \text{(C.14)}$$

We note that $s_2(0) = 0$ and $s_2(\psi) = s_2(-\psi)$. Also:

$$\frac{\partial s_2}{\partial \psi} = 4 \sin \psi (\psi \sin \psi + \cos \psi) \geq 0 \qquad 0 \leq \psi \leq \pi/2. \tag{C.15}$$

Thus, $s_2(\psi) \geq 0$ for $|\psi| \leq \pi/2$.

Appendix D

Stability of Cascade System

We justify the treatment of the actuated coordinate ϕ as a *pseudo input.* We denote the desired trajectory of ϕ by ϕ_d. From (5.1), $\phi_d = \sin^{-1}(\sin(k_1(\theta_f - \theta) - k_2\dot{\theta})\sin^2\theta/k)$. The dynamics of the actuated coordinate ϕ may always be feedback linearized by choosing the control torque as:

$$\tau_1 = \frac{\ddot{\phi}_d - 2\lambda\dot{\tilde{\phi}} - \lambda^2\tilde{\phi}}{N_{11}} + F_1 + G_1 + \frac{N_{12}}{N_{11}}(F_2 + G_2), \tag{D.1}$$

where:

$$\begin{bmatrix} N_{11} & N_{12} \\ N_{12} & N_{22} \end{bmatrix} = \begin{bmatrix} H_{11} & H_{i1} \\ H_{i1} & H_{ii} \end{bmatrix}^{-1},$$

$$\tilde{\theta}_1 = \phi - \phi_d \text{ and } \lambda > 0.$$

Using (D.1) in (3.1), the error dynamics of the actuated coordinate is given by:

$$\ddot{\tilde{\phi}} + 2\lambda\dot{\tilde{\phi}} + \lambda^2\tilde{\phi} = 0. \tag{D.2}$$

Let us define $x = [\theta, \dot{\theta}]^T$ and $y = [\tilde{\phi}, \dot{\tilde{\phi}}]^T$. The dynamics of the unactuated coordinate (x) and the error dynamics of the actuated coordinate (y) may be written in cascade form as $\dot{x} = f(x, y)$ and $\dot{y} = g(y)$. Here, $f(x, y) = [\dot{\theta}, A\sin\theta\sin(\phi_d + \tilde{\phi})]^T$ and $g(y) = [\dot{\tilde{\phi}}, -2\lambda\dot{\tilde{\phi}} - \lambda^2\tilde{\phi}]^T$. We note that $f(x, y)$ is globally Lipschitz and the linear subsystem

$\dot{y} = g(y)$ is globally exponentially stable. Also, we have proved that the non-linear subsystem $\dot{x} = f(x, 0)$ is asymptotically stable using La Salle's Theorem. It follows from Sontag's Theorem [18], [21] that the cascade system is locally asymptotically stable for an appropriate choice of λ.

Appendix E

Level Curves of Lyapunov Function

We construct $l(k_1, k_2) > 0$ such that the region $\Omega_l = \{[\theta, \dot{\theta}] : V(\theta, \dot{\theta}) < l\}$ is a subset of Ω. From (5.7),

$$V = \frac{\sqrt{C^2 + D^2}}{2(k_1^2 - 4)} \sin(2\theta + E) + \frac{1}{2k_1}(1 - \cos\psi) + \frac{1}{2}\dot{\theta}^2, \tag{E.1}$$

where $C = k_1(\cos\psi - \cos\frac{2\psi}{k_1})$, $D = k_1 \sin\frac{2\psi}{k_1} - 2\sin\psi$ and $E = \text{atan2}(C, D)$. From (5.5) and (E.1)

$$\begin{aligned} &\frac{1}{k_1}\int_0^{\psi} \sin x \sin^2(\frac{x + k_2\dot{\theta}}{k_1} - \theta_f)dx \\ &= \frac{\sqrt{C^2 + D^2}}{2(k_1^2 - 4)} \sin(2\theta + E) + \frac{1 - \cos\psi}{2k_1}. \end{aligned} \tag{E.2}$$

Using (5.6) in (E.2) and noting that $|\sin(2\theta + E)| \leq 1$ we have

$$\frac{1 - \cos\psi}{2k_1} - \frac{\sqrt{C^2 + D^2}}{2|k_1^2 - 4|} \geq 0. \tag{E.3}$$

From (E.1) and (E.3) we have

$$V \geq \overline{V} \triangleq \frac{1}{2k_1}(1 - \cos\psi)(1 - |\sin(2\theta + E)|) + \frac{1}{2}\dot{\theta}^2. \tag{E.4}$$

Let us consider the region (See Fig. E-1)

$$\overline{\Omega}_l = \{[\theta, \dot{\theta}] : \overline{V}(\theta, \dot{\theta}) < l, |2\theta + E| \leq \gamma_{max}\}, \tag{E.5}$$

where

$$l = \frac{1}{2k_1}(1 - \cos\psi_{max})(1 - |\sin\gamma_{max}|). \tag{E.6}$$

Here $\psi_{max} \in (0, \pi/2)$ and $\gamma_{max} \in (0, \pi/2) \cup (\pi, 3\pi/2)$ are to be determined such that $\overline{\Omega}_l$ is a subset of Ω. From (E.4), (E.5) and (E.6):

$$\psi, \dot{\theta} \in \overline{\Omega}_l \Rightarrow |\psi| \leq \psi_{max} \text{ and } |\dot{\theta}| < \dot{\theta}_{max} \triangleq \sqrt{2l}. \tag{E.7}$$

Using $\theta = \theta_f - (\psi + k_2\dot{\theta})/k_1$ and (E.7) we have

$$|\theta| \leq \theta_{max} \triangleq |\theta_f| + (\psi_{max} + k_2\dot{\theta}_{max})/k_1. \tag{E.8}$$

$\psi_{max} \in (0, \pi/2)$ and $\gamma_{max} \in (0, \pi/2) \cup (\pi, 3\pi/2)$ are chosen to satisfy

$$\theta_{max} \leq \min(\frac{1}{2}(\gamma_{max} - \max_{|\psi| \leq \psi_{max}} |E|), \pi). \tag{E.9}$$

Condition (E.9) implies that $|\theta| < \pi \ \forall \ \theta \in \overline{\Omega}_l$. From (E.7) and (E.9)

$$\psi, \theta \in \Omega_l \Rightarrow |\theta| < \pi \text{ and } |\psi| \leq \psi_{max} < \pi/2. \tag{E.10}$$

Thus $\overline{\Omega}_l \subset \Omega$. From (E.4), $V \geq \overline{V}$. Thus $\Omega_l \subset \overline{\Omega}_l \subset \Omega$.

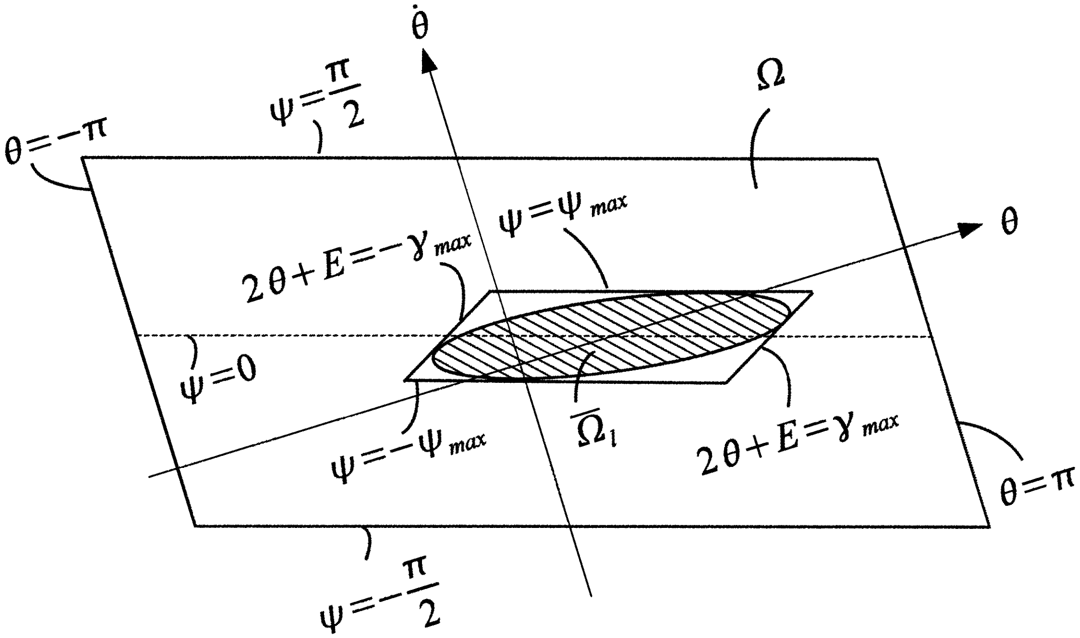

Figure E-1: Choice of l

Bibliography

[1] H. Arai, K. Tanie, and N. Shiroma. Nonholonomic control of a three-dof planar underactuated manipulator. *Robotics and Automation, IEEE Transactions on*, 14(5):681–695, Oct 1998.

[2] J. Hauser and R. M. Murray. Nonlinear controller for nonintegrable systems: the acrobot example. In *Proc. American Contr. Conf.*, pages 669–671, 3-5 Nov 1990.

[3] S. Hirose and M. Mori. Biologically inspired snake-like robots. In *Robotics and Biomimetics, 2004. ROBIO 2004. IEEE International Conference on*, pages 1–7, 22-26 Aug 1990.

[4] J. M. Hollerbach. Dynamic scaling of manipulator trajectories. *J. Dyn. Systems, Meas. and Control, ASME Trans*, 106:102–106, 1984.

[5] K. Kobayashi and T. Yoshikawa. Controllability of under-actuated planar manipulators with one unactuated joint. *The International Journal of Robotics Research*, 21, 2002.

[6] K. Kobayashi and T. Yoshikawa. Trajectory planning and control for planar robots with passive last joint. *The International Journal of Robotics Research*, 21, 2002.

[7] I. Kolmanovsky and N. H. McClamroch. Developments in nonholonomic control problems. *Control Systems Magazine, IEEE*, 15(6):20–36, Dec 1995.

[8] A. De Luca, R. Mattone, and G. Oriolo. Stabilization of an underactuated planar 2r manipulator. *International Journal of Robust and Nonlinear Control*, 10, 2000.

[9] A. De Luca and G. Oriolo. Motion planning under gravity for underactuated three-link robots. In *Intelligent Robots and Systems, 2000. (IROS 2000). Proceedings. 2000 IEEE/RSJ International Conference on*, pages 139–144, 31 Oct.-05 Nov 2000.

[10] K. M. Lynch, N. Shiroma, H. Arai, and K. Tanie. Collision-free trajectory planning for a 3-dof robot with a passive joint. *International Journal of Robotics Research*, 19(12):1171–1184, 2000.

[11] R. Mukherjee and D. Chen. Control of free-flying underactuated space manipulators to equilibrium manifolds. *Robotics and Automation, IEEE Transactions on*, 9(5):561–570, Oct 1993.

[12] Murray, Li, and Sastry. *A Mathematical Introduction to Robotic Manipulation.* CRC Press, Inc., 1st edition, 1994.

[13] Y. Nakamura and R. Mukherjee. Nonholonomic path planning of space robots via a bidirectional approach. *Robotics and Automation, IEEE Transactions on*, 7(4):500–514, Aug 1991.

[14] Y. Nakamura, T. Suzuki, and M. Koinuma. Nonlinear behavior and control of a nonholonomic free-joint manipulator. *Robotics and Automation, IEEE Transactions on*, 13(6):853–862, Dec 1997.

[15] G. Oriolo and Y. Nakamura. Free-joint manipulators: motion control under second-order nonholonomic constraints. In *Intelligent Robots and Systems '91. Intelligence for Mechanical Systems, Proceedings IROS '91. IEEE/RSJ International Workshop on*, pages 1248–1253, 3-5 Nov 1991.

[16] E. Papadopoulos and S. Dubowsky. On the nature of control algorithms for free-floating space manipulators. *Robotics and Automation, IEEE Transactions on*, 7(6):750–758, Dec 1991.

[17] E. Papadopoulos and S. Dubowsky. The kinematics, dynamics, and control of free-flying and free-floating space robotic systems. *Robotics and Automation, IEEE Transactions on*, 9(5):531–543, Oct 1993.

[18] E. D. Sontag. Remarks on stabilization and input-to-state stability. In *Decision and Control, 1989., Proceedings of the 28th IEEE Conference on*, pages 1376–1378, 13-15 Dec. 1989.

[19] M. W. Spong. Swing up control of the acrobot. *Control Systems Magazine, IEEE*, 15(5):49–55, Feb 1995.

[20] H. J. Sussmann. A general theorem on local controllability. *SIAM Journal on Control and Optimization*, 25(1):158–194, 1987.

[21] H. J. Sussmann and P.V. Kokotovic. The peaking phenomenon and the global stabilization of nonlinear systems. *Automatic Control, IEEE Transactions on*, 36(4):424–440, April 1991.

[22] T. Suzuki, M. Koinuma, and Y. Nakamura. Chaos and nonlinear control of a nonholonomic free-joint manipulator. In *Robotics and Automation, 1996. Proceedings., 1996 IEEE International Conference on*, pages 2668–2675, 22-28 Apr 1996.

[23] T. Suzuki, W. Miyoshi, and Y. Nakamura. Control of 2r underactuated manipulator with friction. In *Decision and Control, 1998. Proceedings of the 37th IEEE Conference on*, pages 2007–2012, 16-18 Dec 1998.

[24] T. Suzuki and Y. Nakamura. Control of manipulators with free-joints via the averaging method. In *Robotics and Automation, 1997. Proceedings., 1997 IEEE International Conference on*, pages 2998–3005, 20-25 Apr 1997.

[25] D. Tilbury, R.M. Murray, and S. S. Sastry. Trajectory generation for the n-trailer problem using goursat normal form. *Automatic Control, IEEE Transactions on*, 40(5):802–819, May 1995.

[26] D. Tilbury, O. J. Sordalen, L. Bushnell, and S. S. Sastry. A multisteering trailer system: conversion into chained form using dynamic feedback. *Robotics and Automation, IEEE Transactions on*, 11(6):807–818, Dec 1995.

[27] A. Wolf, H. B. Brown, R. Casciola, A. Costa, M. Schwerin, E. Shamas, and H. Choset. A mobile hyper redundant mechanism for search and rescue tasks. In *Intelligent Robots and Systems, 2003. (IROS 2003). Proceedings. 2003 IEEE/RSJ International Conference on*, pages 2889–2895, 27-31 Aug 2003.